Deterministic ratchets for suspension fractionation

Thanawit Kulrattanarak

Thesis committee

Thesis supervisor
Prof. dr. ir. R.M. Boom
Professor of Food Process Engineering, Wageningen University

Thesis co-supervisors
Dr. ir. R.G.M. van der Sman
Assistant Professor, Food Process Engineering Group, Wageningen University
Dr. ir. C.G.P.H. Schroën
Assistant Professor, Food Process Engineering Group, Wageningen University

Other members
Prof. dr. ir. C.J.N. Buisman
Wageningen University
Prof. dr. ir. J.G.E. Gardeniers
University of Twente
Prof. dr. ir. J. Westerweel
Delft University of Technology
Prof. dr. ir. A. Stankiewicz
Delft University of Technology

This research was conducted under the auspices of the Graduate School VLAG.

Deterministic ratchets for suspension fractionation

Thanawit Kulrattanarak

Thesis

Submitted in fulfilment of the requirements for the degree of doctor
at Wageningen University
by the authority of the Rector Magnificus,
Prof. dr. M.J. Kropff,
in the presence of the
Thesis Committee appointed by the Academic Board
to be defended in public
on Wednesday 28 January 2010
at 4 p.m. in the Aula

Thanawit Kulrattanarak
Deterministic ratchets for suspension fractionation
141 pages

Thesis, Wageningen University, Wageningen, NL (2010)
with references, with summaries in Dutch and English

ISBN: 978-90-8585-614-6

Contents

1 General introduction **1**

2 Classification and evaluation of microfluidic devices for continuous suspension fractionation **7**

3 Refinement of classification rules for deterministic ratchets through 2-D flow field simulation **47**

4 Image analysis of particle trajectories in deterministic ratchets including comparison with computed classification rules **71**

5 Analysis of particle motion in deterministic ratchet via experiment and simulation **99**

6 General discussion **119**

Summary **127**

Samenvatting **131**

Acknowledgement **135**

Curriculum vitae **137**

Overview of completed training activities **141**

Chapter 1

General introduction

1.1 Separation and fractionation of food suspension

Separation of particles from a liquid is a universal challenge in many different applications, be it e.g. separation of soil particles from dredging liquids, removal of yeast from a fermentation, or cream production from milk. Various technologies are used for this such as sedimentation tanks, centrifugation, and membrane separation. Each of these technologies has its own specific advantages, but it can be said that in general they are applied in such a way that the separation is as absolute as possible. This implies that absolute removal of the particles is targeted and not so much fractionation of the particles into different fractions. Although fractionation is not relevant for all applications, we find that especially in food, fractionation can open the way to sustainable use of raw materials, and new products. One of the technologies that in principle will allow fractionation is membrane filtration; therefore, we discuss this technology in more detail specifically for the food field, including some related new technologies that are the main interest of this work.

Membranes are widely used to remove particles from a food suspension [1], and we see numerous applications of microfiltration, ultrafiltration, nanofiltration in beer, milk, fruit juices and carbohydrate solution processing [2–6]. The pressure drop over the membrane pushes the fluid through the membrane, but also drags the suspended particles towards the membrane. Since mostly absolute retention of the particles is targeted, the membrane pores are smaller than the particles, and the particles accu-

mulate on the membrane surface, which lowers the throughput of the membranes, and therewith the overall productivity of the system [1]. In practice, the particle accumulation is generally reduced by applying high cross-flow velocities that partially remove the accumulated particles, or a low uniform transmembrane pressure that controls particle deposition, but these 'solutions' can never prevent particle accumulation.

Particle accumulation will have a negative effect on the overall productivity of a process, but besides it will also influence the selectivity of the process which is of great relevance if fractionation is the target [7–9]. Our research group has been investigating fractionation of milk [7–9], with the purpose of fractionating it into its constituent components (milk fat, bacteria, casein and whey proteins), and even into fractions of these components. Milk is a concentrated fluid, of which the components hardly differ in size; therefore, fractionation is a challenge [9]. One of the tools to facilitate membrane fractionation is to make use of shear-induced migration that influences particle movement in such a way that they accumulate less and in some cases even do not reach the membrane [10]. This method is currently investigated in our group, but still needs more research is needed to mature the technology further.

Besides membranes, alternative technologies are available, and one of the newest developments is the use of microfluidic devices. Currently, this technology is intensively investigated for biological applications, like sorting cells or DNA, and this is typically done with dilute suspensions for which the productivity per micro device may be low. However, the demands for food applications are much more stringent regarding the concentration of components and the through-put that is needed for industrial application. Although, microfluidic devices seem to have less problems with particle accumulation compared to membranes, their design needs careful consideration [13], as does up-scaling and evaluation for high-volume processing as is required for food processing. A recent study of Kitamuri [11, 12], is reassuring; it has shown that large scale production is indeed possible by mass parallization of microfluidic devices.

From literature, various microfluidic devices are known, and a short survey made us decide that deterministic ratchets [14], are the most promising microfluidic devices for food applications, therefore, they are the main focal point of this thesis.

1.2 Deterministic (DLD) ratchet

Deterministic ratchets, also known as deterministic lateral displacement (DLD) arrays, are microfluidic devices, invented by Austin and co-workers [14], that are used for sorting and fractionation of cells and DNA. From an extensive quantitative comparison of the DLD with other microfluidic devices (chapter 2), we have concluded that they have the highest potential for fractionating concentrated food suspensions on a large scale [13].

The fractionation process in deterministic ratchets is based on the flow line sieving principle [16], which is due to the interaction between the driving flow field and the steric interactions of suspended particles with solid obstacles placed in the flow field of a microchannel. The flow field is divided into flow lanes, which are separated from each other by dividing streamlines. These streamlines originate and terminate in flow stagnation points at the surface of the obstacles in the microchannel.

Particles having a radius smaller than the width of the flow lane will follow the streamlines and stay within the flow lane. Hence, it will show a zigzag motion around the obstacles in the microchannel. Particles having a radius larger than the flow lane width will have steric interaction with the obstacles in the microchannel, and consequently they will cross the dividing streamlines and they will be displaced to the adjacent flow lanes. This behavior is called displacement motion, which is shown in figure 1.1) together with the zigzag motion.

Since the particle behavior is determined by the ratio of flow lane width and particle size, this is an important design parameter for deterministic ratchets. Initially, the inventors have assumed equal flow lane width inside the pore space between obstacles [14] for the devices that they investigated, and later they have refined this to a parabolic flow profile in the pore space with all flow lanes having equal volumetric flow rate, leading to a non-uniform, but symmetric distribution of flow lane widths [17].

1.3 Research aim and thesis outline

The aim of this thesis is to evaluate deterministic (DLD) ratchets for a wide range of designs and render design rules for fractionation of concentrated food suspensions. Food applications have more stringent constraints than those investigated in literature until now. In the literature review described in chapter 2, the DLD is compared with

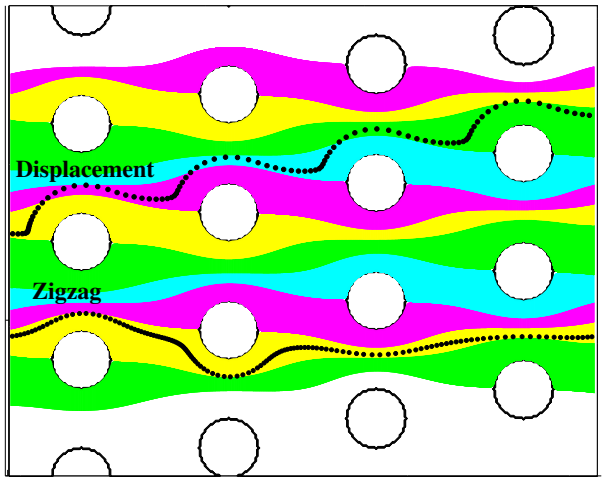

Figure 1.1: Flow lanes (indicated by color) and particle trajectories (dotted lines) showing zigzag and displacement motion through a periodic cell of a deterministic (DLD) ratchet. The figure shows a deterministic ratchet with cylindrical obstacles, with fluid flow induced by a pressure gradient in the horizontal direction. The dotted lines show particle trajectories for either displacement or zigzag motion. Zigzagging particles remain within their flow lanes, and particles moving by displacement mode move into neighboring flow lanes. Flow lanes are bounded by dividing streamlines, starting and ending at stagnation points at the back or the front of the obstacle.

other microfluidic devices based on key performance indicators like the yield, selectivity and the potential for large-scale application. From this quantitative evaluation, it is concluded that indeed the DLD is the most promising microfluidic device for food fractionation.

The deterministic ratchets are investigated via experiments and simulations, and the results are presented in chapters 3 to 5. The numerical analysis is performed using the Lattice Boltzmann method, via which we have computed a) the flow field and tracer particle trajectories with a 2D model (chapter 3), and b) trajectories of finite sized particles, whose motion is explicitly solved in a 3D model (chapter 5). In chapter 3, we use a 2-D lattice Boltzmann flow field simulation for a wide range of lattice designs, which is far beyond the charted territory in literature. From this, we have refined existing classification rules, based on the ratios of particle size to largest flow lane widths. Further, we have used these rules to formulate the design for compact ratchets having an optimal yield for concentrated food suspensions.

In chapter 4, particle behavior in deterministic ratchets is analyzed experimentally via high speed video-microscopy, combined with sophisticated image analysis that is

purposely developed for this application. The particle trajectories are characterized by their so-called migration angle, which is indicative for the type of motion that the particles exhibit (e.g. zigzag or displacement motion). The experimental results are compared with the simulation results from chapter 3, and based on that, design rules are derived allowing various motions, including a new mixed motion that was observed.

Chapter 5 describes the particle motion investigated via a combined analysis of experiment and 3D-simulation. Here, the simulation explicitly incorporates the motion of particles flowing through a periodic cell of ratchets. The results are compared with experimental observations and design rules from chapter 4, and the 2D simulations and the design rules derived from chapter 3. From this analysis, it has been possible to refine the design and classification rules even further.

In chapter 6, we summarize our insights in deterministic ratchets in terms of classification rules. Starting from the rules formulated in chapter 5, we re-evaluate the key performance indicators relevant for food applications, and give design rules for fractionation processes. Finally, we conclude with a recommendation for future research.

Acknowledgement

This research project was carried out within the framework of MicroNed (WP II-D). It was financially supported by the Royal Thai Government and MicroNed.

References

[1] G. Belfort, R.H. Davis, and A.L. Zydney. Review: The behavior of suspensions and macromolecular solutions in crossflow microfiltration. *J. Membr. Sci.*, **96** (1994) 1-58.

[2] Q. Gan, J.A. Howell, R.W. Field, R. England, M.R. Bird, C.L. O'Shaughnessy and M.T. MeKechinie. Beer clarification by microfiltrationproduct quality control and fractionation of particles and macromolecules. *J. Membr. Sci.*, **194**(2) (2001) 185-196.

[3] A.S. Grandison, W. Youravong and M.J. Lewis. Hydrodynamic factors affecting flux and fouling during ultrafiltration of skimmed milk. *Lait* **80** (2000) 165-174.

[4] M.A. Rao, T.E. Acree, H.J. Cooley, R.W. Ennis. Clarification of apple juice by hollow fiber ultrafiltration: fluxes and retention of odor-active volatiles. *J. Food Sci.*, **52**(2) (1987) 375-377.

[5] J. Warczok, M. Ferrando, F. Lopez and C. Güell. Concentration of apple and pear juices by nanofiltration at low pressures. *J. Food Eng.*, **63**(1) (2004) 63-70.

[6] A.K. Goulas, P.G. Kapasakalidis, H.R. Sinclair, R.A. Rastall, and A.S. Grandison. Purification of oligosaccharides by nanofiltration. *J. Membr. Sci.* **209**(1) (2002) 321-335.

[7] G. Brans, C.G.P.H. Schroën, R.G.M. van der Sman, and R.M. Boom. Membrane fractionation of milk: state of the art and challenges. *J. Membr. Sci.*, **243** (2004) 263-272.

[8] J. Kromkamp, F. Faber, C.G.P.H. Schroën, and R.M. Boom. Effects of particle size segregation on crossflow microfiltration performance: control mechanism for concentration polarisation and particle fractionation. *J. Membr. Sci.*, **268** (2006) 189-197.

[9] G. Brans, A. van Dinther, B. Odum, C.G.P.H. Schroën, and R.M. Boom. Transmission and fractionation of micro-sized particle suspensions. *J. Membr. Sci.*, **290** (2007) 230-240.

[10] J. Kromkamp, A. van der Padt, C.G.P.H. Schroën, and R.M. Boom. Shear induced fractionation of particles. *Patent*, **EP**20040078536.

[11] T. Kitamori. Integrated micro-nano chemical and bio systems. http://www.unisa.edu.au/promo/2003/micronano.pdf.

[12] M. Tokeshi, Y. Kikutani, A. Hibara, H. Hisamoto and T. Kitamori. Chemical processing on microchips for analysis synthesis and bioassay. *Electrophoresis.* **24** (2003) 3583-3594.

[13] T. Kulrattanarak, R.G.M. van der Sman, C.G.P.H. Schroën and R.M. Boom. Classification and evaluation of microfluidic devices for continuous suspension fractionation. *Adv. Colloid Interface Sci.*, **142** (2008) 53-66.

[14] L.R. Huang, E.C. Cox, R.H. Austin, and J.C. Sturm. Continuous Particle Separation Through Deterministic Lateral Displacement. *Science*, **304** (2004) 987-990.

[15] J.A. Davis, D.W. Inglis, K.J. Morton, D.A. Lawrence, L.R. Huang, S.Y. Chou, J.C. Strum, and R.H. Austin. Deterministic hydrodynamics: Taking blood apart. *PNAS*, **130**(40) (2006) 14779-14784.

[16] J.C.T. Eijkel, A. van den Berg. Nanotechnology for membranes, filters and sieves. *Lab Chip*, **6** (2006) 19-23.

[17] D.W. Inglis, J.A. Davis, R.H. Austin, and J.C. Sturm. Critical particle size for fractionation by deterministic lateral displacement. *Lap Chip*, **6** (2006) 655-658.

Chapter 2

Classification and evaluation of microfluidic devices for continuous suspension fractionation

Abstract

Membrane processes are well-known for separating and fractionating suspensions in many industries, but suffer from particle accumulation on the membrane surface. Currently, there are new developments using microfluidic devices for cell/DNA sorting and fractionation. We anticipate these devices are also applicable to fractionation of polydisperse and concentrated suspensions (e.g. foods), and may potentially have fewer problems with particle accumulation compared to membranes. This review article presents an overview of relevant microfluidic devices. We focus on their performance with respect to concentrated suspensions, as one finds in food industry. We give quantitative estimates on their yield, selectivity, and the potential for large-scale application. From this evaluation follows that deterministic ratchets seem most promising.

This chapter has been published as: T. Kulrattanarak, R.G.M. van der Sman, C.G.P.H. Schroën, R.M. Boom. Classification and evaluation of microfluidic devices for continuous suspension fractionation. *Adv Colloid Interface Sci.*, **142**:53-66 (2008).

2.1 Introduction

Many industries use membrane processes such as microfiltration, ultrafiltration, nanofiltration, etc [1–4] to purify, to concentrate, and to separate suspensions. A force field, like a pressure gradient, drives the suspending fluid and possible minor components through the membrane, while larger particles are retained. The main application of membranes is to separate the particulate phase from the suspending fluid. For many types of membranes, the particle separation is on the basis of their size and shape with respect to the membrane pore size. In rare applications, membranes are used to fractionate suspended particles of different sizes [5].

Here, we will make a clear distinction between separation and fractionation. Separation is the removal of particles from a suspending fluid, and fractionation is the removal of a class of particles from a complex suspension, based on size for example. In this review, we focus on fractionation.

Membrane separation at high permeation rates suffers from accumulation of non-permeating particles above the membrane surface, thereby blocking the pores and/or forming a cake layer [1]. This reduces the permeation rate and the separation performance of the membrane. The design of membrane processes requires quantitative expressions relating membrane and feed properties to separation performance [1, 6, 7]. Particle accumulation is the largest problem in membrane separation, and resolution of the problem through derivation of quantitative expressions is not straightforward [6]. In membrane fractionation applications the problem is even worse [8].

Recently, food industry sees much opportunity for (membrane) fractionation applications [4, 9]. Suspensions like milk or starch granule dispersions are complex, as they consist of particles of different shapes and sizes, and are quite concentrated, and thus prone to particle accumulation [4, 10]. Hence, there is a clear need to address the particle accumulation problem in fractionation applications. A solution to this problem might be found in the newly developed microfluidic devices used for fractionation and sorting of cells, DNA, and proteins in biological applications.

These devices are recently reviewed by Eijkel and Van den Berg [11, 12] with the biological applications in mind. However, compared to food the suspensions used in biological applications are very dilute. The fact that food suspensions are concentrated, sets quite different constraints on the design of the fractionation process using microfluidic devices, like low particle accumulation and high yields. This warrants

another review of these devices and their evaluation on performance indicators relevant to food applications. The above constraints probably make continuously operated micro-devices favorable for large scale application of fractionation in the food industry. Therefore, we restrict this review to continuous operation only.

In the review of Eijkel and Van den Berg [12], a list of sieving strategies for microfluidic devices is presented. This inspired us to make a classification of microfluidic devices to structure the wildly growing number and types of these fractionation devices. Our classification is based on the characteristic length scales of the devices.

After having stated our classification we discuss several devices, belonging to each class, and discuss their feasibility to fractionate food suspensions in qualitative terms. To perform a physically sound evaluation, we give also a quantitative estimation of the order of magnitude of performance indicators, such as yield, particle accumulation, and selectivity.

2.2 Classification

The review of Eijkel and Van den Berg [12] lists 4 strategies for sieving/filtering particles which are shortly discussed next. The first strategy is hydrodynamic chromatography, HDC, where larger particles are excluded from the wall region via the steric hindrance of the microchannel wall. The smaller particles can enter/leave the wall region via Brownian motion. As the average flow velocity in the wall region is lower than elsewhere in the microchannel, the smaller particles have a longer retention time in the microchannel. Hence, the smaller and larger particles are separated in time (see figure 2.1A) [13].

The second strategy is size exclusion chromatography, SEC, which is quite similar to HDC [14]. The microchannel now incorporates dead-end pores - with stagnant fluid - in which particles smaller than the pore diameter can dwell, making the residence time significantly larger than in HDC devices (see figure 2.1B).

A third sieving strategy is that of the classical membrane, where particles smaller than the pore diameter can pass the membrane - while larger ones are retained by the membrane.

The last sieving strategy is called flow line sieving. Via the inclusion of obstacles in the microchannel or via multiple outlets, the flow field in the microchannel gets structured into 'flow lanes' - which are separated by dividing streamlines. If Brownian

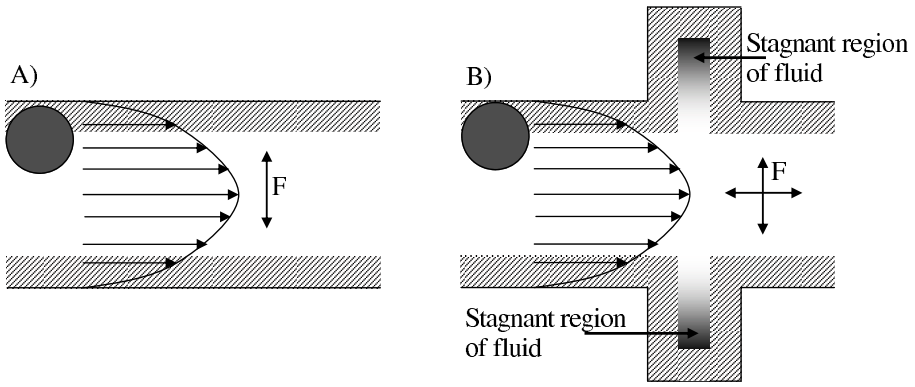

Figure 2.1: Sieving strategies. A) HDC B) SEC. Steric force, F, exerted on particles excluded from the shaded zones in the directions of forces.

motion is negligible and the suspension is dilute, smaller particles will follow streamlines, and will stay within the same flow lane. Larger particles can cross to another flow lane via steric interaction with obstacles in the microchannel, other particles or the microchannel walls. Fractionation is on the basis of the size of the flow lane.

We note, that both HDC and SEC sieving strategies are restricted to batch operation, as smaller and larger particles are only separated in time. This batch-wise operation makes them not very suitable for food applications. The membrane and flow line sieving devices do allow continuous operation, and are taken as distinct classes in our classification.

However, some new microfluidic devices using external force fields can not be classified as membrane or flow line sieving device. Hence, we extend the classification of Eijkel and van den Berg with new classes on the basis of geometrical factors relevant to the fractionation process, and the characteristics of the force field applied. All geometrical factors will be referred to the two particle diameters d_{p1} and d_{p2}, with $d_{p1} < d_{p2}$ (assuming a bidisperse suspension). The geometry of microfluidic devices is characterized with the following length scales:

- d_s is the smallest distance between solid obstacles inside the flow channel, or the pore diameter of a membrane.

- d_c is the width of the flow channel

- d_f the length scale of the flow structure, induced by the applied force field, inside the pore space of size d_s.

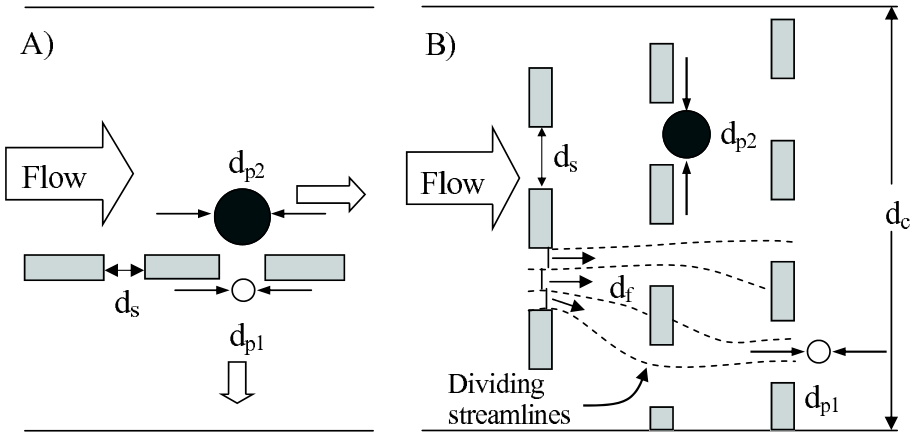

Figure 2.2: Geometric parameters that define A) the membrane device and B) the microfluidic device; for more information see text. Dashed lines indicate dividing streamlines.

Flow structuring (into flow lanes of size d_f) occurs in flow line sieving devices, but also in microchannels having an inhomogenous external force field, creating an array of traps. Both types of structuring are explained in more detail below. In figure 2.2 we have depicted the typical geometrical length scales in fractionating microfluidic devices. Comparing membranes and the majority of microfluidic devices gives readily a first classification of fractionation devices, which is:

1. Membrane Devices ($d_{p1}/d_s < 1 < d_{p2}/d_s$)
2. Microfluidic Devices ($d_{p1}/d_s < d_{p2}/d_s < 1$)

Microfluidic devices can be distinguished from membrane type devices by the fact that the largest particle is smaller than the smallest gap between structures: $d_{p2} < d_s$; for membranes $d_{p2} > d_s$. Membrane devices use the size exclusion principle for fractionation, meaning that only particles smaller than the pore size will pass the membrane, and hence $d_{p1} < d_s < d_{p2}$. Many microfluidic devices also rely on size exclusion, but use the length scale of the structuring of the flow field, d_f, created by external force fields or placement of solid obstacles in the microchannel. In devices having structured flows, fractionation occurs if $d_{p1} < 2d_f < d_{p2}$. If 2 $d_f < d_s$, we can have that $d_{p1} < d_{p2} < d_s$. It is this fact that makes these microfluidic devices less prone to particle accumulation than membranes.

The microfluidic devices are subdivided based on the type of force field that is applied and possible new length scales they introduce (d_f). We distinguish the following force fields: a) thermal fluctuations inducing Brownian motion, b) steric forces

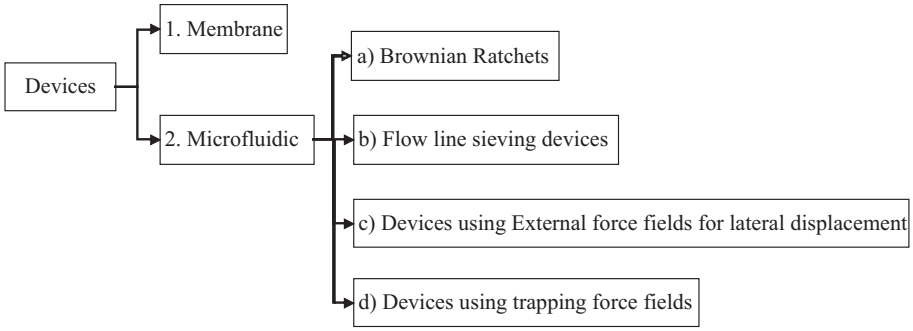

Figure 2.3: Classification tree of devices

as in flow line sieving devices, inducing the length scale $d_f < d_s$, c) external uniform force fields perpendicular to the flow field (inducing lateral displacement of particles), and d) external inhomogeneous (trapping) force fields, having a length scale $d_f < d_c$, leading to structuring of the flow field. The complete classification is shown in figure 2.3.

2.3 Membrane devices

Conventional microfiltration membranes are well-known for separation application. There are many types of materials, which are used to produce microfiltration membranes, such as polymers, ceramics, glass, metal, and silicon [5]. For fractionation conventional membranes are rarely used. Due to their wide distribution of pore sizes, they will have a low selectivity for fractionation on the basis of size exclusion. Furthermore, their yield is imparted by particle accumulation on the membrane [4]. The particle accumulation can be controlled to some extend by conventional means like high cross-flow velocities and back-pulsing, but this also requires more energy [4].

A more promising development for fractionation applications are the microsieves [5, 15]. They are made from silicon wafers with photolithographic etching techniques, and are smooth and thin with well controlled pore size, pore geometry, and porosity [5, 16, 17]. Microsieve membranes have high fluxes compared to classic microfiltration membranes because of their low flow resistance. From the experiments of Kuiper et al. [18], it is concluded that the flux of lager beer was a factor of 10-100 higher than found for conventional membranes.

Hence, a very good productivity for fractionation purposes can be obtained via the uniform and very narrow pore size distribution. However, if the pore diameter

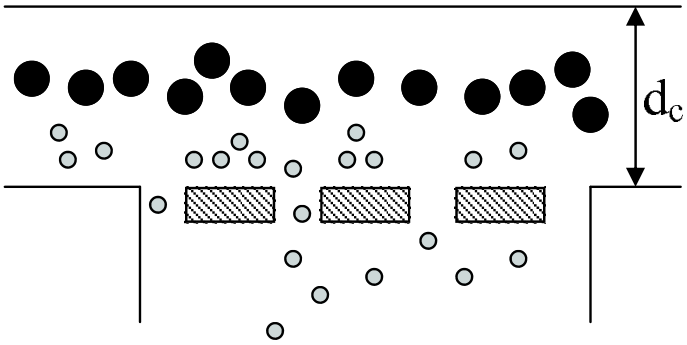

Figure 2.4: Shear-induced migration segregates particles in a microchannel, and possibly allows removal of small particles through a porous wall.

is smaller than the larger particle ($d_s < d_{p2}$), the pores will be plugged, preventing the smaller particles to pass through the membrane [7, 15]. Thus the yield may be greatly reduced. As for conventional membranes, high crossflow velocities and backpulsing can reduce particle accumulation on the membrane, and also external forces (ultrasonic, optical, or electronic force) can be applied to remove the accumulated particles which can improve the yield [19, 20].

A promising new remedy for particle accumulation is to make use of shear-induced migration using a shallow microchannel above the microsieve. It has recently been considered for particle sizes 0.5-30 μm [16]. In a suspension, hydrodynamic particle interactions in shear flow cause shear-induced diffusion, and as a result particles in a non-uniform shear field will migrate towards the centre of the flow channel [21]. Shear-induced diffusion is proportional to the shear rate, the particle radius squared, and the particle concentration in a highly non-linear way.

Hence, via careful tuning of the microchannel design larger particles will migrate towards the centre of the microchannel, while the small particles can permeate unhindered (see figure 2.4) [9, 21]. There is still much research needed to improve and optimize the technology, though we view it has high potential. We even see some potential for the use of shear induced migration in microfluidic fractionation devices - especially if non-dilute suspensions are used.

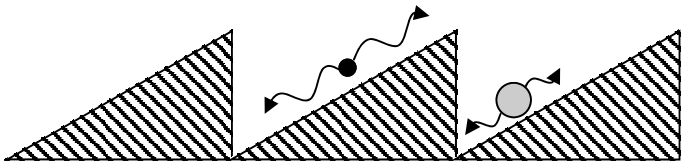

Figure 2.5: The Brownian motion of small and large particle in an asymmetric potential landscape.

2.4 Microfluidic devices

2.4.1 Brownian ratchets, BR

Brownian ratchets are periodic arrays of asymmetric obstacles placed in a microchannel. A force field, like a pressure gradient or an electric field, displaces the fluid and suspended particles through the arrays. Brownian motion is superimposed on the particle motion following the fluid streamlines. While moving through the ratchet, the particles collide with the asymmetric obstacles. A rectified motion of particles can occur via the interaction of force fields, Brownian motion and objects, where the asymmetry of the objects is essential [22, 23]. The asymmetric objects prevent the large particle from diffusing away from the streamlines via steric interactions, while the Brownian motion of the smaller particles is strong enough to allow them to diffuse to other flow lanes. The larger diffusivity of the smaller particle follows from the Stokes-Einstein equation:

$$D = \frac{kT}{3\pi\eta d_p} \tag{2.1}$$

Where D is the diffusion coefficient, k is Boltzmann's constant, T is the temperature, η is the viscosity, and d_p is the diameter of the particle.

The principle of ratchets is shown in figure 2.5. The steric interaction imposed by the asymmetric obstacles is represented by an asymmetric potential landscape. Each valley in the landscape represents a flow lane. The Brownian motion (thermal energy) of large particle is too small to move them over the maximum in the potential, while the thermal energy of smaller particles is large enough to hop over the maximum in the potential. As the potential is asymmetric, the probability of climbing over the less steep potential gradient is higher - leading to the rectified motion.

There are many different Brownian ratchets, however, there are two distinct sub-

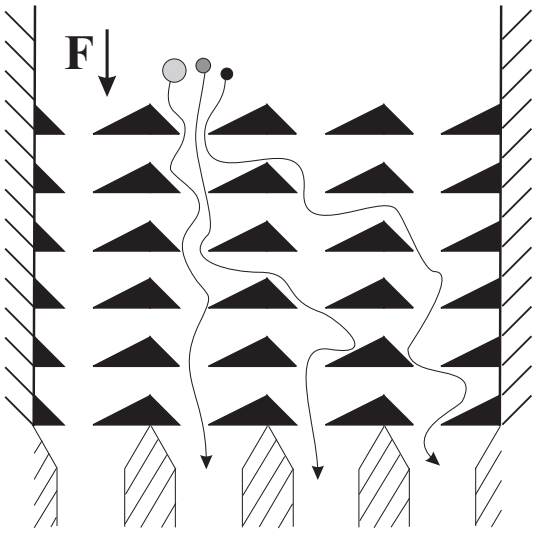

Figure 2.6: A force field displaces Brownian particle through asymmetric obstacles. The (small) particle diffuses in perpendicular direction to the force field.

classes that are considered appropriate for fractionation. The subclasses are based on drift principles by which the particles either migrate perpendicular (Geometric ratchets) [23–25], or parallel (Drift ratchets) [26–28] to the direction of the force field.

Geometric ratchets

The first class is the geometric Brownian ratchets, in which the rectified motion of the Brownian particle is in perpendicular direction to the driving force field. Generally, an electric field is used as the driving force, giving transport by electrophoresis. However, other force fields like a pressure gradient can be used as well as the driving force [23, 29]. In figure 2.6, the force field displaces a Brownian particle through asymmetric obstacles from top to bottom.

The magnitude of the ratchet effect and thus the selectivity depend very much on the obstacle shape, which can be optimized [23]. Geometric ratchets are used to fractionate particles in the range $0.1 \leq d_p \leq 1$ μm. The lower limit in particle size is probably set by the limitations in the lithography.

As Brownian motion is a stochastic process, the selectivity of this device for dilute suspensions is moderate. The yield will be limited, as the particle motion induced by the driving force field should be of similar order or even lower than the Brownian motion. Yield will improve by the use of smaller particles, as they have a higher diffusivity. Hence, this device is more favorable for small particles - in the order of 0.1

μm.

The effect of the use of concentrated suspensions on the selectivity is hard to predict. The higher concentration leads to shear induced diffusivity, which probably enhances the rectified motion. But this may be disrupted by particle-particle interaction. The use of concentrated suspensions also may lead to jamming (or bridging) of particles in the obstacle array, leading to a decrease in the yield.

Drift ratchets

The second class are the drift ratchets [26–28] that consist of many parallel asymmetrically shaped pores, where the rectified motion of particles is parallel to the force field. This device uses an oscillating flow field as a driving force [26, 28]. Figure 2.7 shows a schematic cross-section of the device. The device has two containers which are connected by a ratchet. A carrier liquid with suspended particles is pumped forward and backward through the ratchet by an oscillating force field. The net motion of the carrier liquid is zero but particles are separated by Brownian motion and steric interaction with the asymmetric pores [26–28]. Small particles end up in the left basin and large particles in the right basin [28]. In this device, particles are only separated in time, so this class of ratchets only allows batch operation, which is less favorable for larger scale application. However we have imagined a slight modification, which makes it possible for the drift ratchets to operate in a continuous way, as depicted in figure 2.8. This makes the potential of drift ratchets similar to that of geometric ratchets.

2.4.2 Flow line sieving devices

These devices use the interaction between the driving flow field and the steric interactions of particles, with confining walls or solid objects placed in the flow field, to fractionate particles [12]. The flow field can be divided into "flow lanes", having a length scale of d_f, which are separated by dividing streamlines which start/end at stagnation points present in the devices or their inlets and outlets (see figure 2.9). The particle size, d_p, with respect to d_f determines their motion. The smaller particles $d_{p1}<2d_f$ will follow their present flow lane, while larger particles can get displaced across the dividing streamlines via steric interactions, and thus enter neighboring flow lanes, leading to fractionation of the larger and smaller particles. Smaller particles will

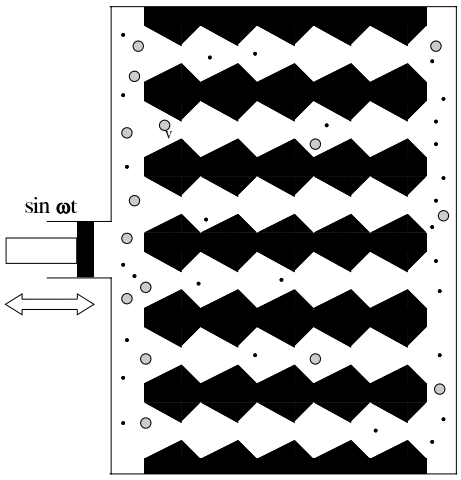

Figure 2.7: Schematic cross-section of a drift ratchet, the carrier liquid, including the suspended particles of different size, is pumped forward and backward through the asymmetrically shaped pores.

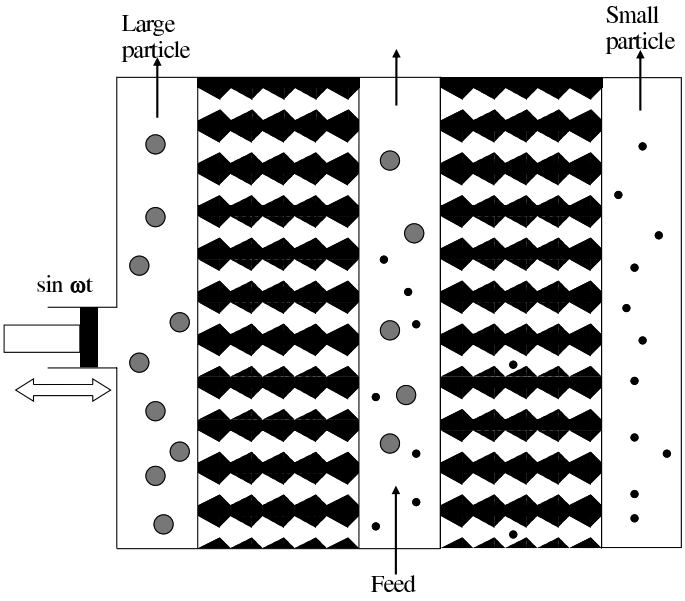

Figure 2.8: Sketch of a continuous set-up for drift ratchets of our own design.

only cross the dividing streamline via Brownian motion, or particle-particle interaction.

Deterministic ratchet, DR

Huang et al., [30] have invented the deterministic ratchet, where a particle suspension flows through a periodic array of obstacles (see figure 2.10). It follows the flow line sieving principle. Larger particles get displaced to adjacent flow lanes via steric

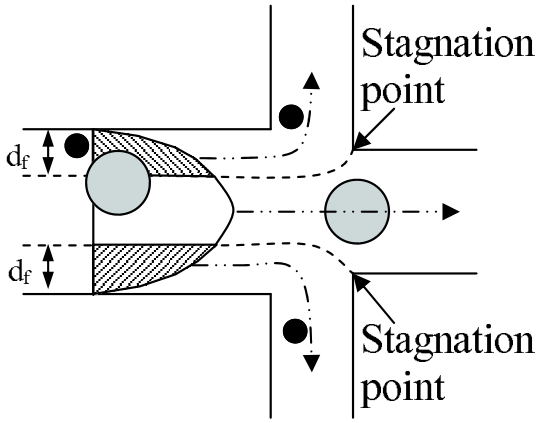

Figure 2.9: The principle of flow line sieving. The flow field is divided into flow lanes by stagnation points at the corners. Large particles with $d_{p2} > 2d_f$ are prohibited to enter the flow lanes along the channel wall, with size d_f and are excluded by steric interactions.

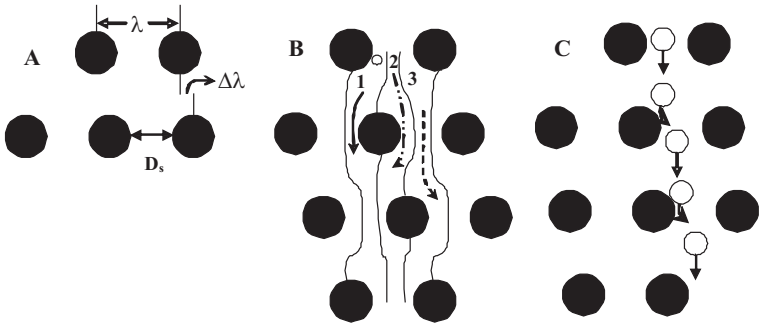

Figure 2.10: Description of characteristics of deterministic ratchets. The gap between obstacles contains 3 lanes. A: Geometric parameters related to obstacles. B: A particle with radius smaller than the width of lane 1 follows the streamline from lane 1, to 3, to 2 and back to 1; this is called zigzag mode. C: A particle with radius larger than the width of lane 1 moves in the initial lane; this is called displacement mode.

interactions between particles and a periodic array of obstacles in the flow channel. Brownian motion is negligible in the operating regime of this device. The special feature of the array of obstacles, is that each row of obstacles is shifted in lateral direction compared to the previous row, see figure 2.10A. This shift $\Delta\lambda$ is a fraction of λ, the distance from centre to centre of the obstacles ($\Delta\lambda < \lambda$). The obstacles will act as stagnation points, and divide the gap (with pore size d_s) in between obstacles into N=$\lambda/\Delta\lambda$ flow lanes. Hereby it is assumed by Huang and co-workers, that a uniform flow exists inside the pores, and consequently that the lane width $d_f = d_s/N$.

In figure 2.10B, we have drawn the obstacle array with $N = 3$. Small particles with

$d_{p1} < 2d_f$ will stay within the flow lane, and will display a zigzag motion through the obstacle array. Large particles $d_{p2} > 2$ d_f will display a continuous displacement to other flow lanes (see figure 2.10C). This displacement is similar to the rectified motion of particles in Brownian ratchets, but here the particle motion is purely deterministic, and hence the name deterministic ratchet.

Deterministic ratchets have been used to fractionate e.g. DNA-molecules and polystyrene beads. In recent experiments Inglis et al., [31] have used particles in the range of 2.3 to 22 μm and found that the assumption of uniform flow in the pore space is invalid, and now a parabolic flow profile is assumed. This leads to a non-uniform distribution of lane widths inside the pore space. This limits the range of particle sizes the deterministic ratchet can be applied to.

The selectivity of this device is relatively high. However, it can be limited by Brownian motion of small particles $d_p < 1\mu m$, albeit that increasing the flow velocity will reduce the effect of the Brownian motion. If concentrated suspensions are used there is a risk of jamming the pores, which will decrease the yield. However, we expect for objects with high aspect ratios (height over object diameter), $h \gg \{d_{p1}, d_{p2}\}$, the yield is still reasonable.

Hydrodynamic filtration, HF

This flow line sieving device uses a straight micro-channel with multiple side channels, as illustrated in figure 2.11. The size of flow lanes are controlled by the magnitudes of flow rates through the side channels relative to the flow rate in the main channel. Via steric interactions large particles ($d_{p2} > 2d_f$) are excluded from the flow lane along the main channel wall. Smaller particles can enter the side channels if $d_{p1} < 2d_f \leq d_s$ (see figure 2.11B) [32]. However, smaller particles can also remain in the main channel, which imparts the selectivity of this fractionation device. Selectivity is improved by taking a smaller ratio of d_{p2}/d_c, with d_c the width of the main channel.

Also multiple side channels can be used to enhance the selectivity. In these set ups the lane width of the first few side channels can be taken such that $2d_f < d_{p1}$, which can be used to concentrate the suspension. Obviously these effects can be combined to obtain multiple fractions from a polydisperse suspension in a single pass. Figure 2.11D shows a combination of these flow states to concentrate and fractionate suspension particles. The use of side channels makes the device inefficient regarding the available space on a wafer, and is thus not very appropriate for mass paralisation.

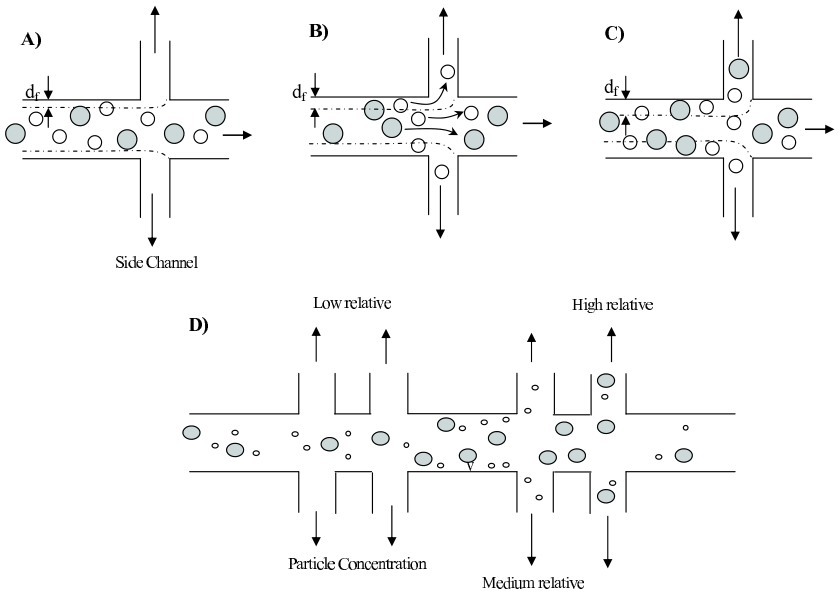

Figure 2.11: Hydrodynamic filtration. The relative flow rates is A) low in main channel, B) medium in main channel, and C) high in main channel. The dotted lines are the dividing streamlines of flow in main and side channels. D) Schematic diagram of a device with multiple branch points and side channels.

The yield of this device is low if $d_s \leq d_p < 2d_f$ due to particle plugging. The low selectivity and yield might be improved by the use of shear induced migration, which is effective if $d_c \approx 10\ d_{p2}$.

Asymmetric pinch flow fractionation, AsPFF

Takagi et al., [33] have developed asymmetric pinch flow fractionation (AsPFF), which is quite similar to hydrodynamic filtration. This device has 2 inlets to inject the suspension and the carrier fluids at different flow rates. The flow rate of the carrier fluid is higher than the flow rate of the suspension. By controlling the flow rates of these inlets, the suspension is forced to sidewall 1 in the pinched segment (see figure 2.12). In the pinched segment, the fluid fields are narrowed and divided in flow lanes spreading into multiple side branches. The distribution of the lane widths $d_{f,n}$ depends on the ratios between the flow rates through the multiple outlets. The steric interaction between the wall of the pinched segment and the particles, displaces larger particles to other flow lanes. Hence, in outlet 1 only particles enter with $d_{p1} < 2d_{f1}$. In outlet 2 particles enter with $d_{p1} < 2(d_{f1} + d_{f2})$. Note, also the smaller particles enter outlet 1. Similar to HF, AsPFF has a low selectivity.

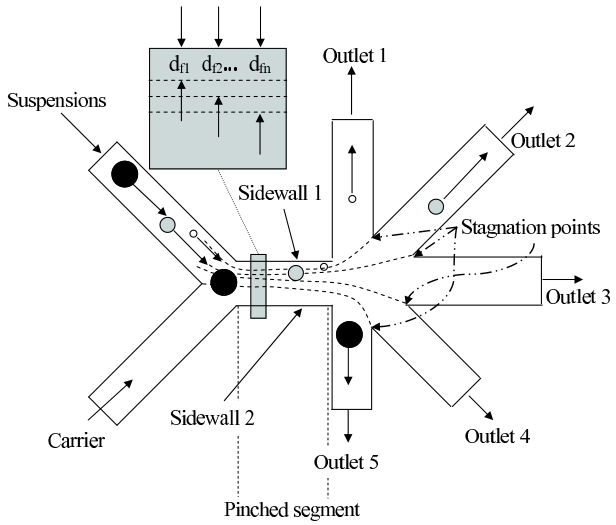

Figure 2.12: Schematic diagram that shows particle separation in asymmetric pinched flow fractionation, AsPFF.

As in HF the use of side channels makes the device inefficient regarding the available wafer space, and not quite appropriate for mass paralisation.

2.4.3 Devices using external force fields for lateral displacement

In this class of fractionation devices various external force fields are applied perpendicularly to the flow field (e.g. gravity, centrifugal, electric force). The motion of the particle depends on the physical properties of the particles with respect to the external force fields (e.g. permittivity, size). The lateral motion is superimposed on the motion induced by the drag force of the flow field.

Field flow fractionation, FFF

FFF is a fractionation technique, where particles are fractionated in a microchannel by applying an external driving force perpendicular to the flow of the fluid [34, 35]. The flow profile is parabolic and different external forces are used like thermal, electrical, centrifugal, gravitational, etc. [34–36]. FFF operations can be used in 3 modes; normal, steric, and hyperlayer mode. In normal mode, suspended particles are driven towards the accumulation wall. As a result a concentration polarisation layer is built up at the bottom of the microchannel. The build up of that layer is

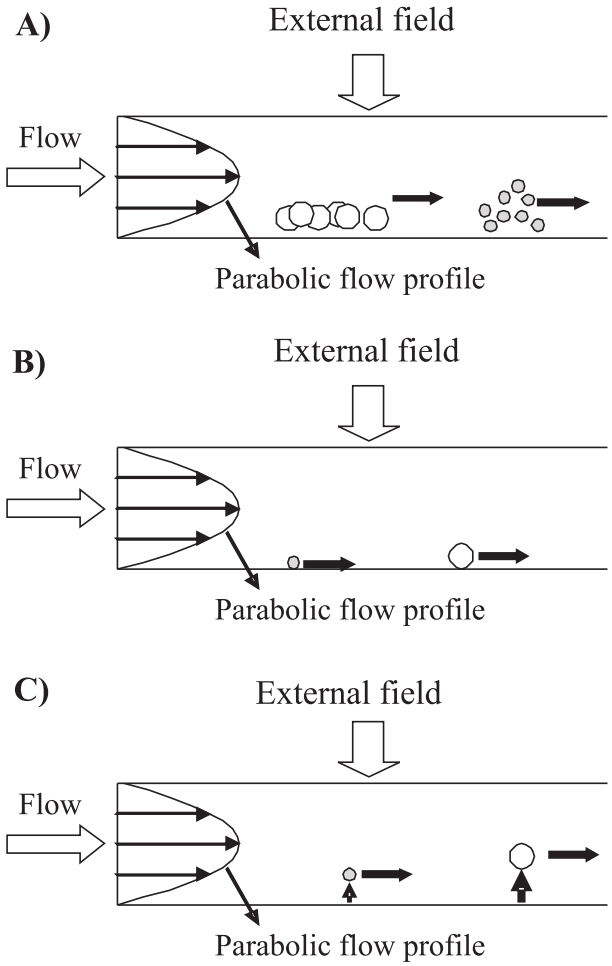

Figure 2.13: Schematic diagram shows the mechanisms of particle separation in A) normal mode, B) steric mode, and C) hyperlayer mode of FFF.

partly opposed by Brownian diffusion that makes the particles move away from the wall. Consequently, the smaller particles with larger diffusivity have higher probability to move to the middle of the channel, and therewith, to the faster streamlines of the parabolic profile resulting in the shorter residence times [35]. Figure 2.13A shows the mechanism of particle separation in normal mode.

In the steric mode FFF operates on larger particles, with particle size around 0.5-10 μm, where Brownian diffusion is too weak to oppose the particle build up [1, 36]. The particles accumulate now while forming a thin layer. Larger particles protrude out of this thin layer. Via steric interactions they can leave the thin layer, and enter faster streamlines, resulting in smaller residence times than smaller particles (see figure 2.13B). The residence time for the steric mode depends only on the size of the particle

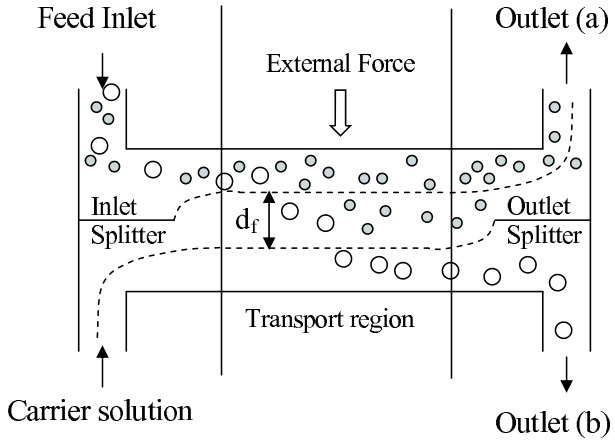

Figure 2.14: Schematic representation of a SPLITT system.

[35].

For the larger particles (> 10 μm), particle accumulation on the wall is opposed by the hydrodynamic lift force acting on single particles [1, 35, 36]. The distance that they are lifted away from the wall is greater than their diameters (see figure 2.13C). The residence time in this hyperlayer mode depends not only on particle size, but also on the physical properties of the particle (e.g. shape, deformability), which jointly affect the intensity of the hydrodynamic lift force [35, 37].

FFF can be used for fractionating a very broad size range of particles of around 1 nanometer to 100 μm [36, 38]. However, this device is not favorable for large scale application due to its batch-wise operation.

Split-flow thin, SPLITT

Split-flow thin (SPLITT) fractionation is a technique quite similar to FFF but is operated in a continuous way. The SPLITT microchannel has so-called splitters at both inlet and outlet (see figure 2.14), which create three flow lanes in the microchannel between inlet and outlet. The size of the flow lanes depends on the flow rates at the inlet and outlet channels. The distance between the dividing streamlines is d_f, with the streamlines starting or ending at the inlet/outlet splitters, which act as stagnation points.

The particle suspension is introduced into the feed inlet channel, and a carrier fluid is introduced into the other inlet channel albeit at different velocity (see figure 2.14) [39–41]. In general, the flow rate of the carrier fluid is higher than the flow rate of the particle suspension.

In contrast to flow line sieving, the fractionation is not via steric interactions, but via the external force field. Particles that are not or slightly affected by the force fields, remain in their flow lane and are transported to outlet (a). Particles that are affected by the external forces, and also cross the distance, d_f, to the outer flow lane in the transport region leave at outlet (b) [42]. This fractionation is based on the effect of the external force on particle properties other than size [42, 43]. For instance by using an electric field, the fractionation depends on the dielectric properties of particles.

The yield is high compared to FFF due to the continuous operation. The selectivity depends on the effect of the force on the particles. Within the residence time of particles in the transport region, they have to cross the distance d_f between dividing streamlines. Via controlling the flow rate one can change d_f and thus the selectivity. For small particles the selectivity can also be imparted by Brownian motion. For concentrated suspension steric interactions (leading to shear-induced diffusion) can also impart the selectivity.

Dielectrophoresis, DEP

Dielectrophoresis, DEP, is the movement of dielectric particles across a fluid by application of a non-uniform AC electric field. An interaction between the dielectric particle and an electric field causes this movement [44, 45]; the strength and direction of this interaction depends on the dielectric properties of particles and fluid [46, 47]. The electric field is applied perpendicular to the flow lines. The average DEP force, F_{DEP} acts on the particle as follows [47, 48]:

$$F_{DEP} = 2\pi r^3 \varepsilon_w Re(f_{CM}) \bigtriangledown E^2 \tag{2.2}$$

Where r is the radius of the particle, ε_w is the dielectric constant of the surrounding fluid, and E is the electric field. $Re(f_{CM})$ is the real part of the polarization factor for which the Clausius-Mossotti relation holds

$$f_{CM} = \frac{\varepsilon_c^* - \varepsilon_w^*}{\varepsilon_c^* + 2\varepsilon_w^*} \tag{2.3}$$

ε_c^* and ε_w^* are the frequency dependent complex dielectric permittivities of particle and surrounding fluid, respectively.

Particles having a higher dielectric permittivity than the fluid ($Re(f_{CM}) > 0$), move to a region with stronger electric field; this is called positive DEP. In contrast, for

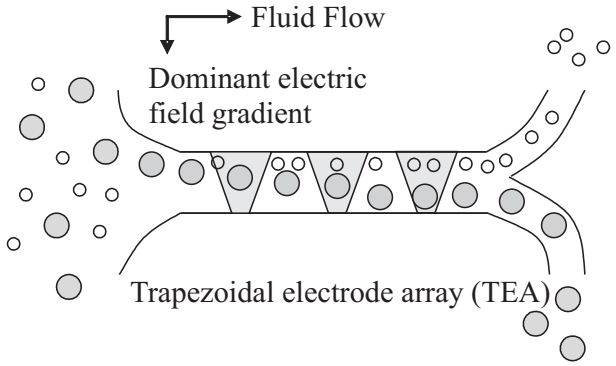

Figure 2.15: Schematic view of a trapezoidal electrode array (TEA) for dielectrophoretic fractionation of particles.

negative DEP, particles with a lower dielectric permittivity than the fluid ($Re(f_{CM}) < 0$), move to a region with a weaker electric field [46, 47].

During positive DEP, particles are attracted to electrodes [48, 49]. The positive DEP is not appropriate for continuous fractionation due to particle accumulation at the electrodes in the microchannel. The opposite is true for the negative DEP, particles are repelled by the electrodes [49].

Choi et al., [48] invented a trapezoidal electrode array (TEA) to separate polystryrene beads with different dielectric properties by negative DEP. The fractionation of particles depends on the dielectrophoretic force exerted by the electric field and the drag force exerted by the fluid velocity. If the dielectric force is sufficient, the particles will be fractionated to the output channels. Figure 2.15 shows a schematic view of TEA for dielectrophoretic separation of particles. The electrode is made in trapezoidal shape and generates an electric field gradient. In the devices, electrodes are placed near or in the fluid stream to exert a driving force on the particles.

The yield of this device is quite high due to the absence of objects in the microchannel, leading to low particle accumulation. The selectivity depends on the difference in dielectric properties and size of the particles, cf. Eq.(2.2).

Ultrasonic separation, US

Ultrasonic fields give two types of acoustic forces, called primary and secondary acoustic forces, and suspended particles are affected by them. The primary acoustic force acts directly on the particles and is used for fractionation. The secondary acoustic force causes interaction between particles, which are attracted or repulsed. This force

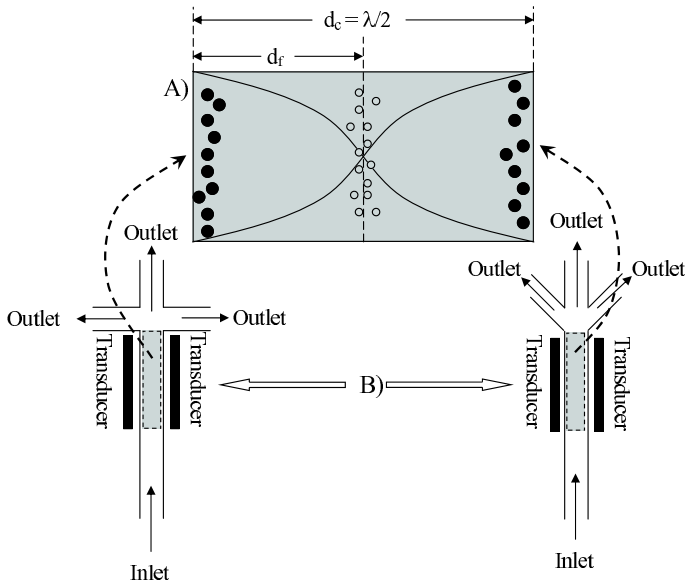

Figure 2.16: A) Primary acoustic force moves particles toward a node (the centre of the channel) or anti-node (the wall side of the channel). B) Schematic view of particle separation by ultrasound in the device with one inlet and three outlets.

is usually negligible compared to the primary force [50].

The acoustic field accumulates the particles in nodes or anti-nodes of the standing acoustic wave. Equation 2.4 expresses the force on a particle.

$$F_u = -\frac{\pi p_0^2 V_p \beta_w}{2\lambda_u} \phi_{uc}(\beta, \rho) \cdot sin(2kx) \tag{2.4}$$

$$\phi_{uc} = \frac{5\rho_c - 2\rho_w}{2\rho_c + \rho_w} - \frac{\beta_c}{\beta_w} \tag{2.5}$$

Where ρ_w and ρ_c are the densities of the medium and the particle, respectively, β_w and β_c are the corresponding compressibilities, p_0 is the pressure amplitude, V_p is the volume of the particle, λ_u is the ultrasonic wavelength, ϕ_{uc} is the acoustic contrast factor, k is defined as $2\pi/\lambda_u$, and x is the distance from the pressure node. ϕ_{uc} is used to show the direction of the force. If ϕ_{uc} is positive, the direction is toward a pressure node. If ϕ_{uc} is negative, the direction is toward a pressure anti-node.

Figure 2.16A shows a cross-section area inside the devices (gray boxes) in which the channel width, d_c, is equal to one half of the frequency wavelength. The pressure node is at the centre of the channel and the anti-node is at the wall side of the channel.

There is one main inlet channel and three outlets in the device (see figure 2.16B). Suspensions are injected into the main channel having the standing wave region. If

the density and compressibility of the particle are appropriate compared to the carrier fluid, particles will move toward the node or the anti-node. For example, if the particles are red blood cells or lipid droplets in blood plasma, the erythrocytes (cells) move toward the node and the lipid particles move toward the anti-node [52]. This is interesting for food applications, especially milk where milk fat is to be fractionated from bacteria - which have comparable size. At the outlet, particles gather in the node, and move through the centre of the central outlet. Particles, gathering in the anti-node, move via the walls toward the outer outlets.

Ultrasonic separation can be used to fractionate particles of size $0.1\mu m < d_p < 10\mu m$ [53]. The fractionation depends on the density and compressibility of the particles and carrier fluid [51, 52]. The difference between particles has to be such that the factor ϕ_{uc} has opposite signs for the two types of particles. The selectivity is increased by reducing the flow rate exposing the particles longer to the standing wave field, but this will reduce the yield. The use of highly concentrated suspensions needs strong acoustic force, but this also leads to particle trapping in the flow channel [53].

2.4.4 Devices using trapping force fields

Via externally applied inhomogenous force fields, particles can be trapped or deflected by regions having a local extreme in the force field. The inhomogenity of the force field is characterized by the length scale d_f, and fractionation occurs if $d_{p1} < 2d_f < d_{p2}$, or if particles differ significantly in other physical properties relevant to the trapping force field.

Holographic optical tweezers, HOTs

Optical tweezers are created by strong focusing of a laser beam. The optical tweezers can be used to trap or deflect particles in a fluid [54, 55]. The focused beam creates an electric field with a very strong gradient, which traps the particles. The expression for the trapping force is identical as for DEP [71]:

$$F = \frac{-3\varepsilon_w}{2}\frac{\varepsilon_c - \varepsilon_w}{\varepsilon_c + 2\varepsilon_w}V_p \bigtriangledown_r \mid E^2(r) \mid \tag{2.6}$$

Where ε_w and ε_c are the dielectric constants of the surrounding fluid, and particle, respectively. V_p is the volume of the particle, and E is the electric field. Next to the gradient force, there is also a force due to radiation pressure, which moves the particle

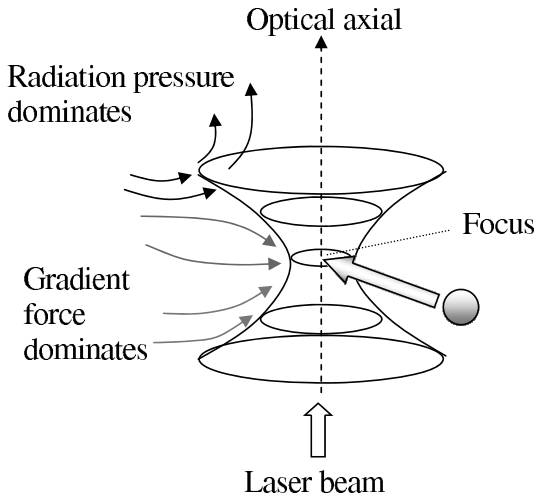

Figure 2.17: Optical tweezers use a strongly focused beam of laser light to trap a particle.

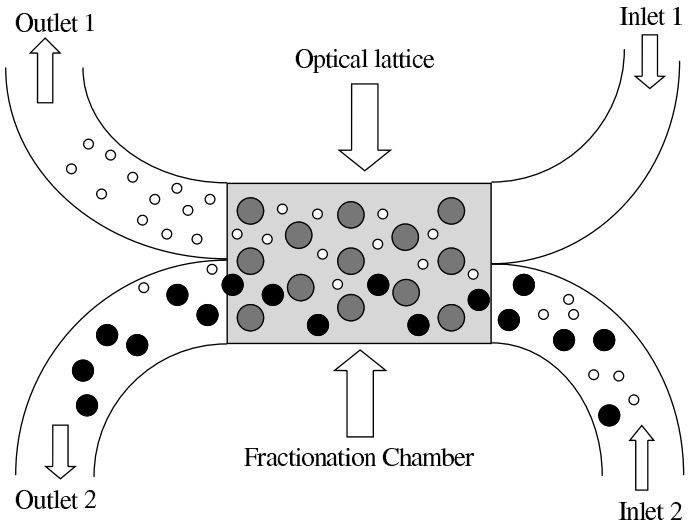

Figure 2.18: Schematic representation of optical fractionation.

along the optical axis (see figure 2.17).

Optical fractionation uses holographic optical tweezers, HOTs, computer generated holograms to create multiple optical tweezers, which can simultaneously trap or deflect particles [55–57]. If HOTs arranges the optical tweezers into an array, they operate very similar to deterministic ratchets, as shown in figure 2.18. Via the gradient forces of the optical tweezers a periodic energy landscape is created, which can be used for fractionation with very high selectivity [57].

The set up of a optical fractionation device is much like a SPLITT device, where the

carrier fluid is fed to inlet 1, and the suspension fluid is fed into inlet 2. The particles are driven through the potential field created by the array of optical tweezers. The array of optical tweezers might be similar to the structures found in deterministic ratchets or a single inclined line of traps [30, 55, 56].

Particles that are strongly affected by the gradient force, as compared to their drag force, will change direction from the original trajectory and move to outlet 1. Particles that are not affected by the gradient force will continue to follow their streamline and end up in outlet 2.

HOTs can trap particles ranging in size from $10nm < d_p < 10\mu m$ [56, 58]. Due to the structures of the device, the yield is similar to SPLITT, while the selectivity is similar to deterministic ratchets. When particles accumulate in the trapping structure due to the use of concentrated suspensions, this can be solved by turning the trapping power off; this makes the trapping structure disappear, but resolves the accumulation of particles. This make HOTs a quite promising technique with in-situ cleaning facilities. However the optical equipment is expensive, and the creation of the optical tweezers requires a high amount of energy.

Dielectrophoretic traps, DT

DEP force is used as a lateral displacement force in the previous section, but it can be also used as a trapping force. The expression for trapping is identical to that used in HOTs and DEP. DT differs in frequency from HOTs due to frequency dependence of dielectric properties. Here the trapping forces are via electrodes [59–62]. The DT can use either positive or negative DEP. By using positive DEP, particles are pulled towards the electrodes. In contrast, particles are pushed away from the electrodes by using negative DEP.

The trapping position of positive DEP is at a field maximum, typically at the electrode surface or at field constrictions. Positive DEP traps need particles suspended in an artificial low-conductivity media [59, 62], which makes it hardly applicable for food suspensions.

In contrast, the trapping position of negative DEP is at a field minimum away from electrodes which pushes a particle from all sides via the electrode geometry. Negative DEP traps can be used with normal media. However if the media has a high conductivity a significant amount of heat can be dissipated in the fluid [62, 63]. Heat dissipation is generally not desired in food fractionation applications, since foods are

heat sensitive.

Optoelectronic tweezers, OET

This device creates also trapping fields, which create the same gradient force field as in HOTs, and DT. The difference with previous devices is that the trapping field is created via conversion of an optical field into an electric field via optoelectrodes, which create an electric field upon illumination by laser light. The advantages of OET is the lower energy requirement compared to HOTS [64, 65].

The structure of OET consists of an upper transparent conductive and a lower photoconductive surface in which an alternating current (a.c.) bias is applied between the surfaces. Suspensions will be fed into the space between these two parallel surfaces. When light projects on the photoconductive layer, this creates a virtual electrode with a non-uniform electric field for manipulating particles. The particles can be attracted by or repelled from the projected light area due to the DEP forces [64].

2.5 Performance indicators

In the previous sections we have discussed microfluidic devices for fractionation of suspensions. In this section, we describe how to quantify their performance indicators, i.e. yield, particle accumulation and selectivity. For a fair comparison we will evaluate the performance for a collection of devices fitted in a particular volume, say $V = 1m^3$. The objective of the envisioned process is to fractionate a bidisperse suspension of non-deformable particles with diameter $d_{p1} < d_{p2}$. Fractionation will be based on size.

The topology of the process is shown in figure 2.19. The process will have two inlets, one with the feed with the bidisperse suspension, and optionally another with a carrier fluid. Furthermore, the process has two outlets, the permeate and the retentate (for the terminology we follow membrane technology). Ideally, the permeate and retentate will have only one type of particle, that we like to fractionate. In our evaluation we will compare only the performance of retentate because the yield is limited by the accumulation of large particles. We will require that the selectivity is at least $S_f = 95\%$, i.e. each outlet should contain at least 95% (volume fraction) of one kind of particle.

As shown in figure 2.19, we have defined the flow rates of the feed (ϕ_f), the carrier fluid (ϕ_c), the permeate (ϕ_p), and the retentate (ϕ_r). The carrier fluid is without

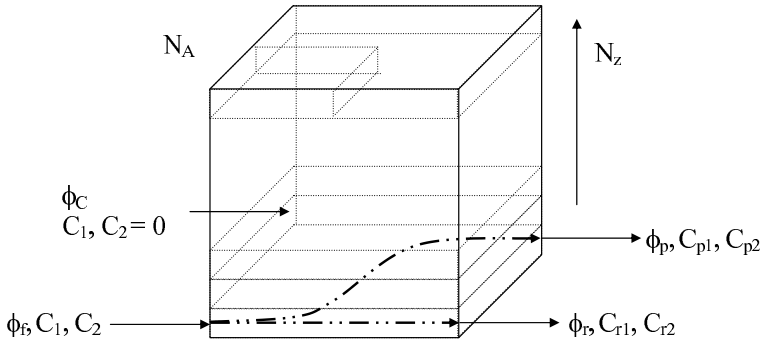

Figure 2.19: A cubic meter for evaluating devices

.

particles, and the volume fractions of particles in the feed are C_1 and C_2 (with index 2 referring to the particle that needs to be separated from particle 1). In the permeate the volume fractions are C_{p1} and C_{p2}, and in the retentate the volume fractions are C_{r1} and C_{r2}.

If the fractionation process allows, the devices will be stacked on top of each other. Each layer is assumed to be the size of a silicon wafer. Between the silicon wafers, there are spacers - having conduits (manifolds) connecting the inlets and outlets to the individual devices. Hence, they interface the meter scale of the factory to the micrometer scale of the microfluidic devices. We assume the spacers to be 5 mm thick. Note, that the spacers determine the number of wafers which can be stacked (if the process allows them to be stacked). The number of stacks will be indicated by N_z.

On each layer, a number of microfluidic devices can be placed, which will be indicated with N_A. If a single device can not achieve the required selectivity of 95%, several devices need to be connected in series. For this number N_s will be used.

2.5.1 Yield

In this section we will derive a dimensionless expression for the yield of a particular device, which will be used for quantitative evaluation of the devices. Assuming, that selectivity of 95% is achieved, the yield (Y) of a particular process is defined as $Y = \phi_r C_{r2}$, having as units $[m^3/\text{s}]$. To make it dimensionless we divide it by the volume V and multiply it with the processing time t_e. Processing time is defined as the fraction of the day the process can continuously operate (the other fraction of the day is then assigned to required cleaning e.g.). Hence, the dimensionless yield is equal to:

$$Y^* = \frac{\phi_r C_{r2} t_e}{V} \tag{2.7}$$

The total flow rate of the retentate is calculated from the number of devices available in the volume V, $N_z \times N_A$, with correction for the number of devices put in series to obtain the required selectivity N_s and the flow rate for a single devices, $\phi_{r,i}$:

$$\phi_r = \frac{N_z N_A}{N_s} \phi_{r,i} \tag{2.8}$$

2.5.2 Particle accumulation

Particle accumulation in the fractionation device is unfavourable since it always will reduce the yield and the selectivity. These effects, which are often called fouling, are the main problem in separation and fractionation processes with membranes, and it is expected that it will also be the main issue when using concentrated suspension in microfluidic devices. Belfort et al., [6] used the diameter of the particle, d_p, and the pore diameter of the membrane, d_s, to categorize fouling into 3 cases: (1) adsorption ($d_p \ll d_s$), (2) pore plugging or hydrodynamic bridging ($d_{p2} \leq d_s$), and (3) cake layer formation ($d_{p2} \geq d_s$, pores are covered).

The same effects are expected to be present in any microfluidic device. The local flow velocities affect the adsorption of particles to the wall and plugging of pores and channels. In our definition, adsorption only occurs if $d_p \ll d_s$. Particles smaller than the pore or channel size, can enter and build an extra resistance inside the pore or channel when the fluid velocity is low (see figure 2.20). The deposition of particles is a result of attraction between the particle and the surface. At increased velocity, adsorption will be less [66].

Although adsorption of particles may be less at higher velocity, at the same time plugging by hydrodynamic bridging will increase, and this can affect transmission unfavourably. The plugging phenomenon occurs when the flow velocity is higher than a critical velocity [66, 67]. Although $d_s \geq d_{p2}$, plugging can also occur at low Reynolds numbers due to hydrodynamic bridging [66]. Figure 2.21A. shows plugging by a single particle when $d_s = d_{p2}$. Figure 2.21B. shows particle plugging by hydrodynamic bridging when $d_s \gg d_{p1}$. Hydrodynamic bridging is the phenomenon that particles, smaller than the pore or channel size, arrive simultaneously and block the pore or channel.

Ramachandran and Fogler [66] presented the colloidal repulsion force, F_{col}^{p-p}, and

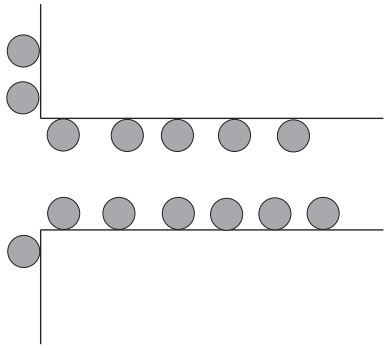

Figure 2.20: Deposition of particles within a pore of a membrane.

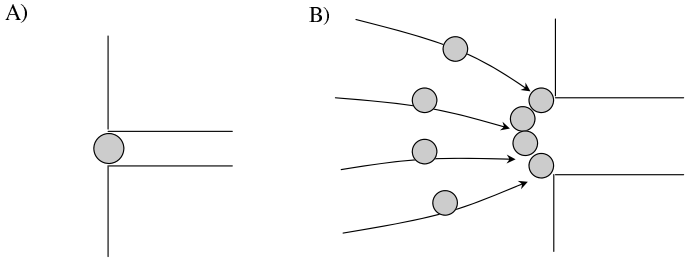

Figure 2.21: Sketch of hydrodynamic bridging by particle.

the drag force, F_{drag} which affect hydrodynamic bridging. The colloidal repulsion forces between two charged particles are based on the DLVO theory consisting of van der Waals attraction and electrostatic repulsion. The mean potential expressions for short-range repulsion between particles, constructed from the repulsive parts of interatomic potentials, is derived by Feke et al. [68]. If the drag force, acting on particles at the entrance, is greater than the colloidal repulsion force between the particles, plugging by hydrodynamic bridging will occur [67]: $F_{drag}/F_{col}^{p-p} > 1$. The experimental result of Ramachandran and Fogler [66], shows that the critical ratio of the pore or channel size to the particle size:

$$\frac{d_s}{d_{p2}} = 3 - 4 \tag{2.9}$$

Below this ratio, particles can permeate through the pores or channels without plugging. Whether this also happens, is determined by the critical velocity. Hydrodynamic bridging does not occur if the velocity is lower than the critical velocity. In this case, the drag force is less than the interparticle colloidal repulsion forces. The critical velocity will depend on the critical ratio, flow geometry, surface properties of the particle and of the pore or channel [66]. Bridging or plugging is expected to be

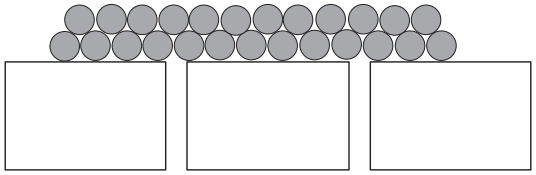

Figure 2.22: Cake layer formation

.

the main cause for losses in yield and in selectivity in microfluidic devices due to their structure, $d_s > d_{p2}$.

The probability of plugging, P_f, depends on the volume fraction of (large) particles in the feed flow and the ratio of the cross section area of particle to the cross section area of a pore or channel. For lower A_s/A_{p2}, the probability of plugging will be higher and this is also the case for higher volume fraction of particles. These effects are summarized in:

$$P_f = C_2^{\frac{A_s}{A_{p2}}} \tag{2.10}$$

For the evaluation, it is assumed that P_f is 1×10^{-27} for each device. This value is estimated from the separation experiment with microsieve membranes by Brans et al., with 0.1% particle suspensions [5]. For optimized microsieve pores, d_s/d_{p2}, is around 3-5 [69], which is in agreement with equation 2.9. When the pore shape is circular, A_s/A_{p2} is equal to $(d_s/d_{p2})^2$.

In this paper we assume that cake layer formation occurs when $d_p > d_s$, or after d_s is reduced due to adsorption or plugging by hydrodynamic bridging until $d_p > d_s$. Particles cannot penetrate the membrane and they will accumulate on the surface of the membrane where they form a cake layer (see figure 2.22). This will reduce the permeate flux and selectivity of the fractionation in time. Although applying a high shear by suspension flowing tangential to the membrane surface, can reduce particle accumulation, the cake layer still remains [1].

2.5.3 Selectivity

For a good fractionation, the outlet flows of permeate and retentate should contain $C_{p1} \gg C_{p2}$ and $C_{r1} \ll C_{r2}$. In our evaluation, we will compare the yield of each device for the same final selectivity of the retentate, S_f (at least 95%). However the selectivity of the retentate of each device, S_r is not equal. S_r of some devices is more

or equal to 95% by fractionation in a single device ($N_s = 1$), whereas some devices need several in series to reach the same S_f. S_f is defined as follows.

$$S_f = 1 - (1 - S_r)^{N_s} \tag{2.11}$$

For $C_1 = C_2$ in the feed, the equation for S_r is:

$$S_r = \frac{C_{r2}}{C_{r1} + C_{r2}} \tag{2.12}$$

$$C_{r2} = CO_{ret} \cdot C_2 \tag{2.13}$$

$$C_{r1} = (1 - CO_{per}) \cdot C_1 \tag{2.14}$$

Where CO_{ret}, is the retention coefficient that is indicative for the recovery of the large particles in the retentate flow, and CO_{per} is the permeation coefficient, which is indicative for the recovery of the small particles in the permeation flow.

2.6 Evaluation

In the previous section we have given relations for performance indicators. In this section we quantify the performance of each device. However our evaluation will be restricted to the devices which can operate in continuous mode. We assume that for all devices except BR, a single device of each process is operated with constant flow rates of the feed ($\phi_{f,i}$), carrier fluid ($\phi_{c,i}$), permeate ($\phi_{p,i}$), and retentate ($\phi_{r,i}$), which are expected to be in the order of 10^{-11} m^3/s. For a cross-section at area $A \approx 10^{-7}m^2$, the typical velocity is in the order of 10^{-4} m/s in microfluidic devices. For this flow rate, the Peclet number (Eq. 2.15) $Pe \gg 1$; hence the selectivity is not affected by Brownian motion. In BR, Brownian motion is the driving force, and hence $Pe \ll 1$. Consequently the velocity is in order of 10^{-6} m/s and the flow rates are in order of $10^{-13}m^3$/s [25]. The Peclet number is the ratio of the diffusion time of Brownian motion, τ_2, to the retention time of velocity of the fluid flow, τ_1.

$$Pe = \frac{\tau_2}{\tau_1} = \frac{d_f^2}{D} \cdot \frac{U}{L_x} \tag{2.15}$$

Where L_x is the distance that a particle moves with velocity of fluid, U; d_f is the distance that a particle moves away from the direction of U by Brownian diffusion, D, which is calculated from Eq 2.1.

The number of devices that can be placed in a volume of 1 m^3 is estimated for each device. From the literature data, we know that on a wafer area of 1 m^2 N_A are in the range of 10^4 for Membranes, BR, DR, HOTs, DT, and OET [4, 18, 25, 26, 28, 30, 56, 64], while N_A are in the range of 10^3 for other devices [33, 35, 36, 39, 40, 43, 48, 51, 52]. This is because HF and AsPFF need more space for side channels, while drag forces are greater than external forces in SPLITT, DEP, and US, therefore they need longer channels to exert external force fields for fractionation. For space efficiency, each device is stacked, where N_z is the number of layers in the device of 1 meter height. N_z of each device is 200, except for the HOTs where N_z is 1 because it can not be stacked due the need for light illumination from above.

From equation 2.10 we can estimate the volume fraction based on the probability of particle plugging, if we know the ratio of A_{p2} to A_s. For the membrane, we choose $d_{p2}/d_s = 0.33$ which is the largest ratio recommended in literature [66, 69]. So $A_{p2}/A_s = 0.11$. For other devices we assume the depth of the channels, h, are around 10 times d_{p2}. For Brownian and deterministic ratchets, $d_{p2}/d_s \approx 0.33$. Also we assume that the structures of devices using trapping force fields are created similar to Brownian and deterministic ratchets (but can be removed), so $A_{p2}/A_s \approx 0.026$. d_{p2}/d_s of HF and ASPFF is around 0.2, so $A_{p2}/A_s \approx 0.016$. For devices using external force fields for lateral displacement ($d_c = d_s$), there are no solid obstacles inside the channel, so we assume that d_s is around 10 times d_{p2}: $d_{p2}/d_s \approx 0.1$ and therewith A_{p2}/A_s is around 0.008.

The selectivity of each device depends on the recovery of small and large particles in permeate and retentate flows, which can be determined from the permeation and retention coefficient. From the literature values, retention and permeation coefficients are known or estimated as shown in table 2.1.

Besides parameters related to the fractionation also operation time has to be taken into account for the evaluation; t_e is the operating time per day. For most devices it can be assumed that they can be operated continuously without stopping for cleaning and therefore: $t_e = 86400s$. The operation of microsieve membranes is continuous, but it has to be stopped for cleaning and we assumed that this takes one-third of the day: $t_e = 57600s$.

The concentrations shown in Table 2.2 are calculated with equation 2.10. However at concentration $C_2 > 0.2$, we expect shear-induced diffusivities to be significant [70], which will lower selectivity similar to Brownian diffusion. Hence we keep C_2 restricted

Table 2.1: The permeation and retention coefficient values of each device

Devices	CO_{per}	CO_{ret}
Membrane	0.85	1.0
Brownian Ratchets, BR	0.95	0.95
Deterministic Ratchets, DR	0.95	0.95
Hydrodynamic Filtration, HF	0.65	0.80
Asymmetric Pinch Flow Fractionation, AsPFF	0.75	0.85
Split-flow Thin, SPLITT	0.80	0.90
Dielectrophoresis, DEP	0.85	0.90
Ultrasound Separation, US	0.85	0.90
Holographic Optical Tweezers, HOTs	0.95	0.95
Dielectrophoretic Traps, DT	0.95	0.95
Optoelectronic Tweezers, OET	0.95	0.95

to $C_2 \leq 0.2$ for the estimation of the yield.

In Table 2.2, all devices that we have discussed in the previous sections are summarized together with the characteristics needed for the evaluation. Some devices can fractionate poly-disperse particles in a single pass by using multiple output channels, while other devices only use two outlets and therefore only two fractions can be obtained (see Table 2.2). Depending on the number of outlets (fractionation in multiple fractions ≥ 2) that are required this could already limit the number of devices, which are suited for that specific fractionation.

Membrane devices suffer from particle accumulation due to $d_{p1}<d_s<d_{p2}$ leading to the use of very low concentration ($C_2 = 0.001$). The yield of membrane devices is also quite low. Compared to other devices, membranes are not really suited for fractionation.

Brownian ratchets are a promising technique for small particles ($d_p \approx 100$ nm) having less particle accumulation due to $\{d_{p1}, d_{p2}\} < d_s$. The concentration is moderate. The yield is low because of the operating regime $Pe \ll 1$.

Flow line sieving devices have less particle accumulation similar to Brownian ratchets due to their structures. The concentration in these devices is moderate. The yield of flow line sieving devices depends strongly on their designs. The selectivity of DR is higher than HF and AsPFF. DR is very promising for fractionation of polydisperse particles $> 1\mu$m.

Devices using external force fields for lateral displacement have the least problem with particle accumulation compared to other devices due to d_{p1},$d_{p2} \ll d_s$, so they can

Table 2.2: Evaluating performance of each device

Devices	Particle size	Ext. energy	Outlet	(C_2)	log (Y^*)
Membrane	$d_{p1} < d_s < d_{p2}$	No	2	0.001	-3
BR	$d_{p1}, d_{p2} < d_s$	No	>5	0.20	-2
DR	$d_{p1}, d_{p2} < d_s$	No	>5	0.20	0
HF		No	>5	0.40*	-2
AsPFF		No	5	0.40*	-2
SPLITT	$d_{p1}, d_{p2} \ll d_s$	Yes	2	0.60*	-2
DEP		Yes	2	0.60*	-2
US		Yes	2	0.60*	-2
HOTs	$d_{p1}, d_{p2} < d_s$	Yes	2	0.20	-1
DT		Yes	2	0.20	0
OET		Yes	2	0.20	0

Note:* These concentrations are calculated from geometric structure and particle size. We take maximum value of $C_2 = 0.2$ for evaluating Y^* because this is the minimum value which can generate shear-induced diffusivities [70].

fractionate very highly concentrated suspensions. However, the yields are not very high because the devices need longer channels than other devices due to relative weakness of the external force compared to the drag force.

In devices using trapping force fields, particle accumulation is similar to flow line sieving devices. The concentration is also moderate. The advantage of these devices is that they can solve the particle accumulation issues by removing the trapping structures. However they require more energy than other devices. The yield of optical devices will be high, if the layers of optic devices can be stacked, using LED displays fabricated via microtechnology [72].

Table 2.2 shows that the deterministic ratchets are most promising for fractionation of concentrated suspensions (e.q. foods or biotechnology). Although some devices using trapping force fields can give high yields, and low particle accumulation and moderate concentrations can be used similar to deterministic ratchets, their operation needs more energy for trapping.

2.7 Conclusions

In summary, we have evaluated quantitatively different classes of microfluidic devices and membranes for fractionation of concentrated suspensions. All classes show

different behaviors, but are within a class mostly quite similar. Microfluidic devices are applicable for fractionation of concentrated suspensions with less particle accumulation problems compared to membranes. Brownian ratchets are suited for fractionation of small particles ($d_p < 1\mu$m). Flow line sieving devices can fractionate polydisperse suspensions. Further devices may use other properties than size to separate and are based on external force fields i.e. dielectric properties of protein. At the moment, the deterministic ratchet seems to be most promising. One has to keep in mind that ratchets were first applied for dilute bio-molecule separations, but they definitely also show great potential for particle fractionation in concentrated (food) suspensions.

List of symbols

A_s	the cross section area of a pore or channel
A_{p2}	the cross section area of large particle
C_1	the volume fractions of small particle in feed
C_2	the volume fractions of large particle in feed
C_{p1}	the volume fractions of small particle in permeate
C_{p2}	the volume fractions of large particle in permeate
C_{r1}	the volume fractions of small particle in retentate
C_{r2}	the volume fractions of large particle in retentate
CO_{per}	the permeation coefficient
CO_{ret}	the retentation coefficient
d_c	the width of the flow channel
d_f	the length scale of the flow structure
d_s	the smallest distance between solid obstacles or the pore diameter of a membrane
d_{p1}	the diameter of small particle
d_{p2}	the diameter of large particle
D	the diffusion coefficient
E	the electric field
F_{DEP}	the average DEP force
F_u	the acoustic force
f_{CM}	the polarization factor of the Clausius-Mossotti relation
k	the Boltzmann constant
L_x	the distance that particle moves with the velocity of fluid
N_A	the number of devices that can be placed on each layer
N_s	the number of devices put in series
N_z	the number of stacks
P_f	the probability of plugging
p_0	the pressure amplitude
Pe	the Peclet number
S_f	the final selectivity of the retentate
S_r	the selectivity of the retentate in a single device

r	the radius of particle
T	the temperature
t_e	the processing time
U	the velocity of fluid
V_p	the volume of the particle
V	the volume of evaluating devices [1 m^3]
Y	the yield
Y^*	the dimensionless yield
η	the viscosity
ε_w	the dielectric constant of the surrounding fluid
ε_c	the dielectric constant of the particle
ε_w^*	the frequency dependent complex dielectric permittivity of surrounding fluid
ε_c^*	the frequency dependent complex dielectric permittivity of particle
ρ_w	the density of the surrounding fluid
ρ_c	the density of the particle
β_w	the corresponding compressibility of the surrounding fluid
β_c	the corresponding compressibility of the particle
λ_u	the ultrasonic wavelength
ϕ_{uc}	the acoustic contrast factor
ϕ_f	the flow rate of the feed
ϕ_c	the flow rate of the carrier
ϕ_p	the flow rate of the permeate
ϕ_r	the flow rate of the retentate
τ_1	the retention time of velocity of the fluid flow
τ_2	the diffusion time of Brownian motion

References

[1] G. Belfort, R.H. Davis, and A.L. Zydney, *J. Membr. Sci.*, **96** (1994) 1-58.

[2] A.N. Sharpe, P.I. Peterkin, and I. Dudas, *Appl. Environ. Microbiol.*, **37(1)** (1979) 21-35.

[3] C. Bang-xiao, *Filtration & Separation*, **42** (2005) 33-35.

[4] G. Brans, C.G.P.H. Schroën, R.G.M. van der Sman, and R.M. Boom, *J. Membr. Sci.*, **243** (2004) 263-272.

[5] Brans G, Design of membrane systems for fractionation of particle suspensions. *PhD. Thesis, Wageningen University, The Netherlands*, 2006.

[6] G. Belfort, J.M. Pimbley, A. Greiner, K.Y. Chung, *J. Membr. Sci.*, **77** (1993) 1-22.

[7] G. Brans, J. Kromkamp, N. Pek, J. Gielen, J. Heck, C.J.M. van Rijn, R.G.M. van der Sman, C.G.P.H. Schroën, and R.M. Boom, *J. Membr. Sci.*, **278** (2006) 344-348.

[8] G. Brans, A. van Dinther, B. Odum, C.G.P.H. Schroën, and R.M. Boom, *J. Membr. Sci.*, **290** (2007) 230-240.

[9] J. Kromkamp, F. Faber, C.G.P.H. Schroën, and R.M. Boom, *J. Membr. Sci.*, **268** (2006) 189-197.

[10] K.D. Rausch, *Starch/Stärke*, **54** (2002) 273284.

[11] J.C.T. Eijkel, and A. van den Berg, *Electrophoresis*, **27** (2006) 677-685.

[12] J.C.T. Eijkel, and A. van den Berg, *Lab on a Chip*, **6** (2006) 19-23.

[13] E. Chmela, R. Tijssen, M.T. Blom, H.J.G.E. Gardeniers, and A. van den Berg, *Anal. Chem.*, **74** (2002) 3470-3475.

[14] G. Stegeman, J.C. Kraak, and H. Poppe, *J. Chromatogr.*, **550** (1991) 721-739.

[15] S. Kuiper, C.J.M. van Rijn, W. Nijdam, G.J.M. Krijnen, and M.C. Elwenspoek, *J. Membr. Sci.*, **180** (2000) 15-28.

[16] J. Kromkamp, M. van Domselaar, C.G.P.H. Schroën, R.G.M. van der Sman, and R.M. Boom, *Desalination*, **146** (2002) 63-68.

[17] M.Girones, Z. Borneman, R.G.H. Lammertink, and M. Wessling, *J. Membr. Sci.*, **259** (2005) 55-64.

[18] S. Kuiper, C.J.M. van Rijn, W. Nijdam, O. Raspe, H. van Wolferen, G. Krijnen, and M. Elwenspoek, *J. Membr. Sci.*, **196** (2002) 159-170.

[19] P. Poesio, and G. Ooms, *Journal of Petroleum Science and Engineering*, **45** (2004) 159-178.

[20] M. Mosbacher, H. J. Münzer, J. Zimmermann, J. Solis, J. Boneberg, and P. Leiderer, *Appl. Phys. A* **72** (2001) 41-44.

[21] J. Kromkamp, A. Bastiaanse, J. Swarts, G. Brans, R.G.M. van der Sman, and R.M. Boom, *J. Membr. Sci.*, **253** (2005) 6779 .

[22] C.F. Chou, O. Bakajin, S.W.P. Turner, T.A.J. Duke, S.S. Chan, E.C. Cox, H.G. Craighead, and R.H Austin, *PNAS*, **96** (1999) No. 24, 13762-13765.

[23] C. Keller, F. Marquardt, and C. Bruder, *Phys. Rev. E*, **65** (2002) 041927.

[24] A. Abdulle, and S. Attinger. (*http* : *//www.math.unibas.ch/preprints*03/*preprint*2003−18.*pdf*).

[25] L.R. Huang, E.C. Cox, R.H. Austin, and J.C. Sturm, *Anal. Chem.*, **75** (2003) 6963-6967.

[26] S. Matthias, and F. Müller, *Nature*, **424** (2003) 53-57.

[27] F. Müller, A. Bitner, J. Schilling, U. Gösele, C.H. Kettner, and P. Hänggi, *Phys. Status Solidi A*, **182** (2000) 585.

[28] C. Kettner, P. Reimann, P. Hanggi, and F. Müller, *Phys. Rev. E*, **61** (2000) 312-323.

[29] L.R. Huang, P. Silberzan, J.O. Tegenfeldt, E.C. Cox, J.C.Sturm, R.H. Austin, and H. Craighead, *Phys. Rev. Lett.*, **89** (2002) 178301.

[30] L.R. Huang, E.C. Cox, R.H. Austin, and J.C. Sturm, *Science*, **304** (2004) 987-990.

[31] D.W. Inglis, J.A. Davis, R.H. Austin, and J.C. Sturm, *Lab on a Chip*, **6** (2006) 655-658.

[32] M. Yamada and M. Seki, *Lab on a Chip*, **5** (2005) 1233-1239.

[33] J. Takagi, M. Yamada, M. Yasuda, and M. Seki, *Lab on a Chip*, **5** (2005) 778-784.

[34] J. Janca, *Mikrochim. Acta*, **111** (1993) 135-162.

[35] P. Reschiglian, A. Zattoni, B. Roda, E. Michelini, and A. Roda, *Trends Biotechnol.*, **23(9)** (2005) 475-483.

[36] J.C. Giddings, *Science*, **260** (1993) 1456-1465 .

[37] B.N. Barman, E.R. Ashwood, and J.C. Giddings, *Anal. Biochem.*, **212** (1993) 35-42.

[38] Q. Du and M.E. Schimpf, *Anal. Chem.*, **74** (2002) 2478-2485.

[39] C.B. Fuh, *Anal. Chem.*, **April 1** (2000) 266A-271A.

[40] C.B. Fuh, S. Levin, and J.C. Giddings, *Anal. Biochem.*, **208** (1993) 80-87.

[41] M.H. Moon, S.G. Yang, J.Y. Lee, and S. Lee, *Analytical and Bioanalytical Chemistry*, **381** (2005) 1299-1344.

[42] Ö. Gustafsson, A. Düker, J. Larsson, P. Andersson, and J. Ingri, *Limnology and Oceanography*, **45(8)** (2000) 1731-1742.

[43] N. Narayanan, A. Saldanha, and B.K. Gale, *Lab on a Chip*, **6** (2006) 105-114.

[44] E.B. Cummings, *IEEE Engineering in Medicine and Biolology Magazine*, November/December (2003) 75-84 .

[45] N.G. Green, and H. Morgan, *J. Phys. D: Appl. Phys.*, **30** (1997) L41-L84.

[46] H. Watanarai, H. Monjushiro, S. Tsukahara, M. Suwa, and Y, Iiguni, *Anal. Sci.*, **20** (2004) 423-434.

[47] Y. Li, and K.V.I.S. Kaler, *Anal. Chim. Acta*, **507** (2004) 151-161.

[48] S. Choi, and J.K. Park, *Lab on a Chip*, **5** (2005) 1161-1167.

[49] S. Fiedler, S.G. Shirley, T. Schnelle, and G. Fuhr, *Anal. Chem.*, **70** (1998) 1909-1915.

[50] S. Kapishnikov, V. Kantsler, and V. Steinberg, *J. Stat. Mech.*, (2006) P01012 .

[51] A. Nilsson, F. Petersson, H. Jönsson, and T. Laurell, *Lab on a Chip*, 4 (2004) 131-135.

[52] F. Petersson, A. Nilsson, C. Holm, H. Jönsson, and T. Laurel, *Lab on a Chip*, 5 (2005) 20-22.

[53] T. Laurell, F. Petersson, and A. Nilsson, *Chem. Soc. Rev.*, **36** (2007) 492-506.

[54] A. Ashkin, *PNAS*, **94** (1997) 4853-4860.

[55] D.G. Grier, and Y. Roichman, *Appl. Opt.*, **45(5)** (2006) 880-887.

[56] M.P. Macdonald, S. Neale, L. Paterson, A.Richies, K. Dholakia, and G.C. Spalding, *Journal of Biological Regulators and Homeostatic Agents*, **18(2)** (2004) 200-205.

[57] K. Ladavac, K. Kasza, and D.G. Grier, *Phys. Rev. E*, **70** (2004) 010901(R).

[58] D.G. Grier, *Nature*, **424** (2003) 810-816.

[59] A. Rosenthal, and J. Voldman, *Biophys. J.*, **88** (2005) 2193-2205.

[60] A. Rosenthal, B.M. Taff, and J. Voldman, *Lab on a Chip*, **6** (2006) 508-515

[61] Th. Schmelle, T. Müller, and G. Fuhr, *J. Electrostat.*, **50** (2000) 17-29.

[62] M. Ferrari, R. Bashir, and S. Wereley, BioMEMS and Biomedical Nanotechnology. Volume IV: Biomolecular sensing, Processing and Analysis. *Spring US* 2006, Chapter 8.

[63] R.M. Johann, *Analytical and Bioanalytical Chemistry*, **385** (2006) 408-412.

[64] P.Y. Chiou, W. Wong, J.C. Liao, and M.C. Wu, *Proc. 17th IEEE/MEMS International Conference on Micro Electro Mechanical Systems*, Maastricht, 2004, 21-24.

[65] P.Y. Chiou, A.T. Ohta, and M.C. Wu. *Nature*, **436** (2005) 370-372.

[66] V. Ramachandran and H.S. Fogler, *J. Fluid Mech.*, **385** (1999) 129-156.

[67] V. Ramachandran, R. Venkatesan, G. Tryggvason, and H.S. Fogler, *J. Colloid Interface Sci.*, **229** (2000) 311-322.

[68] D.L. Feke, N.D. Prabhu, J.A. Mann Jr., and J.A. Mann, III, *J. Phys. Chem.*, **88** (1984) 5735-5739.

[69] G. Brans, R.G.M. van der Sman, C.G.P.H. Schroën, A. van der Padt, and R.M. Boom, *J. Membr. Sci.*, **278** (2006) 239-250.

[70] J. Kromkamp, D. van den Ende, D. Kandhai, R.G.M. van der Sman, and R.M. Boom, *Chem. Eng. Sci.*, **61** (2006) 858-873.

[71] M.T. Valentine, L.E. Dewalt, and H.D. Ou-Yang, *J. Phys.: Condens. Matter*, **8** (1996) 9477-9482.

[72] W. Choi, S.H. Kim, J. Jang, and J.K. Park, *Microfluid Nanofluid*, **3** (2007) 217-225.

Chapter 3

Refinement of classification rules for deterministic ratchets through 2-D flow field simulation

Abstract

Nowadays microfluidic devices are becoming popular for cell/DNA sorting and fractionation. One class of these devices, namely deterministic ratchets, seems most promising for continuous fractionation applications of suspensions [1]. In this paper, we present a refinement of the existing classification rules, obtained via the numerical simulation of fluid flow through the periodic array of the deterministic ratchet. Contrary to the hypotheses of the inventors [2, 3], we have found that the distribution of the flow lanes is *asymmetric* for a large portion of the design parameter space. This implies that their classification rules have to be refined. Hence, we have performed an exhaustive parameter study via numerical analysis of the flow field in deterministic ratchets. From our results we have formulated new classification rules, and have used them to optimize the design of compact ratchets for optimal yield, which is desirable for fractionation of suspensions.

3.1 Introduction

A deterministic ratchet, also known as a deterministic lateral displacement (DLD) array, is a microfluidic device used for sorting and fractionation of cells and DNA

in biological applications [2–5]. Fractionation is defined as the removal of a class of particles from a complex suspensions. The fractionation in deterministic ratchet is based on the flow line sieving principle [6]. Other examples of flow line sieving devices are found in the works of Yamada and co-workers [7, 8], and in blood plasma separation devices using the plasma skimming principle [9–12].

In flow line sieving devices, the flow field in the microchannel is divided into so-called flow lanes, which are bordered by dividing stream lines. These dividing stream lines originate and terminate in stagnation points in the flow field, induced by obstacles placed in the microchannel, or via (multiple) inlets and outlets of the microchannel. Via steric interaction with the obstacles or confining walls of the microchannel, large particles will cross these dividing streamlines, and are displaced to the adjacent flow lanes. Particles smaller than the width of the flow lane will just follow the stream lines. Due to the different behaviour of small and large particles one can fractionate them, if the flow line sieving devices have different outlets downstream [6].

Flow line sieving in deterministic ratchets is accomplished by a two-dimensional array of obstacles [2, 3], as shown in figure 3.1A - where the obstacles have cylindrical shape. The division of the flow field in flow lanes is shown in figure 3.1B, with the dividing stream lines depicted as solid lines, originating from the back of the obstacle, and terminating at the front of the obstacle, positioned exactly downstream. The essential property of the deterministic ratchet is that each next row of obstacles is displaced a small distance with respect to the previous row in the direction perpendicular to the flow direction. The symmetry breaking of the obstacle placement leads to continuous displacement of large particles in one particular direction, while small particles will follow the flow lanes and zigzag around the obstacles - having on average zero displacement in the perpendicular direction. Displacement and zigzag movement of particles are shown in figure 3.2.

Based on the assumptions of 1) Poiseuille flow profile in between obstacles within one row, and 2) equal volumetric flow rate of each flow lane, Inglis and co-workers have determined a classification rule, stating whether a particle with a certain size will display displacement movement or zigzag movement [3]. The classification is based on the ratio of particle radius and the first flow lane width. The classification rule seems to hold well for the set of devices tested in their work [3].

However, this classification rule seems not to be valid for certain types of devices, as apparent from the remark on mixed behaviour in a figure in work of Heller and Bruus

[13]. Surprisingly, this finding is only briefly discussed in the caption of this paper [13]. Knowledge of the working of ratchets in the complete design parameter space is required for their optimal design. Hence, there is an obvious need for refinement of the classification rules for deterministic ratchets.

In a previous review paper [1], we have shown that deterministic ratchets are promising for fractionation of concentrated, polydisperse suspensions. Earlier work on fractionation of food suspensions with membranes shows that this classical method is much hindered by the larger particles plugging the pores of the membrane [14, 15]. The chance of particles plugging the space between obstacles (i.e. the pore) is much smaller in deterministic ratchets. This is due to the fact that 1) the pore size is always larger than all to be fractionated particles (a requirement of the flow line sieving principle), and 2) the slit-like shape of the pore between obstacles, having a height much larger than the width (being the distance between obstacles).

Based on the quite limited chance of particle accumulation, we have estimated the productivity or yield of several designs of deterministic ratchets, as in food applications a high yield per unit of occupied space is desired [1]. We have shown that higher yields are attainable with devices, that are more compact. Inglis and coworkers have not considered the variation of interspacing between rows. Hence, it might be that there are more compact devices with higher yield than those investigated by Inglis and co-workers [3]. We expect that if the distance between adjacent rows becomes comparable with the interspacing between obstacles, the flow profile within one pore will be influenced by the vicinity of neighbouring rows.

The classification rule of Inglis and coworkers does not seem to hold in general. Further there is a need for compact deterministic ratchet for food applications, and for this, refinement of classification rules is required. Consequently, we have engaged in numerical simulations of the flow field in compact deterministic ratchets in order to obtain the refined classification rules.

As shown by other papers on the design of deterministic ratchet/flow line sieving devices [10, 17, 18], 2-D flow field simulation is sufficient to obtain design rules. From the 2D simulations, one can obtain the flow lane distribution, or equivalently the dividing streamlines. Knowing the flow lane distribution, one can determine the maximal size of particles which will follow the streamlines, and thus will show zigzag motion, and subsequently the classification rule can be deduced.

In this paper we report the results of the numerical analysis in terms of the dis-

tribution of flow lanes, from which we have deduced the refined classification rules. Via these new classification rules, we have formulated design rules for deterministic ratchets having an optimal yield, based on the assumption of bidisperse feed having spherical particles .

The numerical analysis is performed with the method of Lattice Boltzmann [19], via which we have determined the 2-D flow field. 2-D calculations can be employed for deterministic ratchets due to the high aspect ratios of the obstacles, which can be in the order of 1:10, as is the case in previously investigated devices discussed by Huang et al.[2], and Inglis et al.[3].

Our paper is organized as follows. First, we discuss the design principles of the deterministic ratchet in more detail. Secondly, we discuss the numerical method and the setup of our numerical analysis - including the method to calculate the flow lane distribution and the yield of the device. The presented numerical results include 1) the validation of the Lattice Boltzmann code, 2) the presentation of flow lane distribution and related classification rules, and 3) the values of the yield and the design rules deduced thereof. The paper is ended with a summary of our main conclusions.

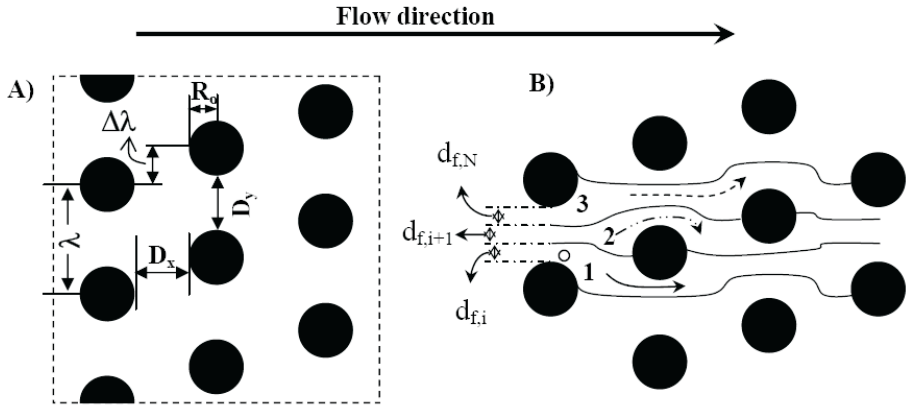

Figure 3.1: A) Characteristic length scales of a deterministic ratchet indicated in a periodic cell, with $N = \lambda/\Delta\lambda = 3$. B) The gap between obstacles is divided into a number of flow lanes, which is equal to $N = \lambda/\Delta\lambda = 3$.

3.2 Principle of deterministic ratchet

As mentioned above, the deterministic ratchet employs the flow line sieving principle via placing periodic arrays of obstacles in a microchannel. This periodic array

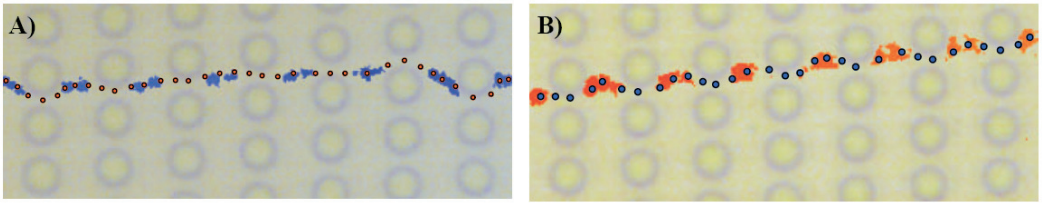

Figure 3.2: View through a microscope of a periodic cell of one of our realizations of a deterministic ratchet, showing A) zigzag motion of small particles ($r_{p1} < d_{f,c}$), and B) displacement motion of large particles ($r_{p2} > d_{f,c}$). The design of the ratchet device is based on the simulation result of $N = 6, D_x/D_y = 2$ and $R_o/D_y = 0.6$ with $D_y = 7.3$ μm, giving a critical lane width of $d_{f,c} = 2.15$ μm. Height of the pillar is 30 μm, the nominal radius of small particles is $r_{p1} = 1.15$ μm, and the nominal radius of the large particle is $r_{p2} = 2.5$ μm.

is characterized by a number of geometric parameters, as indicated in figure 3.1A. In this figure we have displayed a periodic unit cell of the obstacle array, using cylindrical pillars as obstacles. In practice a deterministic ratchet array consists of a multitude of periodic cells.

The characteristic length scales of such a periodic cell are:

- R_o is the radius of the obstacle.
- D_x is the gap width between obstacles in the flow direction.
- D_y is the gap width perpendicular to the flow.
- $\Delta\lambda$ is the shift in position of adjacent rows of objects perpendicular to the flow direction.

The shift $\Delta\lambda$ is a fraction of the distance between the centers of the obstacles, denoted as $\lambda = D_y + 2R_o$. The ratio $N = \lambda/\Delta\lambda$ is originally taken as an integer number [2, 3]. A very recent paper [20] discusses a deterministic ratchet with non-integer values of $\lambda/\Delta\lambda$, but this class of ratchets we will not consider here. This shift of adjacent rows of obstacles is the main feature of deterministic ratchets, and is, as said, essential for the fractionation principle.

Another degree of freedom in the design of a deterministic ratchet is the (tilt) angle between the flow direction, and the principle axis of the periodic cell. For computational efficiency we have chosen this tilt angle to be zero. We should notice that this tilt angle is non-zero, and is even the main design parameter in the works of

the inventors of the DLD [2, 3]. Their designs are further restricted to $D_x = D_y$, and the various values of N are realized through variation of the tilt angle.

In figure 3.1B, we have sketched the flow lane distribution for a deterministic ratchet with $N = 3$. The number of flow lanes in the gaps between the obstacles is always equal to N. The solid lines represent the dividing streamlines, which start at the back of the obstacle and end at the front of an obstacle, exactly N rows downstream. The dividing streamline will pass below or above the obstacles positioned in between its starting and ending point.

Hence, small particles (smaller than the flow lane widths) will follow streamlines and thus stay in their flow lane. Consequently, they will move through the obstacle array in a zigzag motion, as indicated in flow lanes 1 to 3 in figure 3.1B. Hence, on average small particles will have a zero displacement in the direction perpendicular to the flow.

In the hypothesis of Inglis and co-workers, their assumed flow lane distribution is non-uniform, but symmetric [3]. An important characteristic of the flow lane distribution is the first flow lane width $d_{f,1}$. According to Inglis, a particle having a radius larger than this first lane width, $r_p > d_{f,1}$, will continuously bump onto an obstacle every time it passes an obstacle row. Due to the shift in the position of adjacent rows (with $\Delta\lambda$) the larger particles will be displaced in the direction perpendicular to the flow with every pass through an obstacle row. The zigzag motion of small particles ($r_p < d_{f,1}$) and the displacement motion of large particles ($r_p > d_{f,1}$) are shown in figure 3.2, where we display one of our realizations of a deterministic ratchet, with $N = 6$. The particle trajectory is obtained here via image analysis.

A sketch of a minimal deterministic ratchet device by which one can fractionate a bidisperse suspension is shown in figure 3.3. The device has two inlets having the same width as one periodic cell l_y. Through one of the inlet flows the bidisperse suspension enters, while through the other inlet a carrier fluid is flowing at the same flow rate as the fluid with suspended particles. The device must have at least $2 \times N$ periodic cells, as it takes a large particle N periodic cells to traverse the width l_y of a periodic cell. If a large particle has traversed this distance, it will end up in the upper outlet, while the smaller particles will move via their zigzag motion with net zero displacement towards the lower outlet.

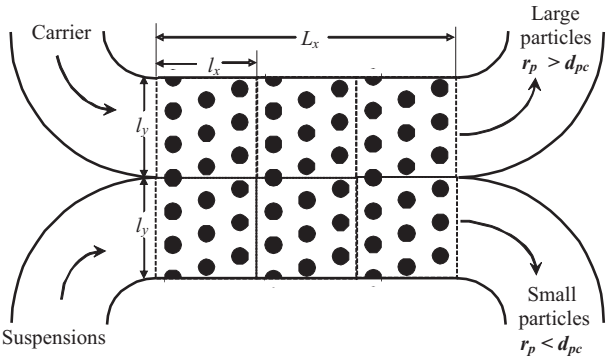

Figure 3.3: Sketch of the possible minimal size of single device with $N = 3$.

3.3 Numerical analysis

3.3.1 Lattice Boltzmann method

For the numerical analysis of the flow we use the Lattice Boltzmann (LB) method [19]. The Lattice Boltzmann method is chosen because of its efficient and simple way of handing complex geometries, like the deterministic ratchet [21]. Furthermore, the method can easily be extended with explicit particles suspended in the fluid using the method developed by Ladd [22]. For the simulation of the flow field presented in this paper we have applied the commonly used Lattice BGK scheme [23], having 9 velocities on a two-dimensional lattice (D2Q9).

Simulations are performed for a single periodic cell of the deterministic ratchet, such as depicted in figure 3.1. A 2-D approximation is valid, if the height of the cylindrical pillars is much larger than their radius ($h \gg R_o$), as is the case in our experimental realizations of the deterministic ratchet (figure 3.2) and in the work of Inglis and co-workers [3]. The no-slip boundary condition at the interface of fluid and obstacles is implemented using the bounce back method, as discussed in a review of Ladd and Verberg [21]. The pressure drop over the periodic cell is implemented using the 'pressure periodic' boundary conditions as proposed by Inamuro and co-workers [24].

Numerical variables are in units of lattice spacing (Δx) and time step (Δt). Sufficient spatial resolution of the flow lane distribution simulations is obtained for $D_y \geq 27\Delta x$, $R_o \geq 18\Delta x$ and $\Delta\lambda \gg \Delta x$. A computational domain with minimal resolution is displayed in figure 3.4. Simulations are performed with the flow always in the Stokes flow regime, as expressed by the obstacle Reynolds number $Re = \bar{u}R_o/\nu < 0.1$, with $\bar{u}$

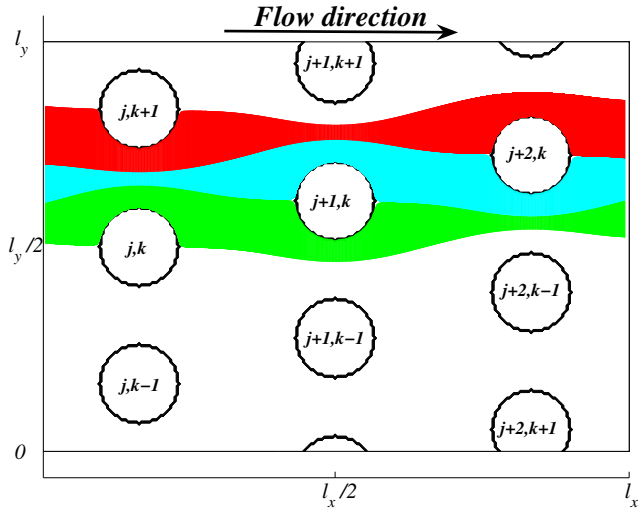

Figure 3.4: Simulation of flow field on a lattice with minimal resolution. The periodic cell is characterized with $N = 3, D_x/D_y = 2$ where $l_y = N(2R_o + D_y)$ and $l_x = N(2R_o + D_x)$. The flow lanes are indicated with different colors, and are computed using the procedure described in section 'Determination of flow lanes'.

the average fluid velocity in the ratchet device, and ν the kinematic viscosity of fluid. Furthermore, to reduce compressibility errors the Mach number $Ma = \bar{u}/c_s \ll 1$, with c_s the so-called speed of sound, which is a numerical attribute of the LB method. Lattice Boltzmann operates in the weakly compressible flow limit for the simulation of incompressible flow, which means that fluid velocities must be much smaller than this speed of sound [25].

3.3.2 Simulation setup

Before we analysed the flow lane distribution in various ratchet designs, we have validated our Lattice Boltzmann code against a benchmark problem of Sangani and Acrivos [26], who have investigated the drag force on cylinders induced by pressure driven flow through a periodic, square or hexagonal array of cylindrical objects with axis perpendicular to the flow direction. We have also compared the correlation of Sangani and Acrivos [26] with the drag force experienced by cylindrical obstacles in a periodic array of the deterministic ratchets.

After having validated our simulation code, we have performed simulations to acquire the complete flow field in a single periodic cell of various ratchet designs. Ratchet

designs are characterized by the following dimensionless geometric parameters:

1. N
2. D_x/D_y
3. R_o/D_y

We have performed a thorough analysis of this parameter space. In first instance, we have done simulations on ratchets having cylindrical obstacles, but we will analyze briefly the effects of other obstacles, having a cross section shaped as an ellipse, square, diamond, or rectangle.

We have traversed through the design parameter space via examination of three different cross sections:

i) $N \times D_x/D_y$; with fixed R_o/D_y.

ii) $R_o/D_y \times D_x/D_y$; with fixed N.

iii) $N \times R_o/D_y$; with 4 values of D_x/D_y.

For each simulation we have determined the flow lane distribution $\{d_{f,i}\}$ following the method explained in the next section. With the knowledge of the lane width distribution, we can formulate the refined classification rules.

Determination of flow lanes

From the LB simulations we obtain the steady state velocity field $\mathbf{u}(\mathbf{x})$ throughout the periodic cell of the ratchet device. We have determined the sizes of the flow lanes via particle tracking analysis of the Lattice Boltzmann simulations.

In particle tracking analysis one determines the trajectories of small particles $r_p \ll \{d_{f,i}\}$, which follow the fluid streamlines; Brownian motion is assumed negligible ($r_p > 0.1$ μm). Via solving $dx/dt = \mathbf{u}(\mathbf{x})$, particle tracking is performed by using simple Euler forward integration (Eq. 3.1) where $\Delta t < 0.1\Delta x/\bar{u}$.

$$\mathbf{x}(\mathbf{t} + \mathbf{\Delta t}) = \mathbf{x}(\mathbf{t}) + \mathbf{u}(\mathbf{x})\mathbf{\Delta t} \tag{3.1}$$

If the position $\mathbf{x}$ falls in between lattice points, the velocity $\mathbf{u}(\mathbf{x})$ is determined by linear interpolation using the velocities at the 4 nearest neighboring lattice points.

The accuracy of the Euler method is checked via comparing results with those of a 4^{th} order Runge-Kutta method, for a select number of cases. Comparison is performed between solutions, which have converged within 1% accuracy between consecutive reduction of the time step Δt. Solution of the Euler methods and the Runga-Kutta method agree with each other within 5%. Because the computational effort is smaller for the Euler method, we have chosen for that method.

We compute the width of flow lanes $d_{f,i}$ by releasing a small (tracer) particle in the gap between obstacles (j, k) and $(j, k + 1)$. Particle release takes place at 100 positions per unit lattice spacing Δx equidistantly distributed locations along the direction perpendicular to the flow. The movement of the tracer particles is computed by equation 3.1. For each tracer particle, we determine whether it moves above or beneath certain obstacles.

Each obstacle in the periodic cell is identified with a row number j, and a line number k, as shown in figure 3.4. Note that the centers of the obstacles with the same line number k at row number $j+1$ are shifted from the row j at the shift, $\Delta\lambda = \lambda/N$.

A tracer particle (with $r_p \ll d_{f,i}$) performing zigzag motion, and released in the pore space between obstacles j, k and $j, k + 1$, will cross somewhere this straight line defined by line number k. The particle in the first lane will cross the line between obstacles j, k and $j + 1, k$, and the particle in flow lane with index i will cross the line between obstacles $j + i - 1, k$ and $j + i, k$, as can be observed from figure 3.4.

Hence, via this procedure we determine the identifier of the flow lane of particles released at different positions in the pore space between obstacles. From these data and the release positions of the particles we are able to construct the flow lane distribution from the LB simulations of the flow field.

The obtained flow lane distribution is compared with the distribution according to the hypothesis of Inglis and co-workers [3], who assumed a parabolic flow profile and that all N flow lanes have equal volumetric flow rate. The critical lane width $d_{f,1}$ according to Inglis is derived via the following relation [3]:

$$\int_0^{d_{f,1}} u_x(y)dy = \int_0^{D_y} \frac{u_x(y)}{N} dy \tag{3.2}$$

Using $u_x(y)$ for Poiseuille flow, the solution can be written as follows [3]:

$$\left[\frac{d_{f,1}}{D_y}\right]^3 - \frac{3}{2}\left[\frac{d_{f,1}}{D_y}\right]^2 + \frac{1}{2N} = 0 \tag{3.3}$$

3.4 Model validation and pressure drop

We have validated the simulation code by comparison of the drag force F_{Sa} on the cylinder obstacle in a periodic array with the work of Sangani and Acrivos [26]. They have investigated the drag force as a function of the area fraction, in simple square and hexagonal arrays of circular cylindrical obstacles. We note that the square and hexagonal arrays are special cases of the periodic arrays considered in deterministic ratchet designs. The simple square array is obtained by setting parameters $N = 1$ and $D_x = D_y$, while the hexagonal array is obtained by setting $N = 2$ and $(D_x + 2R_o) = \sqrt{3}(D_y + 2R_o)$. As these designs do *not* break symmetry, one can not fractionate particles with it. It is of further interest to compare the correlation of Sangani and Acrivos [26] also with the drag force computed for a real ratcheting device with $N = 3$. Simulations are performed with $R_o \geq 6$, $U\Delta t/\Delta t \ll 1$, and $Re = UR_o/\mu \ll 1$.

Sangani and Acrivos [26] give a correlation for the drag force, which holds for area fraction $C < 0.25$:

$$F_{Sa} = \frac{F_{drag}}{\mu U h} = \frac{4\pi}{\ln(C^{-1/2}) - 0.738 + C - 0.887C^2 + 2.038C^3 + O(C^4)} \tag{3.4}$$

μ is the fluids dynamic viscosity, U is the mean velocity, and h is the height of the cylinders. The area fraction in terms of ratchet design parameters is: $(C = N^2\pi R_o^2/(l_x l_y))$. In the simulations we have computed the drag force on the obstacle from the pressure drop over the periodic cell of the array, having a cross section $A = hl_y$ and N the number of obstacle rows in a periodic cell. Hence,

$$pA = F_{drag}N^2 \tag{3.5}$$

The simulation results are shown in figure 3.5. There, we also show the results for the ratchet with $N = 3$ and $D_x = D_y$, and compare that with the correlations from Sangani and Acrivos [26]. As one can observe, our Lattice Boltzmann scheme can very accurately reproduce the results of Sangani and Acrivos [26]. For $C > 0.25$ we have used the tabulated data from Sangani and Acrivos [26].

The ratchet design with $N = 3$ follows the correlation for the square array upto $C = 0.5$. Brief investigations of other ratchets designs with $D_x/D_y \geq 1$, $N = 4$ and $C < 0.25$ indicate little deviations from the result with $N = 3$ and $D_x = D_y$.

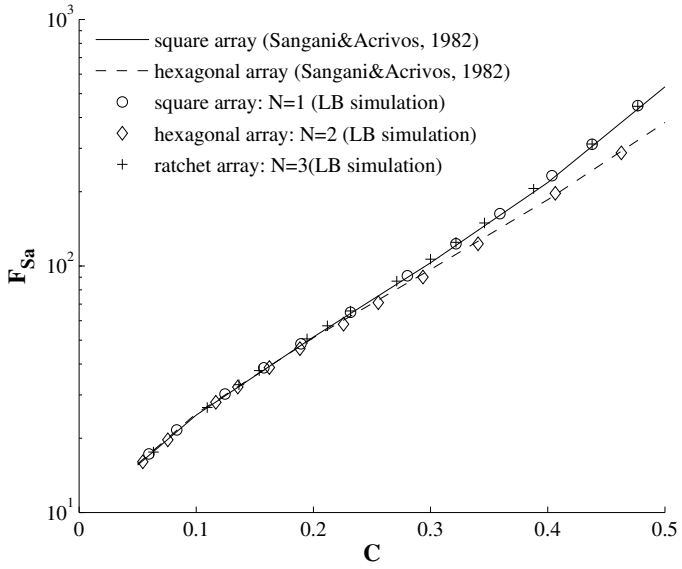

Figure 3.5: Comparison of the dimensionless drag force (F_{Sa}) as a function of the area fraction (C) of obstacles from the numerical results of Sangani and Acrivos [26] with Lattice Boltzmann (LB) simulation of square array (N=1), hexagonal array (N=2), and ratchet array (N=3).

Because the square and hexagonal arrays also do not show much difference, we expect all ratchet designs to give the same result in the range $C < 0.25$. In practice, the area fraction of ratchet arrays will not be above this limit, and hence the correlation of Sangani and Acrivos [26] will render a good estimate of the pressure drop over the ratchet device.

3.5 Refinement of classification rules

As stated above, we investigate the flow lane distribution for different cross sections of the design parameter space. In the first series of simulations, we have examined the cross section $N \times D_x/D_y$ of the design parameter space, with $2 \leq N \leq 10$ and $0.5 \leq D_x/D_y \leq 10$. We have fixed the ratio of obstacle radius to pore size (R_o/D_y) to 0.6. In figure 3.6, we show the flow lane width distributions for $N = 6$. Here, we immediately observe that for $D_x/D_y \leq 2$ the flow lane distributions are asymmetric, and this is not in line with the hypothesis of Inglis and co-workers [3], who assumed a parabolic flow profile in between the obstacles, and thus a symmetric flow lane distribution. For all D_x/D_y the flow lane distribution is non-uniform, with the first

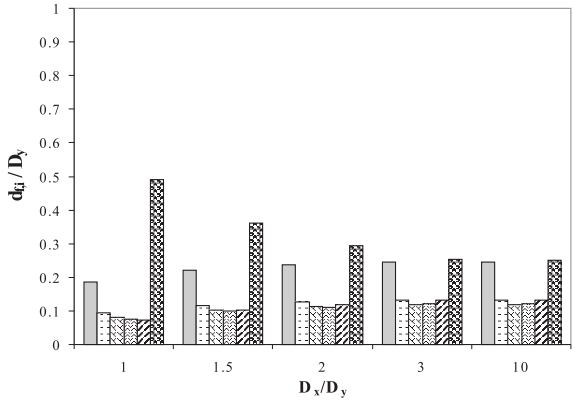

Figure 3.6: The lane width distributions of devices with $N = 6$, $R_o/D_y = 0.6$, for various values of D_x/D_y.

and last lanes larger than the middle lanes.

The inventors [2, 3] state that the width of the first flow lane $d_{f,1}$ determines the radius of those particles r_p which will move in zigzag motion. Due to asymmetric distribution of flow lane widths as shown in figure 3.6, we can imagine that only particles, $r_p > d_{f,N}$, will have continuous steric interaction with each obstacle row and show displacement motion. For the particle in between these flow lane widths, $d_{f,1} < r_p < d_{f,N}$, we expect steric interaction with a selected number of obstacle rows, and the particle may move in an intermediate manner in between zigzag and displacement motion. This type of 'mixed motion' is briefly mentioned in a caption of a figure in the paper of Heller and Bruus [13]. Hence, we expect both length scales $d_{f,1}$ and $d_{f,N}$ to be important for the classification of the type of particle motion in DLD devices.

The simulation results obtained for different D_x/D_y are summarized in figure 3.7A and B. It is obvious that $d_{f,1}/D_y$ and $d_{f,N}/D_y$ strongly depend on N and D_x/D_y. We note that periodic arrays with $N = 2$ are *not* symmetry breaking, and consequently the width of the two flow lanes are always equal, i.e. $d_{f,i}/D_y = 0.5$.

For $D_x/D_y \leq 1$, we find that $d_{f,1}/D_y$ is significantly lower than the theoretical prediction of Inglis, while $d_{f,N}/D_y \geq 0.5$. In these devices, displacement motion of particles is presumably not possible, as particles with radius larger than $d_{f,N}$ do not fit in the pore space, as $r_p > d_{f,N} > 0.5D_y$. We will denote devices with $d_{f,N} > 0.5D_y$ as *non-fractionating* devices.

For $D_x/D_y \geq 3$, the graphs of both 3.7A and B, coincide with the line according to

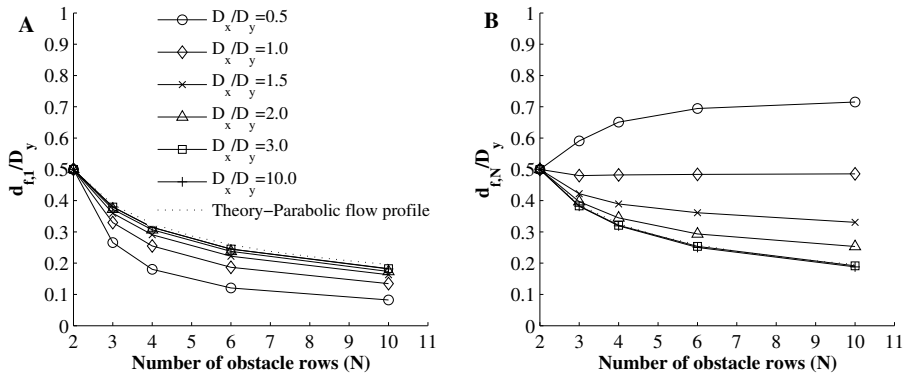

Figure 3.7: A) the ratio $d_{f,1}/D_y$ and B) the ratio $d_{f,N}/D_y$ as a function of N and D_x/D_y with fixed $R_o/D_y = 0.6$ compared to the theoretical parabolic flow profile computed by equation 3.3.

the hypothesis of Inglis, i.e. Eq.(3.3). Hence, the hypothesis of a symmetric flow lane distribution holds for a selected number of ratchets from the first series of designs, namely those having a large spacing between the rows of obstacles: $D_x/D_y > 3$. If the obstacle rows are more closely packed the adjacent rows will influence the flow distribution in between the obstacles, leading to the asymmetric flow lane distribution shown in figure 3.6.

From the perspective of the application of concentrated food suspension fractionation, we seek compact devices with high yields. Hence, the regime of $D_x \approx D_y$ is important, where the flow lane distribution is asymmetric and the ratchet design may be limited by the *non-fractionation* constraint. Hence, from this perspective the largest lane width $d_{f,N}$ appears to be more important than $d_{f,1}$ to compare different ratchet designs. Hence, in the remainder of this paper our results will be presented only in terms of the largest flow lane width $d_{f,N}$.

In the second series of simulations we have investigated the effect of R_o/D_y for various D_x/D_y ($1.0 \leq D_x/D_y \leq 3$ and $0.2 \leq R_o/D_y \leq 2$). We have fixed the number of rows in a periodic cell to $N = 6$. Results are shown in figure 3.8.

For all D_x/D_y, we observe that $d_{f,N}/D_y$ increases with increasing R_o/D_y, except in the case of $D_x/D_y = 3$ where the critical lane width approaches the values predicted by Eq.(3.3), which are indicated with the dash lines in figure 3.8. Some values of the critical lane width seem to fall below these '*limiting*' values. We have encountered such situations also in the third series of simulations, and below we will discuss this phenomenon in more detail.

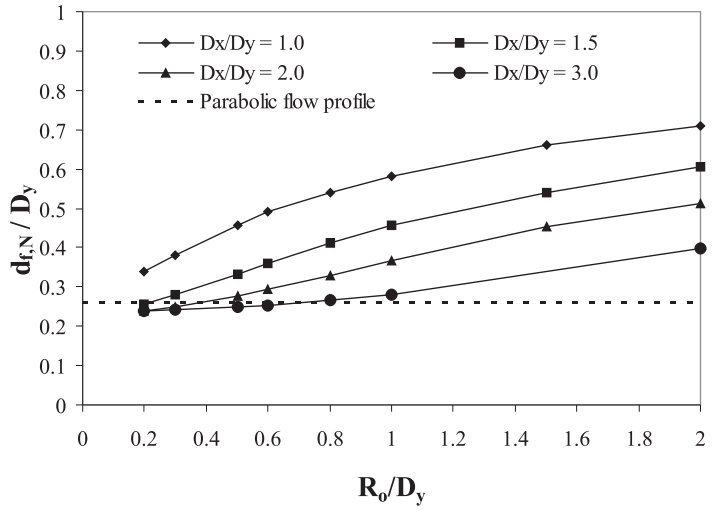

Figure 3.8: The ratio of largest lane width and obstacle spacing $d_{f,N}/D_y$ for ratchets with $N = 6$, as function of R_o/D_y for various values of D_x/D_y. The dash line is the limiting value computed with Eq.(3.3).

In the third series of simulations we vary the ratio of obstacle radius over the pore width in the range $0.2 \leq R_o/D_y \leq 2$, and the number of obstacles in a row within the range $3 \leq N \leq 10$. We have taken four fixed values of $D_x/D_y = \{1.0, 1.5, 2.0, 3.0\}$. Results are shown in figure 3.9.

Again we observe an increase in $d_{f,N}/D_y$ with increasing R_o/D_y. Remarkably, for constant value of D_x/D_y the graphs for various N cross at the same interaction point at $d_{f,N}/D_y \approx 0.5$. The location of the intersection point clearly depends on D_x/D_y. From the collection of these intersection points, we can deduce a simple rule for the constraint of '*the ability to fractionate*'. This rule is: $R_o < D_x - 0.4D_y$, since $d_{f,N}/D_y < 0.5$. Although this is a simple criterion, we do not have a good explanation for the existence of the intersection point.

For $D_x/D_y = 3$ and $R_o/D_y \leq 1$, the critical lane width, $d_{f,N}/D_y$, does not change appreciatively. However, for low values of R_o/D_y the critical lane width seems to fall below the 'limiting' value, as calculated from the hypothesis of Inglis, i.e. Eq.(3.3). To investigate the cause of this phenomenon further, we have analyzed the flow field between obstacles in a ratchet with $D_x/D_y = 1$, $N = 1$, and various values of R_o/D_y, which is shown in figure 3.10. We observe that for $R_o/D_y \leq 0.2$, the flow profile deviates from the parabolic flow profile, which is assumed by Inglis. For smaller values of R_o/D_y the flow profile becomes more blunted. In ratchet designs with $N \geq 3$

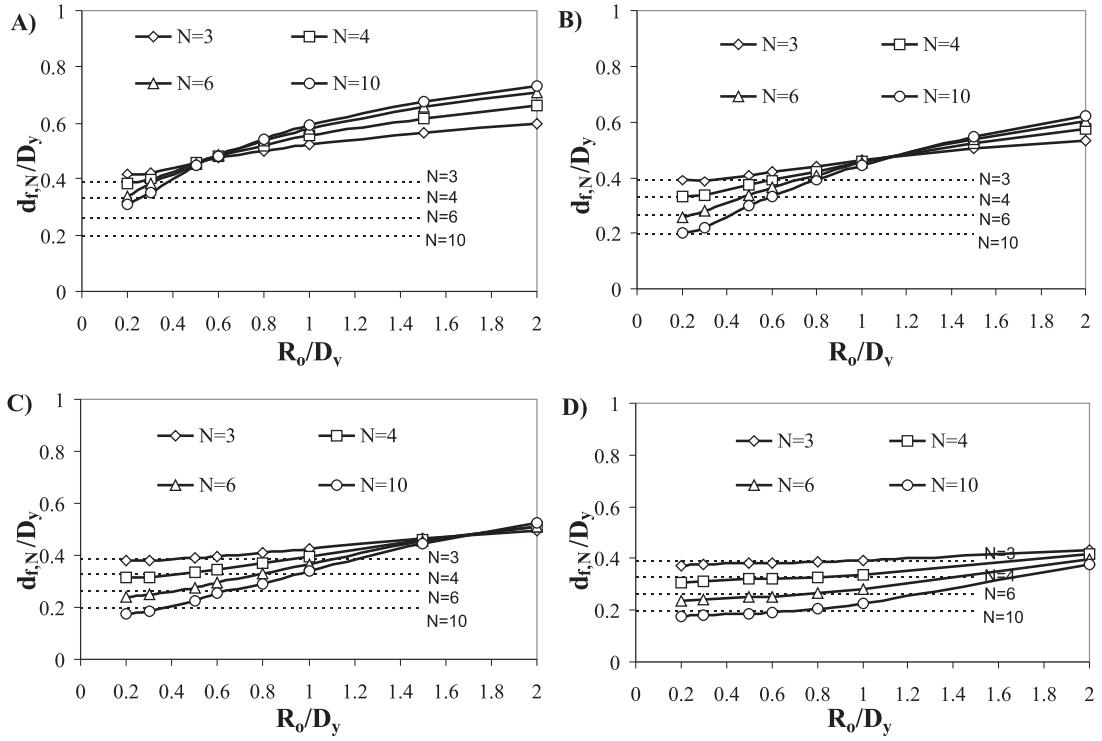

Figure 3.9: Ratio of $d_{f,N}/D_y$ as a function of R_o/D_y and N of A) $D_x/D_y = 1.0$, B) $D_x/D_y = 1.5$, C) $D_x/D_y = 2.0$ and D) $D_x/D_y = 3.0$ compared to the limiting values (dash line) determined from equation 3.3.

we also observe a blunting of the flow profile, leading to a flow lane distribution which is symmetric, but more uniform than computed using the hypothesis of Inglis. Consequently, $d_{f,N}/D_y$ may drop below the value predicted by Eq.(3.3), as shown in figures 3.8 and 3.9. The deviation from the hypothesis of parabolic flow profile becomes significant in the ranges for $R_o/D_y \leq 0.2$ and $D_x/D_y \geq 2$. We anticipate that in the limit of $R_o/D_y \to 0$ the flow profile will approach a uniform flow profile, as postulated in the original hypothesis of the inventors [2].

In the final series of simulations, we have investigated the effect of obstacle shapes. Simulations are performed for $N = 3$, $D_x/D_y = 2$ and $R_o/D_y = 0.67$. The tested shapes are shown in figure 3.11, together with the results on the critical lane width.

We observe that the $d_{f,N}/D_y$ values are quite similar for the different obstacle shapes. Also, the size ratio of the shapes (L_1/L_2) does not have a significant influence on the results. Hence, we conclude that obstacle shape does not matter much, as long as the cross-sectional dimension of the object facing the flow is equal. Note

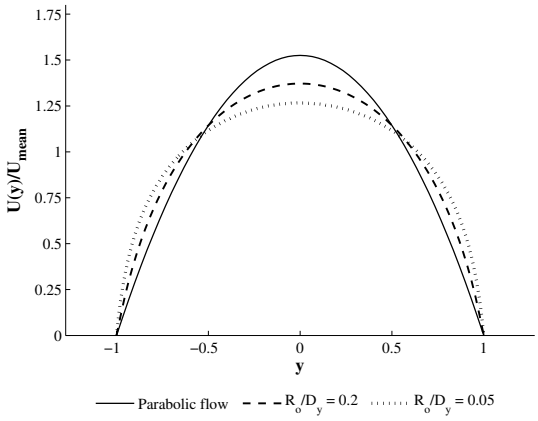

Figure 3.10: The velocity profile from simulation with $N = 1$ and $D_x/D_y = 1$ of $R_o/D_y = 0.05$ and 0.2: the solid line is the normal parabolic flow profile, and $-1 \leq y \leq 1$ is the position of the gap between obstacles where $\mid y \mid = 1$ is the wall of the pore.

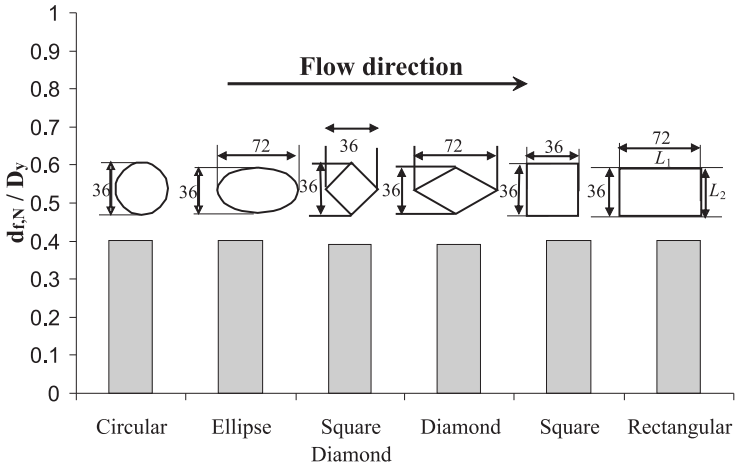

Figure 3.11: Ratio $d_{f,N}/D_y$ for $N = 3$, $D_x/D_y = 2$ and $R_o/D_y = 0.67$ for various obstacle shapes and size ratio (L_1/L_2).

that we observe only obstacle shapes which are mirror-symmetric planes parallel and perpendicular to the flow. Therefore, we expect the design rules derived in the next section for cylindrical objects, are also valid for other shapes.

3.6 Yield analysis

In our previous work [1], we have evaluated the performance of microfluidic devices for continuous suspension fractionation based on their yield, selectivity, and potential for large-scale application in which devices are stacked. In this paper, we follow this evaluation method to quantify the yield of the investigated ratchet designs.

We assume that the ratchet device is fed by a bidisperse suspension with spherical particles, with large particles having radius $r_{p2} \geq d_{f,N}$, and small particles having radius $r_{p1} < d_{f,1}$. The ratchet device has the minimal design as shown in figure 3.3, which was already discussed above. Note that in the real application, the size of the device is larger than the minimal device; for instance in our experimental device, a design of $N = 3$ comprises $L_x \times L_y = 96$ periodic cells in total with $L_x = 8l_y$ and $L_y = N \times L_x/2$. With the larger size of devices and high throughput, we expect that the disturbing effect of side walls on the flow is negligible in the major part of the device.

The volume fractions of the small and large particles are respectively c_1 and c_2. The yield or productivity of a single device is equal to $Y_s = c_2\phi$, which is measured in the total volume of fractionated particles per unit of time. ϕ denotes the volumetric flow rate.

The volume fraction of the large particles, c_2, is constrained by the probability of plugging of pores, P_f, in between the obstacles. Pore plugging is a rather complex process [16], but nevertheless, we have devised a useful estimation based on the work of Ramachandran and Fogler [27]. In this case, we consider the probability of plugging by arrival of multiple particles at the same time [1] which is more relevant and rather different from the work of Wyss and co-workers [16], who focus on plugging of a long pore by adsorption of particles on the wall (which is a single particle mechanism).

This probability P_f of multiple particles simultaneously arriving at the pore and plugging the pore, is [1]:

$$P_f = c_2^{\frac{A_s}{A_{p2}}} \tag{3.6}$$

This assumption is based on monodisperse, spherical particles in which $A_{p2} = \pi r_{p2}^2$ is the cross sectional area of the large particle, and $A_s = hD_y$ is the cross sectional area between two cylindrical pillars with height h and with gap D_y. The ratio A_s/A_{p2} denotes the number of large particles required to completely plug the area between the

pillars. We require that the deterministic ratchet shows at least similar performance as a microsieve membrane with circular holes which was used by Brans and co-workers, with particle suspensions with $C_2 = 0.1\%$ [28]. For this application, $A_s = \pi r_s^2$, and $r_s/r_{p2} = 3 - 5$. For the smallest ratio $r_s/r_{p2} = 3$, P_f is 10^{-27}. If $r_s/r_{p2} \geq 5$ particles will flow through the circular pores without plugging [27, 29].

For all evaluated ratchet devices we assume that they have identical height h, and consequently the probability of plugging is determined only by D_y, which will set the upper limit for $c_2 = 0.2$. Via the differences in the length scales D_x, D_y and R_o the evaluated ratchets will largely differ in the amount of area they will occupy, and consequently in the number of devices that can be placed on a single wafer. For a fair comparison of the productivity we will compare the yield Y_s per unit of volume the device occupies (V_s). If we multiply that with the processing time t_e, we obtain a dimensionless yield:

$$Y^* = \frac{Y_s t_e}{V_s} \tag{3.7}$$

The processing time is taken as a fraction of a single day. In the food processing industry, equipment needs to be cleaned daily, and for deterministic ratchets, this will be no different. We have taken that processing time $t_e = 0.9$ days. The volume occupied by a minimal ratchet device is $V_s = hL_xL_y = 2NV_{cell}$, with $V_{cell} = l_x l_y h$ the volume of a periodic cell.

For the evaluation we take cylindrical obstacles with a radius of $R_o = 0.5$ μm, which is equal to the minimal resolution of the lithography process by which we produced the ratchets shown in figure 3.2. The height of the obstacles is $h = 30$ μm, which is in accordance with the maximal aspect ratio of cylindrical obstacles which can be realized by the lithography. The size of the largest lane width used in the evaluation is based on the typical particle sizes in fractionation of milk: fat globules with a diameter of 2 μm, and consequently $d_{f,N} = 1$ μm. For the volumetric flow rate we have taken the value from the successful implementation of deterministic ratchets for blood separation [4], namely $\phi = 1$ μL/min.

The various designs will be compared based on the dimensionless yield Y^*, which is presented via contour plots. With special hatching we indicate 1) ratchet designs which can not fractionate (as $d_{f,N}/D_y > 0.5$) and 2) ratchet designs which can not be manufactured as the required obstacle size falls below the minimal resolution of the lithography process $R_o < 0.5$ μm.

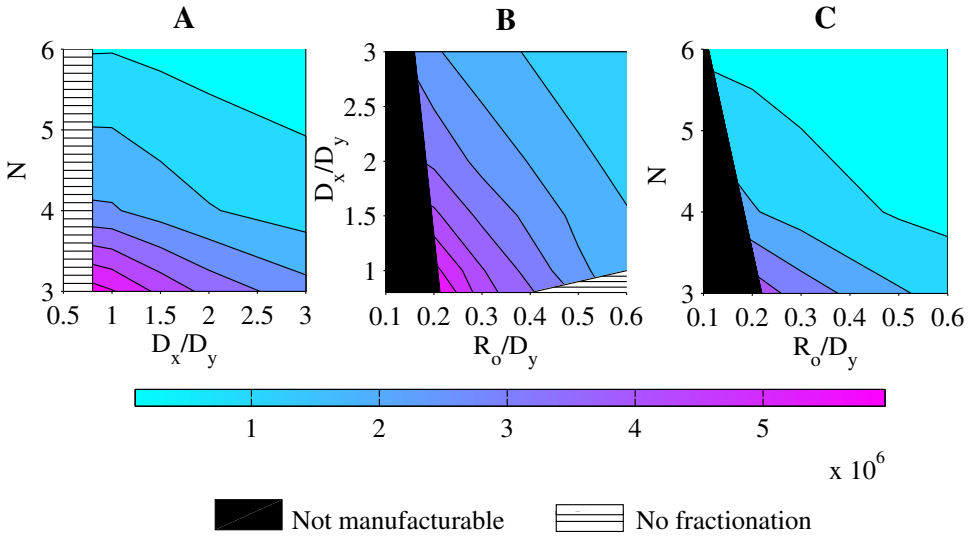

Figure 3.12: Contour plot of the dimensionless yield (Y^*) for different cross sections of the design parameter space. A) is for $R_o/D_y = 0.3$, B) is for $N = 3$, and C) is for $D_x/D_y = 1$. Regions with horizontal hatchings indicate ratchet designs which can not fractionate ($d_{f,N}/D_y \geq 0.5$), black areas indicate practical limitation of the photolithographic technique.

The evaluation data for cross section $N \times D_x/D_y$ in figure 3.12A, show that optimal yield is obtained for $D_x/D_y \lesssim 1$ which is close to the region of *non-fractionating* devices, for which hold $D_x/D_y \leq 0.7$. Figure 3.12B shows that the yield is maximal for $D_x/D_y \lesssim 1$ and $R_o/D_y = 0.2$, which is near the region of non-manufacturability. And furthermore, figure 3.12C shows that optimal yield is obtained for $N = 3$ and $R_o \approx 0.5\mu m$, which is also near the region of non-manufacturability. Hence for all three cross sections of parameter space holds that optimum in yield is determined by the constraint of either fractionation or manufacturing.

Given these constraints, we can rephrase the design rules in words: Make the ratchet as compact as possible, given the limits of the lithography process and *ability*

to fractionate.

However, this evaluation is based on assumption that the suspension is monodisperse where the *non-fractionating* region is limited by $r_p \approx d_{f,N}/D_y \geq 0.5$. For the real application (e.g. food), suspensions are polydisperse. The largest particle radius r_p present in the feed suspension is difficult to determine. Because the optimum in yield is near the constraint of *non-fractionating*, a polydisperse suspension will have a higher chance of pore plugging. We suggest to take an extra safety margin, and set $D_x/D_y \approx 1$.

Combining the evaluation results renders the following design rules for optimal yield:

- $N = 3$
- $R_o/D_y \approx 0.2$
- $D_x/D_y \approx 1$.

Note that for the optimal design, all three design rules have to be met simultaneously.

The value of the optimal dimensionless yield is around $Y^* \approx 4 \times 10^6$ (see figure 3.12), which means that a production unit with a channel volume of $V = 1\ m^3$ can fractionate about 51 m^3/day of micron-sized particles. Although a volume of 1 m^3 may sound very big for microfluidic devices, it is within practical reach as shown for example in the work of Kitamori [30, 31].

3.7 Conclusions

Lattice Boltzmann simulations have allowed us to refine the classification rules, as first formulated by Inglis and co-workers [3]. The original classification rules are based on the assumption of a parabolic flow profile within the pore between obstacles. We have shown that this hypothesis holds only for a limited class of ratchets ($D_x/D_y \geq 3, R_o/D_y \leq 1$) and based on asymmetric distribution of flow lane widths, we pose that there are two important length scales determining particle motion: the size of the first and the largest flow lane, $d_{f,1}$ and $d_{f,N}$. If $r_p < d_{f,1}$ we expect zigzag motion, and if $r_p > d_{f,N}$ we expect displacement motion.

It is likely that in the practically relevant regime with *asymmetric* flow lane distribution, and with particles in the range $d_{f,1} < r_p < d_{f,N}$, particle trajectories will show

mixed motion, which is intermediate between the zigzag and displacement motion, as can be expected based on the remarks in the work of Heller and Bruus [13].

In the range of $2 < D_x/D_y < 3$, and $R_0/D_y \leq 0.2$ the flow lane distribution deviates from that of the parabolic flow profile, but it is still symmetric - as the flow profile is only blunted compared to the parabolic flow profile.

In the regimes between ratchets with parabolic flow profiles, and *non-fractionating* ratchets ($1 < D_x/D_y < 3, R_o/D_y \geq 0.2$), the flow lane distribution is asymmetric, with $d_{f,N}$ larger than $d_{f,1}$, as computed by Eq.(3.3). This regime has practical relevance as designs with optimal yield for concentrated suspensions fall within.

For large-scale applications (e.g. food), the interest is in compact ratchet devices with optimal yield which are characterized by $N = 3, D_x/D_y \approx 1$ and $R_o/D_y \approx 0.2$, with the last constraint imposed by the limits of lithography and other ones by the constraint of *non-fractionation* via displacement motion ($r_p \geq d_{f,N} \geq 0.5D_y$).

References

[1] T. Kulrattanarak, R.G.M. van der Sman, C.G.P.H. Schroën, R.M. Boom. Classification and evaluation of microfluidic devices for continuous suspension fractionation. *Adv Colloid Interface Sci.*, **142**(2008) 53-66.

[2] L.R. Huang, E.C. Cox, R.H. Austin, J.C. Sturm. Continuous particle separation through deterministic lateral displacement. *Science.*, **304** (2004) 987-990.

[3] D.W. Inglis, J.A. Davis, R.H. Austin, J.C. Sturm. Critical particle size for fractionation by deterministic lateral displacement. *Lap Chip*, **6** (2006) 655-658.

[4] J.A. Davis, D.W. Inglis, K.J. Morton, D.A. Lawrence, L.R. Huang, S.Y. Chou, J.C. Sturm, R.H. Austin. Deterministic hydrodynamics: Taking blood apart. *PNAS.*, **130**(40) (2006) 14779-14784.

[5] K. Loutherback, J. Puchalla, R.H. Austin, J.C. Sturm. Deterministic microfluidic ratchet. *Phys Rev Lett.*, **102** (2009) 045301.

[6] J.C.T. Eijkel, A. van den Berg. Nanotechnology for membranes, filters and sieves. A series of mini-reviews covering new trends in fundamental and applied research, and potential applications of miniaturised technologies. *Lab Chip*, **6** (2006) 19-23.

[7] M. Yamada, M. Nakashima, M. Seki. Pinched flow fractionation: Continuous size separation of particles utilizing a laminar flow profile in a pinched microchannel. *Anal Chem.*, **76** (2004) 5465-5471.

[8] M. Yamada and M. Seki. Hydrodynamic filtration for on-chip particle concentration and classification utilizing microfluidics. *Lap Chip.*, **5** (2005) 12331239.

[9] B.W. Roberts and W.L. Olbricht. The distribution of freely suspended particles at microfluidic bifurcations. *AIChE J.* **52**(1) (2006) 199–206 .

[10] S. Zheng, J.Q. Liu, Y.C. Tai. Streamline-Based microfluidic devices for erythrocytes and leukocytes separation. *J Microelectromech Syst.*, **17**(4) (2008) 1029-1038.

[11] S. Yang, A. Undar and J.D Zahn. A microfluidic device for continuous, real time blood plasma separation, *Lab on a Chip*, **6**(7) (2006) 871–880.

[12] M. Faivre, M. Abkarian, K. Bickraj and H.A. Stone. Geometrical focusing of cells in a microfluidic device: An approach to separate blood plasma *Biorheol.*, **43**(2) (2006) 147–159.

[13] M. Heller and H. Bruus. A theoretical analysis of the resolution due to diffusion and size dispersion of particles in deterministic lateral displacement devices. *J Micromech Microeng.*, **18** (2008) 075030.

[14] J. Kromkamp, F. Faber, C.G.P.H. Schroën, R.M. Boom. Effects of particle size segregation on crossflow microfiltration performance: control mechanism for concentration polarisation and particle fractionation. *J Membr Sci.*, **268** (2006) 189-197.

[15] G. Brans, C.G.P.H. Schroën, R.G.M. van der Sman, R.M. Boom. Membrane fractionation of milk: state of the art and challenges. *J Membr Sci.*, *243* (2004) 263-272.

[16] H.M. Wyss, D.L. Blair, J.F. Morris, H.A. Stone, D.A. Weitz. Mechanism for clogging of microchannels. *Phys Rev E.*, **74** (2006) 061402.

[17] Z. Wu, A.Q. Liu, K. Hjort. Microfluidic continuous particle/cell separation via electroosmotic-flow-turned hydrodynamic spreading. *J Micromech Microeng.*, **17** (2007) 1992-1999.

[18] D.W. Inglis. Efficient microfluidic particle separation arrays. *Appl Phys Lett.*, **94** (2009) 013510.

[19] S.Y. Chen, G.D. Doolen. Lattice boltzmann method for fluid flows. *Ann Rev Fluid Mech.*, **30** (1998) 329-364.

[20] B.R. Long, M. Heller, J.P. Beech, H. Linke, H. Bruus, J.O. Tegenfeldt. Multidirectional sorting modes in deterministic lateral displacement devices. *Phys Rev E.*, **78** (2008) 046304.

[21] A.J.C. Ladd and R. Verberg. Lattice-Boltzmann simulations of particle-fluid suspensions. *J Stat Phys.*, **104** (2001) 1191-1251.

[22] A.J.C. Ladd. Numerical simulations of particulate suspensions via a discretized Boltzmann equation Part I. Theoretical foundation. *J Fluid Mech.*, **271** (1994) 285-309.

[23] Y.H. Qian, D. D'Humières, P. Lallemand. Lattice BGK model for Navier-Stokes equations. *Europhys Letters.*, **17** (1992) 479-484.

[24] T. Inamuro, M. Yoshino, F. Ogino. A non-slip boundary condition for lattice Boltzmann simulations. *Phys Fluids.*, **7**(12) (1995) 2928-2930.

[25] R.G.M. van der Sman. Galilean invariant lattice Boltzmann scheme for natural convection on square and rectangular lattices. *Phys Rev E.* **74**(2) (2006) 026705.

[26] A.S. Sangani, A. Acrivos. Slow flow past periodic arrays of cylinders with application to heat transfer. *Int J Multiphase Flow.*, **8**(3) (1982) 193-206.

[27] V. Ramachandran, H.S. Fogler. Plugging by hydrodynamic bridging during flow of stable colloidal particles within cylindrical pores. *J Fluid Mech.*, **385** (1999) 129-156.

[28] G. Brans, A. van Dinther, B. Odum, C.G.P.H. Schroën, R.M. Boom. Transmission and fractionation of micro-sized particle suspensions. *J Membr Sci.*, **290** (2007) 230-240.

[29] G. Brans, R.G.M. van der Sman, C.G.P.H. Schroën, A. van der Padt, R.M. Boom. Optimization of membrane geometry for micro-machined membranes. *J Membr Sci.*, **278** (2006) 239-250.

[30] T. Kitamori. Integrated micro-nano chemical and bio systems. http://www.unisa.edu.au/promo/2003/micronano.pdf.

[31] M. Tokeshi, Y. Kikutani, A. Hibara, K. Sato, H. Hisamoto, T. Kitamori. Chemical processing on microchips for analysis synthesis and bioassay. *Electrophoresis.*, **24** (2003) 3583-3594.

Chapter 4

Image analysis of particle trajectories in deterministic ratchets including comparison with computed classification rules

Abstract

Deterministic ratchets, also known as deterministic lateral displacement arrays, are microfluidic devices, which are used for size-based sorting of cells or DNA. In our previous work [1], we have refined existing classification rules describing the type of motion of particles in a ratchet device obtained via 2-D simulation of fluid flow in a periodic cell. In this paper, we compare our previous formulated classification rules with experimental particle trajectories obtained via video-microscopy of latex particles flowing through ratchets. From the video images, the particle trajectories were reconstructed using a newly developed image analysis algorithm.

Furthermore, experiment definitely show a new type of particle motion, the so-called mixed motion, which occurs when there is an asymmetric flow lane distribution in the pore space between obstacles. Mixed motion is characterized by a migration angle that falls in between the angles of the previously known types of motion, i.e. zigzag and displacement motion. The occurrence of mixed motion can be related to length scales (flow lane widths) obtained from 2-D simulations which also form the basis of the earlier formulated classification rules. Analysis of observed particle

trajectories are in reasonable agreement with classification rules. We can conclude that the classification rules [1] are a useful guide for future ratchet design.

4.1 Introduction

Deterministic ratchets, also known as deterministic lateral displacement (DLD) arrays, are microfluidic devices containing periodic arrays of obstacles. They are investigated for size-based fractionation of suspensions with mainly biological applications in mind, like sorting DNA and cells [2–6].

In our recent review paper, we have shown that these ratchet devices also have potential for fractionation of food suspensions [7], as they have much less chance of particle accumulation compared to membrane fractionation, which is the traditional choice for food applications [8, 9]. For these applications, the yields and concentration of feed suspensions need to be high, and in this, they have very different demands with respect to process design and scale, compared to the biological application for which ratchet technology is first introduced.

Obviously, the prerequisites that need to be met for food applications are stringent, and we have investigated the limits of the operation window through numerical analysis of the fluid flow through a periodic unit cell of a ratchet device having cylindrical obstacles [1]. This analysis has lead to new classification rules, which refine the previous classification rules of the inventors of the DLD device [2, 3]. The main difference being that we are able to show that the original hypothesis that a parabolic flow profile occurs in the pore space between obstacles in a single row, only holds for a limited set of ratchet designs. For a large portion of the design space, the flow profile in the pore space is asymmetric; and this determines the width of the flow lanes, as will be explained in more detail below. The size of the flow lane widths determines the type of motion of the particles, which are named zigzag or displacement motion [2, 3].

From the image analysis it has become clear that the particles can show other motion than the previously reported displacement and zigzag motion, and since the new motion is a combination of both we have denoted it as 'mixed motion'. The mixed motion is only briefly discussed in a figure caption of a paper by Heller et al. [13]. Our paper gives the first comprehensive description of this mixed motion. All types of particle motions can be characterized by a migration angle - defined with respect

to the flow direction. Zigzag motion has a zero migration angle, while displacement motion has a maximal migration angle, which is purely determined by the positioning of the obstacles. Particles showing mixed motion have a migration angle in between these extremes. Via comparison with flow lane distributions, we have formulated a hypothesis for the occurrence of mixed motion.

The numerical analysis in our previous work is based on the assumption that the fluid flow is pre-dominantly two dimensional, which holds for cylindrical obstacles with high ratios of height versus diameter [1]. As a criterion, we have assumed that particles smaller than the first flow lane will always follow the streamlines, and this may turn out to be too optimistic for particles with sizes slightly smaller than the first flow lane, especially in the case where the flow distribution in the pore space is asymmetric. Hence, this warrants experimental investigation of the validity of the refined classification rules - which is the topic of this paper.

The experiments are performed with micro-machined ratchet devices having cylindrical obstacles, through which we flow a latex particle suspension. Particle motion is observed via high-speed video-microscopy, and is quantified via image analysis, which is becoming a standard tool in colloidal science [10–12]. However, the nature of deterministic ratchets devices makes image analysis non-trivial. The particle trajectories have to be extracted from images with a complicated background, which consists of a multitude of circular cross sections of the obstacles - having a size of comparable order of the flowing particles. Furthermore, there may be multiple particles flowing simultaneously in the field of view. Above all, images of flowing particles may be missing in a number of subsequent frames, when they flow around the cylindrical obstacles and disappear in their 'shade'. To cope with these non-trivial questions, we have developed a sophisticated algorithm, which is based on the knowledge of the particle motion through ratchet devices. This algorithm will be discussed in detail in a later section.

The paper is organized as follows. First, we discuss the ratcheting principle in detail, together with a brief summary of the refined classification rules from earlier work [1]. Secondly, we discuss the materials and method used for video-microscopy. The developed algorithms for image and trajectory analysis are discussed in a separate section. Subsequently, we present the results of the analysis and discuss how they fit into the classification rules (i.e. in relation to flow lane distributions).

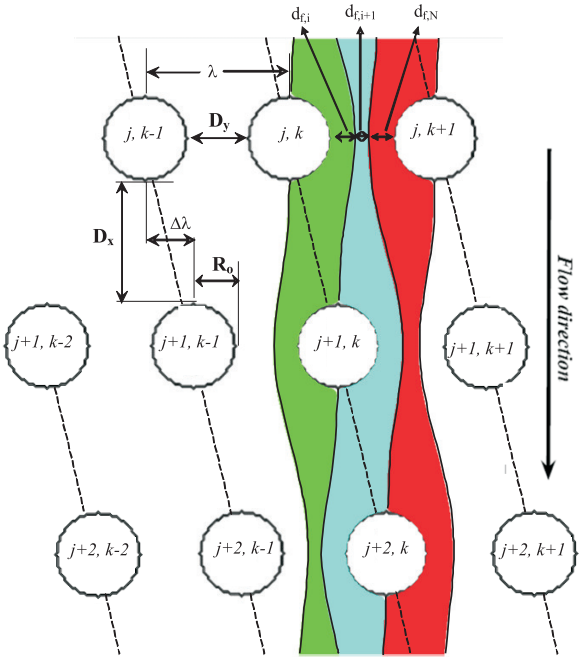

Figure 4.1: A periodic cell of DLD device with 3 obstacle rows showing geometric parameters and obstacle arrangement with flow divided into a number of flow lanes ($d_{f,i}$) which is equal to $N = 3$. Dashed line indicates displacement lanes (positions are arranged in obstacle rows with index j and displacement lane, with index k).

4.2 DLD Ratcheting principle and classification rules

The deterministic ratchets (or DLD) are characterized by a number of geometric parameters as indicated in figure 4.1, in which R_o is the radius of obstacle, D_x is the gap width between obstacles in flow direction, and D_y is the gap width perpendicular to flow. The shift of the obstacle rows, $\Delta\lambda$, is a fraction of the distance between the centers of the obstacles denoted as $\lambda = D_y + 2R_o$. The ratio of $N = \lambda/\Delta\lambda$ is the number of obstacle rows in one periodic cell.

Fractionation in DLD ratchets is based on the flow line sieving principle [14], which is based on the interplay between the driving flow field and the steric interactions of suspended particles with the solid obstacles placed in the flow field. The obstacles in the flow channel impart stagnation points in the flow field, which are connected by dividing streamlines, and the areas between the streamlines are called the flow lanes. As mentioned previously, the obstacles are arranged such that each obstacle row is shifted in lateral direction relative to the previous row.

The layout of the obstacles (see also figure 4.1 for definitions), determines the number of flow lanes [2, 3], and therewith, the fractionation that can be achieved. Initially, it is assumed that particles having a radius smaller than the width of the first flow lane will follow the streamlines, and stay within their flow lane (zigzag motion) [2, 3]. Particles having a radius larger than the first flow lane width will continuously have steric interaction with the obstacles, via which they cross the boundary of the flow lanes, and consequently will enter the adjacent lane. The particles with zigzag motion will have an overall migration angle of zero, $\theta = 0$, while particles with a displacement motion will have the maximum migration angle θ_{max}. Because of the difference in motion of particles smaller and larger than the flow lane width, fractionation will occur.

Figure 4.1, also shows the flow lanes indicated by different colors for a deterministic ratchet with $N = 3$. The dividing stream lines are drawn as solid lines between flow lanes that start at a flow stagnation point at the back of the obstacle, and end at a stagnation point at the front of an obstacle, N rows downstream at the same height. The widths of the flow lanes are indicated with $d_{f,i}$, with the largest flow lane, $d_{f,N}$ always adjacent to the obstacle.

Originally, the inventors, Austin, Sturm and co-workers [2], assumed a uniform flow profile in the pore space between the obstacles, which implies that all flow lane widths are equal, $\{d_{f,i}\} = D_y/N$. In a more recent work, they formulated a parabolic flow profile in the pore space, with all flow lanes having equal volumetric flow rate [3]. The lane width distribution is non-uniform; the first and the last lane are largest and equal in size, and determine which particle size can be fractionated. For the systems of Inglis and coworkers, the critical lane width, $d_{f,c} = d_{f,1} = d_{f,N}$, which holds well for the devices tested in their work, but does not seem to cover a large range of other ratchet designs [1, 13]. Our results show that the parabolic flow profile holds for ratchets with $D_x/D_y \geq 3$, and $R_o/D_y \leq 0.2$ [1].

In previous work [1], we have investigated the fluid flow through a periodic cell of obstacle arrays for a wide range of dimensionless geometric parameters ($N, D_x/D_y$, and R_o/D_y). Contrary to the hypothesis of Inglis et al. [3], we found an asymmetric flow lane distribution, in which the first and the last lanes are significantly larger than the middle lanes, and the last lane larger or equal to the first lane, $d_{f,1} \leq d_{f,N}$ (see figure 4.2A for examples). Figure 4.2B-D shows how the last lane width, $d_{f,N}$, depends on the various design parameters; all design parameters are extensively discussed in

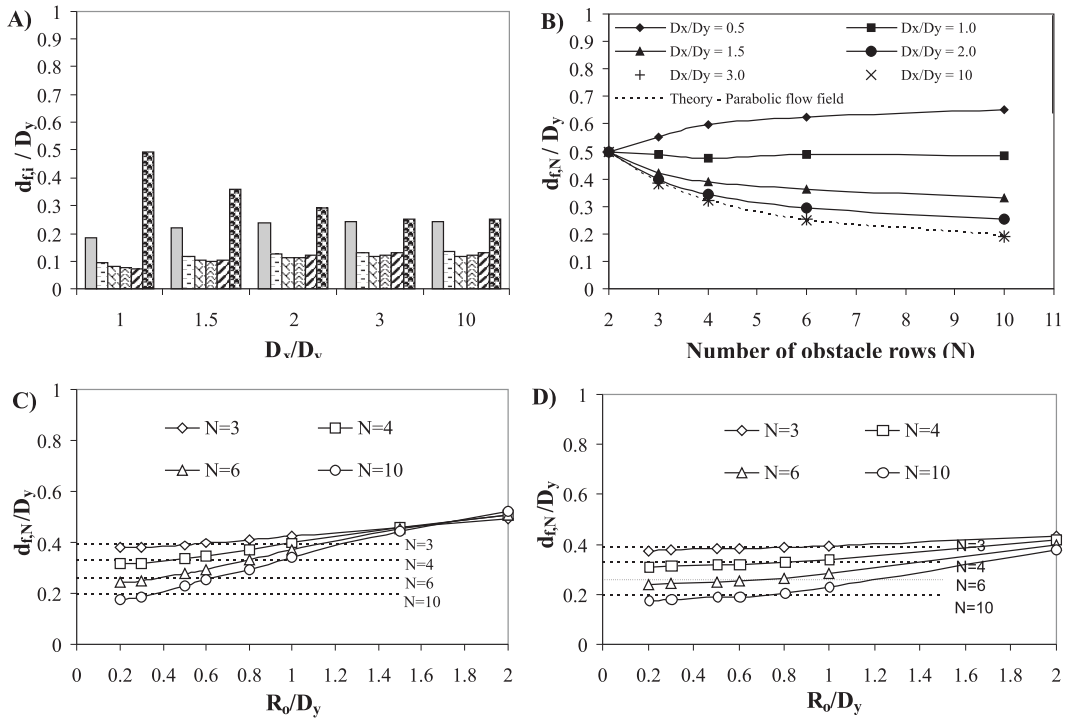

Figure 4.2: A) Flow lane width distributions of devices with $N = 6$ and $R_o/D_y = 0.6$ for various values of D_x/D_y. Ratio of last lane width $d_{f,N}/D_y$ as a function of B) N and D_x/D_y with fixed $R_o/D_y = 0.6$, as a function of R_o/D_y and N of C) $D_x/D_y = 2.0$, and D) $D_x/D_y = 3.0$ compared to the limiting values (dashed line) determined from Inglis et al. [3] and [1].

[1]. If the particle diameter exceeds 2 times the last lane width ($d_p > 2d_{f,N}$), the particle is expected to show displacement motion. Further, there is a limitation to the particle size i.e. it must fit within the pore space between the obstacles which implies $d_p < D_y$. Consequently, $d_{f,N}/D_y = 0.5$ is the upper limit for the last flow lane width. Ratchets that have higher last lane width $d_{f,N}/D_y > 0.5$ do not fractionate.

The last flow lane widths that are mentioned are based on simulation of fluid flow only, assuming that small particles with $d_p < 2d_{f,1}$ will follow streamlines and larger particles, with $d_p > 2d_{f,N}$, will show displacement motion (see figure 4.3A and 4.3C). It is expected that there will be a smooth transition going from one mode to the other, possibly resulting in mixed motion as briefly mentioned by Heller and Bruus [13]. How various modes of motion occur is investigated in this paper, in which we quantify the particle motion in detail (for more information, please consult the trajectory analysis section).

Details of the displacement motion are clearly visible in figure 4.3C. The large particles collide continuously with the cylindrical obstacles. The lubrication force between suspended sphere and cylindrical obstacle will induce the particle to partially rotate around the obstacle [16], until the drag force is sufficiently strong to drive the particle from the obstacle. During the rotation, the center of the particle crosses the dividing stream line, as $d_p > 2d_{f,1}$. Hence, upon detachment of the particle away from the obstacle, the particle ends up in the adjacent flow lane. This process is repeated at every obstacle row, which displaces the larger particles at the maximal migration angle θ_{max}, which is purely determined by the geometry of the ratchet: $\tan(\theta_{max}) = \Delta\lambda/(D_x + 2R_o)$, as indicated in figure 4.1 by the dashed lines. Obstacles on this common line are indicated with the same index k. The area between common lines with index k and $k+1$ is the *displacement lane*.

Particles that follow a zigzag path follow the streamline, and will remain within the flow lane which they enter the ratchet device (see figure 4.1). Let us follow a particle in the first flow lane, just at the right of obstacle with indexes j, k. In between obstacle rows j and $j+1$, it crosses the left boundary of displacement lane k, as it turns around obstacle j, k. Subsequently, it approaches obstacle $(j+1, k)$ of the next obstacle row and makes a partial rotation around the obstacle, but now at the left hand side. In the pore space of the third obstacle row, the flow lane is midway the two obstacles, and will pass without any steric interaction. Following the flow lane, it leaves the periodic cell, after which it will repeat an identical motion in the next cell. Consequently, a zigzagging particle enters another displacement lane after it has traversed through N obstacle rows.

A particle with a size in the range $2d_{f,1} < d_p < 2d_{f,N}$ is expected to be a candidate for mixed motion, but how it will move is unknown; we can only mention that that these trajectories are not expected to be as regular as for either zigzag or displacement motion. Clearly, the difference in particle motion needs to be investigated in detail, as is the focus of this paper and ideally translated into classification rules that later can be used to design DLD ratchet devices for e.g. food suspension.

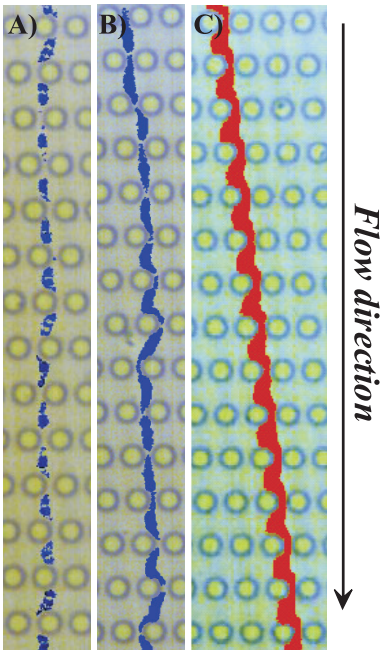

Figure 4.3: Microscopic observation of deterministic ratchets, showing A) zigzag motion of small particle ($d_{p1} < 2d_{f,1}$), B) mixed motion of particle ($2d_{f,1} < d_{p2} < 2d_{f,N}$), and C) displacement motion of large particle ($d_{p3} > 2d_{f,N}$). The ratchet design is based on $N = 6, D_x/D_y = 2, R_o/D_y = 0.6$, with $\lambda = 16.06$ μm, and $R_o = 4.38$ μm and the height of the pillar is 30 μm. The nominal diameters of particles are $d_{p1} = 3.4$ μm, $d_{p2} = 4.0$ μm, and $d_{p3} = 5.0$ μm. From the simulations for this design we know that $2d_{f,1} = 3.46$ μm and $2d_{f,N} = 4.28$ μm. All frames are superimposed for particle tracking. In A), it is evident that some particle images are missing as explained in the image analysis section.

4.3 Materials

4.3.1 Particle suspensions

Four different suspensions of latex particles (Interfacial Dynamics Corporation, USA), were used, having nominal diameter diameters of 3.4, 4.0, 5.0, or 6.0 μm. The actual size distribution was measured using dynamic light scattering with Malvern Mastersizer 2000. The stock suspensions are diluted with MilliQ water to a volume concentration of 0.05%.

Table 4.1: Geometry of the devices, and the first, and the last flow lane widths obtained from simulation [1].

Group	N	D_x/D_y	R_o/D_y	$2\times d_{f,1}/D_y$	$2\times d_{f,N}/D_y$
A	3	1	0.67	0.67	0.98
	4	1	0.64	0.51	0.98
	6	1	0.60	0.37	0.98
	10	1	0.67	0.27	0.98
B	6	2	0.60	0.47	0.59
	6	2	0.90	0.45	0.67
C	3	3	0.67	0.75	0.76
	4	3	0.64	0.63	0.64
	6	3	0.60	0.49	0.51

4.3.2 Microfluidic device

The devices were produced by Delft Institute of Microelectronics and Submicron-technology (DIMES), affiliated with Delft University of Technology, the Netherlands. Using lithography and highly anisotropic DRIE processes, the cylindrical obstacles were etched in silicon, as described by Hao and co-workers [18].

As shown in figure 4.4, there are 2 devices within one chip of 15 by 15 mm. The basic design comprises of a single outlet and two inlets, one for the suspensions and one for the carrier fluid (MilliQ water). In one device up to 200 obstacle rows may be placed, which corresponds to 80-128 periodic cells; the devices are specifically built for trajectory analysis.

The different ratchet designs we have tested are shown in table 4.1. For all these designs, the height of the obstacles, is 30 μm, and the radius is in the range of $3.95 \lesssim R_o \lesssim 10.17$ μm, as determined from SEM images (see figure 4.4). The measured dimensions are in good agreement with the specifications of the design, and these are used for further analysis.

The ratchet devices were placed in a module (Fluidic connect 4515) from Micronit microfluidics B.V., the Netherlands. HPFA/PEEK tubes with an internal diameter of 50 μm were used to connect the chip to syringes (1000 μL, Hamilton) placed in syringe-pumps (Harvard Apparatus model 11 plus) set at constant flow rates of 3-10 $\mu L/hr$.

From the size of the first and last flow lane, ($d_{f,1}$ and $d_{f,N}$), listed in table 4.1 follows that the devices used in our experiments can be subdivided into 3 groups.

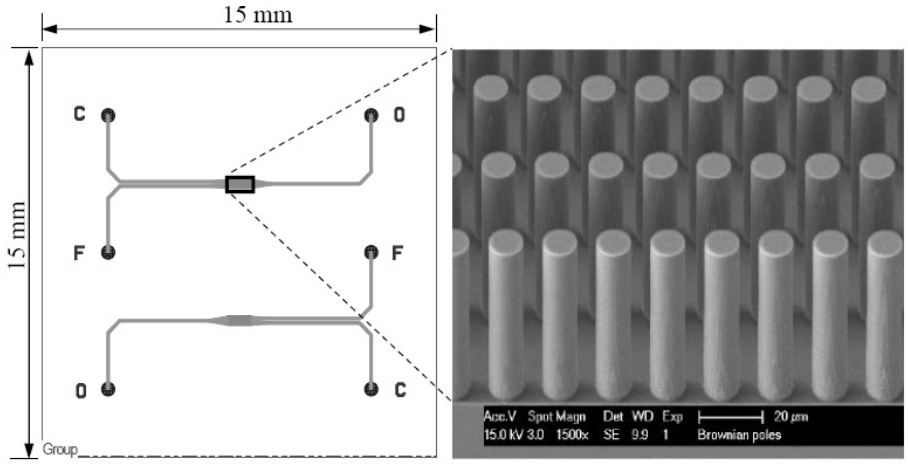

Figure 4.4: On the left, we show a schematic representation of the chip layout. The actual size of the chip is 15 by 15 mm. F denotes inlet for the suspensions, C: the inlet for the carrier fluid (MilliQ water), and O: the outlet. On the right, we show a SEM image of the silicon obstacles.

- Group A, with $D_x/D_y = 1$, has an asymmetric flow lane distribution, and $2d_{f,N} \approx D_y$. Hence, it is likely that particles can not perform displacement motion - but mixed motion may be possible.

- Group B, with $D_x/D_y = 2$, has also an asymmetric flow lane distribution, but $2d_{f,N} < D_y$, and we expect all three types of motions to occur.

- Group C, with $D_x/D_y = 3$, has a symmetric flow lane distribution, and $2d_{f,1} \approx 2d_{f,N} < D_y$). For these devices, we expect only zigzag and displacement motion and no mixed motion.

4.3.3 Image acquisition

The motion of particles through the ratchet devices was observed with a Zeiss Axioplan microscope, equipped with a Motion Pro high-speed camera (Redlake MASD Inc., San Diego). Video images are directly stored on the hard disk of a computer, which operates the camera using MIDAS software. Depending on the size and the speed of the object and required quality of the video, we have used a magnification of 10-100, and a frame of rate 125-400 frames/sec. The resolution of a video image can vary from 128×48 up to 1280×1024 pixels.

4.4 Image analysis

Obtaining trajectories of particles, traversing deterministic ratchets, via image analysis is not trivial. Firstly, the background is complex due to the array of cylindrical obstacles, which appears in the video images as circular objects with 'similar' size as the moving particles. Secondly, often there are multiple particles moving through the ratchet devices, which have to be distinguished from one another. Further, the distance that a particle travels between frames can be more than one particle diameter, and this makes it hard to follow the entire trajectory of the particle. Above all, traversing particles tend to disappear in the shade of the obstacles and reemerge later as depicted in figure 4.3A, which shows that particle trajectories consist of multiple unconnected parts, and for quantification the complete particle trajectory has to be reconstructed.

To overcome the above mentioned hurdles we have developed an extensive algorithm to detect particle images, and construct particle trajectories from these images. Details of the algorithm will be discussed below; here we only mention that it was implemented in MATLAB software (Image Processing Toolbox), but below we will give a general description.

The sequence of steps required to construct the particle trajectories from the video images is shown in figure 4.5. After image enhancement, we determine the background consisting of the cylindrical obstacles. After subtracting the background image from the camera image, the particles can be detected, particle trajectories re-constructed, and migration angles determined. The first four steps are discussed in the subsections below, and trajectory analysis is described in the section thereafter.

4.4.1 Image enhancement

All recorded video images are stored in RGB format. The image is converted into gray scale $I(x, y)$ via the transformation [15]:

$$I(x, y) = 0.2989R(x, y) + 0.5870G(x, y) + 0.1140B(x, y) \tag{4.1}$$

with $R, G, B(x, y)$ the intensity of the red, green and blue channels of pixel x, y. Our images have a strong signal in green, and this transformation rendered a significantly enhanced contrast. The contrast was further enhanced through the MATLAB function

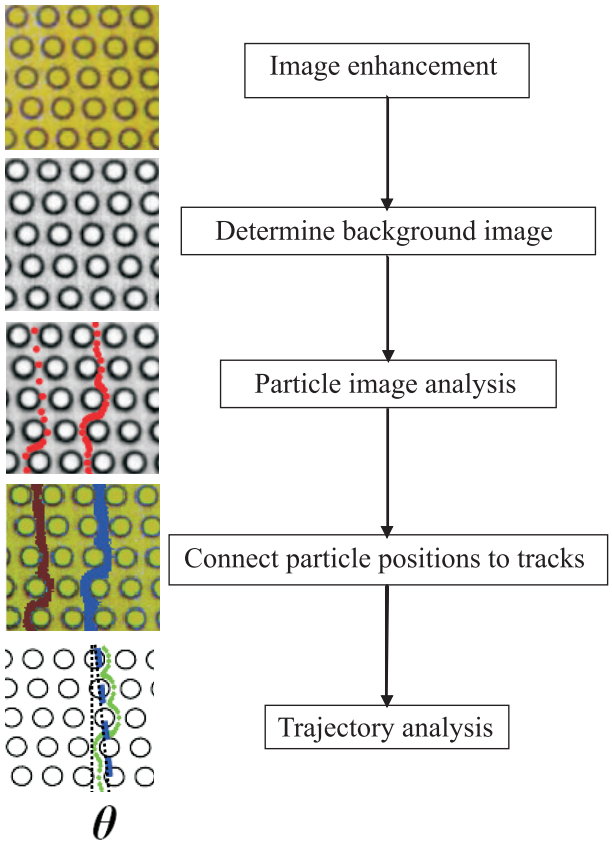

Figure 4.5: Five steps used for image and trajectory analysis process.

"adapthisteq", which transforms the values using contrast-limited adaptive histogram equalization using a sampling region of 10×10 pixels. The enhanced images are denoted by $J(x, y)$.

4.4.2 Background image

To discriminate particle images from the cylindrical obstacles in a video image, we have first determined the background image via averaging all pixel intensities of the enhanced gray images from the complete movie. Through this, it is possible to locate obstacles and possibly static dust and dirt particles. The background image is denoted as:

$$BI = \overline{J}(x, y) = \sum_{n=1}^{NF} \frac{J_n(x, y)}{NF} \tag{4.2}$$

with NF the total number of frames in a single movie.

4.4.3 Particle image analysis

To determine particle images, the background image (BI) is first subtracted from each enhanced gray image (J_n):

$$Z_n = J_n - BI \tag{4.3}$$

Then, the subtracted image (Z_n) is converted to a binary image using an intensity threshold, (Th_l), which is set at the value of $Th_l \approx 0.2 Pix_{max}$ with $Pix_{max} = 255$, the maximum value of the intensity in J_n. The output binary image has values of 0 (black) for the $Z_n(x, y) < Th_l$ and 1 (white) for all others. Via the MATLAB function "bwareaopen", we detect particle images, which are recognized as blobs of interconnected pixels having value of "1". To discriminate particle images from noise or small dust particles, we have used a threshold for the blob size, Th_p. The pixel threshold (Th_p) is adjusted to the nominal size of used particles, via

$$Th_p = \alpha \left(\frac{\pi r_p^2}{\Delta p^2} \right) \tag{4.4}$$

Here r_p is the nominal radius of particles, and Δp is the pixel size, both measured in microns. α accounts for the fraction of the particle image, having a Gaussian intensity profile, which is lost by the conversion into a binary image. In this study, we have used $\alpha = 0.2$. Through the MATLAB function "regionprops", all blobs, recognized as particle images, are labeled, and their areas (in pixels), and the coordinates of their centers ($x_{i,j}$ and $y_{i,j}$) are computed.

4.4.4 Particle tracking

The labeling of particle images by MATLAB is done on a frame-by-frame basis, and identical particles can have different labels in subsequent frames, due to their movements. Hence, we have to establish the identity of particles in each frame, and connect the positions of identical particles into a particle trajectory.

Often, particles disappear in the shade of obstacles, as shown for example in figure 4.3A, and are thus missing from a video frame. In our experiments the number of subsequent frames, in which the particle is missing, can run up to 6 frames, before it reappears again. Furthermore particles might also be missing from a frame if its

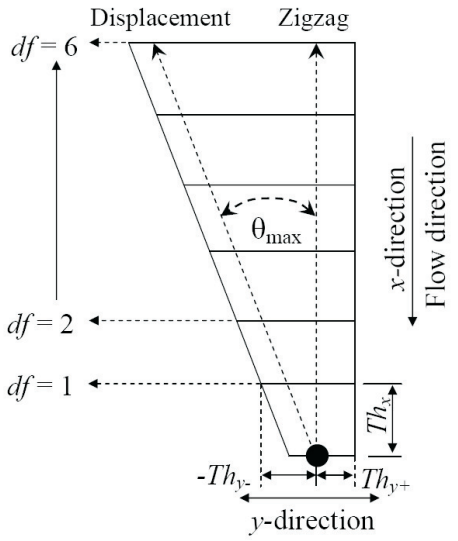

Figure 4.6: Search area for missing particles to establish trajectories. • is the origin of the search area at $df = 0$. df is a counter of the difference between frames that particles are missing in which the search area grows with df.

blob size is below the threshold (Th_p). Hence, our trajectory analysis has to consider this, and we use the expected particle behavior as a guideline. The minimum angle of displacement being 0 for zigzag motion, and highest for displacement motion (θ_{max}), and this limits the searching area in the subsequent frames; a trapezoid shape as indicated in figure 4.6. The variable df counts the difference between current frame f, and previous frames $f - df$; and we allow df to run up to a maximum of 6 missing frames.

The origin of this search area is at the position of the particle in frame f. $Th_{x,df}$ is the estimated maximal displacement of particles in the flow direction, and is based on the average velocity $\overline{u}_x$, the frame rate (F, frames/sec) and the porosity ε which is the fraction of pore space in an obstacle row (accounting for the change in average velocity in the pore space). The threshold is computed as follows:

$$Th_{x,df} = df \frac{3\overline{u}_x}{F\varepsilon\Delta p} \tag{4.5}$$

with the porosity:

$$\varepsilon = \frac{D_y}{2R_o + D_y} \tag{4.6}$$

$Th_{y-,df}$ is the maximum displacement of a particle in negative y-direction in frame

$f - df$ (see Eq. 4.7), when showing displacement motion, and for subsequent frames, $Th_{x,df}$ and $Th_{y-,df}$ grow linear with the number of missing frames df. $Th_{y+,df}$ is the extension of the search area in the positive y-direction (with respect to the origin), corresponding to the maximum displacement of a zigzagging particle in this direction (see Eq. 4.8).

$$Th_{y-,df} = df \tan(\theta_{max}) Th_x + 2R_o \Delta p \tag{4.7}$$

$$Th_{y+,df} = df(2R_0 + 2r_p - \Delta\lambda)\Delta p \tag{4.8}$$

The purpose of the particle tracking algorithm shown in figure 4.7 is to relabel the records of the data set produced by the particle image recognition routine "regionprops". This data set comprises of particle positions $(x_{f,i}, y_{f,i})$ and the labels $(index_{f,i})$ assigned by MATLAB. The particle tracking routine will assign the label $(Label_{f,i})$, and particles with the same label $Label_{f,i}$ are assumed to be identical particles, and from their positions $x_{f,i}$,$y_{f,i}$ the trajectory can be constructed.

Via the algorithm shown in figure 4.7, the relabeling of particle images is performed. For the first frame, we keep the labels $(Label_{1,i} = index_{1,i})$, as assigned by MATLAB. The variable $nParticles$ is used for labeling the particles, which enter the field of view in frame $f > 1$. The initial value of $nParticles$ is the number of particles in frame $f = 1$.

Subsequently, we perform an iteration over all subsequent frames $(2 \leq f \leq NF)$, and all particles in that frame (Num_f). Via the function "FindLabelInPreviousFrames", we try to link the current particle with $Label_{f,i}$ to a previously identified particle in frames $f - 1$, upto $f - 6$ in case of missing frames. The function returns zero, if it was not able to identify the particle. This happens if the current particle is a new particle entering the ratchet, or the particle was not observed in 6 earlier frames (e.g. has been hidden in the shade of obstacles), or its blob size has been below the threshold Th_p. Consequently, we treat them as new particles and assign the value of $nParticles + 1$ to $Label_{f,i}$, and increase the counter $nParticels$.

The function "FindLabelInPreviousFrames" first detects whether a particle at position $(x_{f,i}, y_{f,i})$ is in the search area df defined in figure 4.6. It computes the vector $(\Delta x, \Delta y)$ between particle position $(x_{f,i}, y_{f,i})$ and $(x_{f-df,j}, y_{f-df,j})$. If the vector falls within the search area df, the function assumes the particle at $(x_{f,i}, y_{f,i})$ to be identical to particle at $(x_{f-df,j}, y_{f-df,j})$, and assign $IdentifiedLabel$ to $Label_{f-df,j}$, and assigns

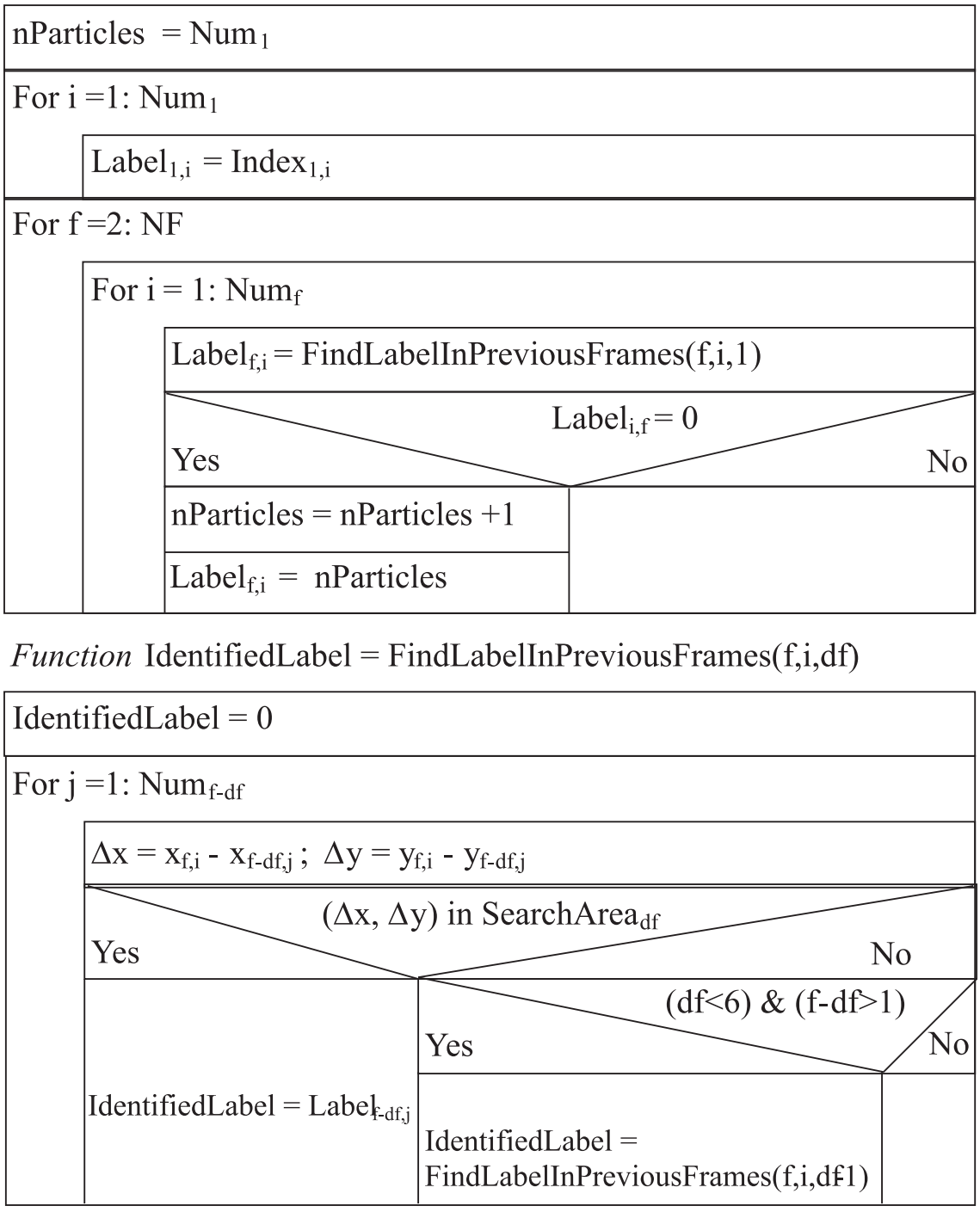

Figure 4.7: The algorithm used to track particles in consecutive frames.

$IdentifiedLabel$ as its return value. If the particle is not found in search area df, the function calls itself in a recurrent fashion, if $df < 6$ and $f - df > 1$. These constraints hold because we have allowed for a maximum of 6 missing frames, and the backward search can only be performed up to the first frame.

4.5 Trajectory analysis

Via the image analysis algorithm described above, we have obtained particle trajectories of each individual particle, which are analyzed further. We use two quantities for characterization of particle motion; firstly, the migration angle, which is also used in a recent paper by Inglis [17]. A second measure that we consider is the number of obstacle rows, M, that the particle has traversed between entering and leaving a *displacement lane*. We denote this as the retention in a displacement lane. Its advantage above the migration angle is that it is discrete - and will have little error in the measurement.

4.5.1 Migration angle

As defined above, the migration angle is the angle that the trajectory makes with respect to the flow direction. In deterministic ratchets the angle is always in the range $0 \leq \theta \leq \theta_{max}$. We compute the migration angle corresponding to a particular particle trajectory, via linear regression. From the tangent of the fitted lines, one can determine the angle θ.

However, the flow direction may not perfectly aligned with the vertical axis of the video image. Henceforth, we have to correct for that when computing the migration angles of the trajectories. For that we first determine the tilt angle, the device makes with the vertical axis in the video images, θ_{tilt}, via image analysis of the background image BI, and the true migration angle of a trajectory θ_{track} is computed.

4.5.2 Retention in a displacement lane

The line through the center positions of obstacles having an angle of θ_{max} with the flow direction forms the bounding line of a displacement lane, as shown in figure 4.1. Now we can determine whether the particle positions within a particular trajectory are above or below the bounding lines of the displacement lanes. Subsequently,

we determine the displacement of the particle in the vertical (flow) direction, while it resides in a particular displacement lane. The displacement can be expressed in terms of the distance between obstacle rows ($D_x + 2R_o$), and is performed for every displacement lane the particle traverses. This renders a sequence of numbers, $\{M_k\}$, indicating how many obstacle rows the particle has crossed during its residence in a displacement lane.

For particles with zigzag motion this sequence contains all equal numbers, with $M_k = N$ the number of obstacle rows in a single periodic cell. For particles with displacement motion, this sequence contains a single number, which is equal to the number of obstacle rows in the field of view. For particles with mixed motion, this sequence contains multiple numbers, with at least one $M_k > N$.

Via the determination of the retention of the particle in the displacement lanes, we have a discrete method for establishing the type of motion of the particle. The method requires though that the length of the particle track in the flow direction is at least larger than $2N$ times the distance between obstacle rows ($D_x + 2R_o$), and this may pose a challenge for especially mixed motion.

4.6 Results and discussion

4.6.1 Particle distribution

The particle size distributions of the suspensions are summarized in table 4.2, where we have listed the mean particle size $D(0.5)$, together with $D(0.1)$ and $D(0.9)$ values corresponding to the lower and upper 10 % size limit of the particles. The deviation from the average particle size is at most 1.0 μm, for A and B. The span of the suspension C and D, is considerably larger (2 micron), and the distributions overlap. For the analysis of the particle trajectories, we start from the average particle size keeping the $D(0.1)$ and $D(0.9)$ values as limits.

4.6.2 Image analysis

The above described image analysis algorithm has proven to be powerful and robust, allowing simultaneous analysis of many particles. We have obtained many particle tracks, which run through the whole field of view. A single video movie contains 2-12 trajectories, and in a single frame, we typically observe 1-5 particles. The search

Table 4.2: Particle size distributions as measured in the Malvern Mastersizer 2000.

Suspension	D(0.1) μm	D(0.5) μm	D(0.9) μm
A	2.8	3.2	3.8
B	3.6	3.8	4.2
C	4.2	5.1	6.2
D	5.0	5.9	7.0

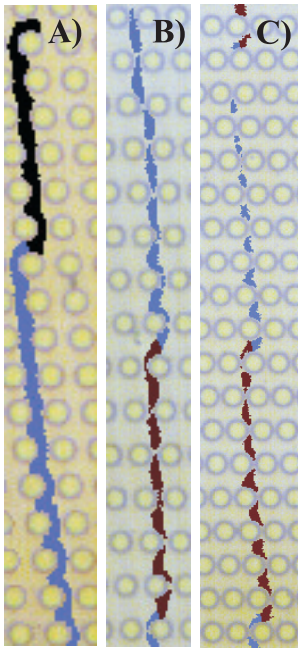

Figure 4.8: Mixed motion in different designs of $N = 6$, A) $D_x/D_y = 1$ with particles having nominal size $d_p = 6$ μm, B) $D_x/D_y = 2$ with $R_o/D_y = 0.6$ and C) $D_x/D_y = 2$ with $R_o/D_y = 0.9$ with particles having nominal size $d_p = 4$ μm, showing irregular motion. Particle trajectory in the same displacement lane is indicated by the same color.

method for missing particles has performed satisfactory, and mostly no more than 2-4 frames at a row are missing for a single particle trajectory.

The recorded video images clearly show the existence of mixed motion, as shown for example in figure 4.8, where a particle moves in difference designs of devices with $N = 6$. Often the mixed motion is quite irregular. In figure 4.8A, a particle first resides for 6 obstacle rows in the displacement lane, after which it stays within the next displacement lane for the remainder of the trajectory. In figure 4.8B, the particle resides in the first displacement for at least 8 obstacle rows, while in the second displacement lane it resides for 7 obstacle rows. In figure 4.8C the mixed motion appears regular,

where the particle resides for 9 obstacle rows in both first and second displacement lane. Figure 4.8 colors from retention in a displacement lane analysis.

4.6.3 Comparison particle trajectories with classification rules

Experiments are performed with all ratchet designs listed in table 4.1, and all particle suspensions that allow passage of particles through the ratchet (as a constraint we have taken $d_p/D_y < 0.8$). The particle trajectories are analyzed in turns of migration angle and retention of displacement lane.

The results on the migration angle, are presented in figures 4.9-4.11, where we have plotted the dimensionless migration angle, $\theta_{track}/\theta_{max}$, as a function of the dimensionless size of particles, d_p/D_y, in which d_p is the mean particle diameter shown in table 4.2. The horizontal error bars are based on the $D(0.1)/D_y$ and $D(0.9)/D_y$ values from the same table. On average, we have obtained 16 particle trajectories from each experiment, and we have determined the error interval from these values, displayed in the graphs as vertical error bars of the data points.

In all graphs, we also displayed which type of motion is expected, indicated by regions in the graph, having different shades of gray. The vertical dashed lines separating these regions are determined by the conditions $d_p/D_y = 2d_{f,1}/D_y$, and $d_p/D_y = 2d_{f,N}/D_y$, where $d_{f,1}$ and $d_{f,N}$ denote the widths of the first and last flow lanes (data from a previous paper listed in table 4.1). The size of the particle, d_p, with respect to these flow lane widths determines the expected type of motion. Hence, for particle sizes within the white area, zigzag motion is expected, in the light gray area mixed motion is expected, and in the dark gray area displacement motion is expected.

In the same graphs, we also indicated the type of motion as determined from the residence of particles in displacement lanes through different markers; triangles ($\triangle$) for zigzag motion, filled circles ($\bullet$) for mixed motion, and crosses ($\times$) for displacement motion. As stated above, each data point represents the average result of about 16 particle trajectories. Hence, the observed type of motion displayed in the graph is based on the type of motion shown by the majority of particle trajectories.

The graphs are grouped according to the classification from table 4.1, and that is also the order in which we will discuss the results.

In the ratchet devices of group A, we expect to observe only zigzag motion, and mixed motion. The experimental results obtained for these devices are shown in figure 4.9, and indeed, in the experiments no displacement motion is observed. In one

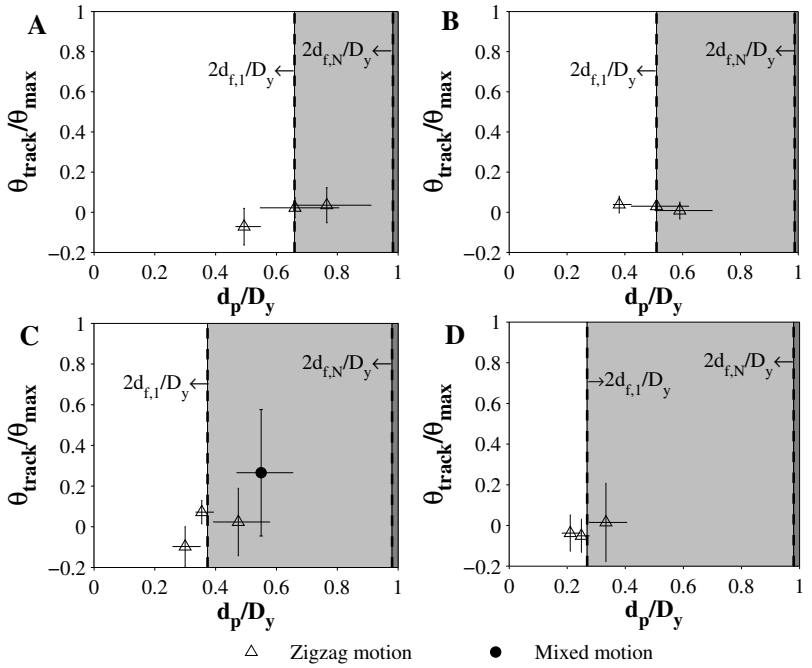

Figure 4.9: Particle trajectories in devices of $D_x/D_y = 1$ with A) N=3, B) N=4, C) N=6, and D) N=10 represented as $\theta_{track}/\theta_{max}$ as function of the dimensionless ratio of particle diameter to the gap between obstacles (d_p/D_y).

experiment, particles displayed mixed motion, and their particle size is in the range $2d_{f,1} < d_p < 2d_{f,N}$. In the remainder of the experiments, the particles displayed zigzag motion. Taking into account the (sometimes, relatively large) error intervals of the particle size, these observations are in agreement with our expectations that zigzag motion occurs if $d_p < 2d_{f,1}$.

For ratchet devices in group B, all three types of motions are expected to be observed, and this has been the case as displayed in figure 4.10, except for a single experiment. In the device with $R_o/D_y = 0.6$ shown in figure 4.10A, the diameter of particles with mixed motion falls in the range, $2d_{f,1} < d_p < 2d_{f,N}$, which is relatively narrow for this device. Since the error interval of the particle diameter is relatively small, there is a high certainty for this observation. For the device with $R_o/D_y = 0.9$ shown in figure 4.10B, the uncertainty in the particle diameter falling in the range $2d_{f,1} < d_p < 2d_{f,N}$, is unfortunately relatively large and thus we can not falsify the expectation.

For ratchet devices in group C, only zigzag and displacement motion is expected.

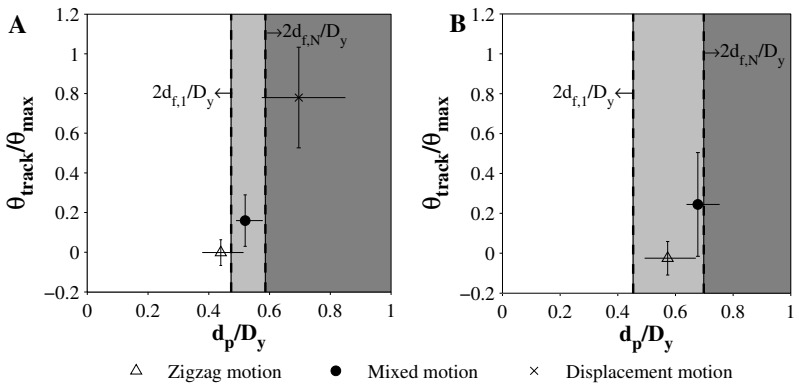

Figure 4.10: Particle trajectories in the device designs of $D_x/D_y = 2$ with A) $R_o/D_y = 0.6$ and B) $R_o/D_y = 0.9$ show $\theta_{track}/\theta_{max}$ as a function of the dimensionless ratio of particle diameter to the gap between obstacle (d_p/D_y).

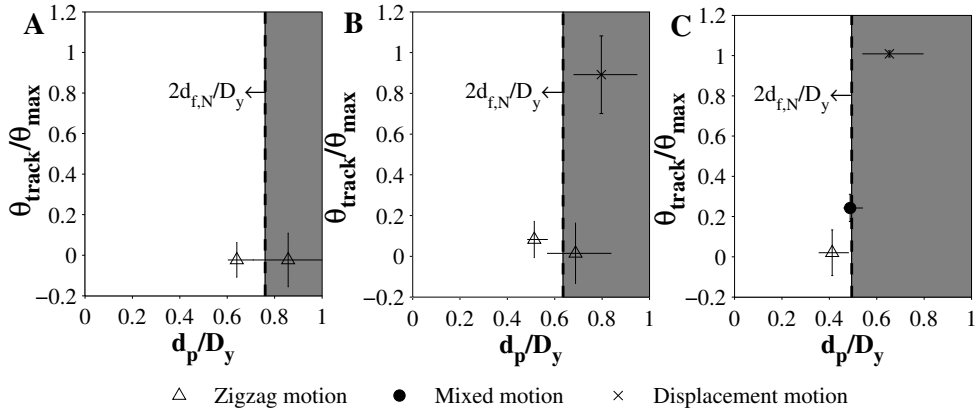

Figure 4.11: Particle trajectories in the device designs of $D_x/D_y = 3$ with A) $N = 3$, B) $N = 4$ and C) $N = 6$ show $\theta_{track}/\theta_{max}$ as a function of the dimensionless ratio of particle diameter to the gap between obstacle (d_p/D_y). The simulation result shows that $d_{f,1} \approx d_{f,N}$.

The experimental results are displayed in figure 4.11, and surprisingly, we observed one single instance of mixed motion, as shown in figure 4.11C, which is right on the boundary between the region between zigzag and displacement motion, which can be the reason for this motion.

4.7 Conclusion

The presented image analysis algorithm has shown to be a powerful tool to construct particle trajectories in deterministic ratchets (DLD). From the particle trajectories, we have established the existence of mixed motion in deterministic ratchet devices, with migration angle $0 < \theta < \theta_{max}$, besides known migration motions such as zigzag motion, and displacement motion. Mixed motion is in general irregular, and appears as a mixture of zigzag and displacement motion.

For all particles showing mixed motion, holds that their particle size falls within the range, $2d_{f,1} < d_p < 2d_{f,N}$ (the experimental uncertainty is small). Although we have to cope with considerable experimental uncertainty (mainly in the size distribution of particles expected critical sizes based on flow lane widths), the observations of mixed motion are within the expected range, and this indicates that with the knowledge of the flow lane widths, one can obtain a reasonable estimate on the type of motion particles will show.

Appendix: Deterministic ratchets for particle separation fabricated with Si MEMS technology

Using Si-based MEMS technologies obstacles with pre-defined geometries and accurate sizes and locations within deep micro-channels can be fabricated and integrated in lab-on-a-chip systems. Configurations with N between 3 and 10, and varying distances between obstacles ($0.5 \leq D_x/D_y \leq 3, 0.6 \leq R_o/D_y \leq 0.9$) are tested. Figure A1 shows the main steps of the fabrication process. The 2.5 μm and 6 μm SiO_2 layers deposited and patterned on the front and back sides of a silicon wafer (A1a), are used as a hard mask during the DRIE etching of the silicon obstacles (A1b). These obstacles are high aspect ratio cylindrical pillars with a width between 7-20 μm and height of 60-80 μm. After removing the SiO_2 hard mask, the ratchet structures are oxidized. The 100 nm thermal oxide layer on the surface (A1c) insures a hydrophilic surface for better wetting. Finally, a glass wafer is used to seal the channels and to allow the observation of particle trajectories (A1d).

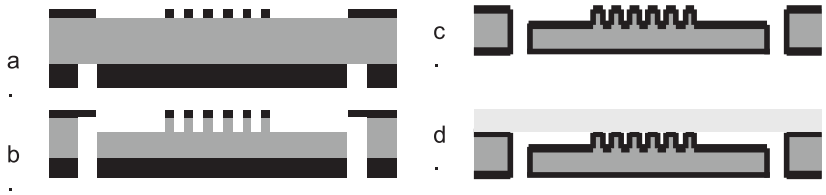

Figure A1: Schematic drawing of the fabrication process.

The anisotropic etching of Si with high aspect ratio is carried out in an Adixen (AMS100 I-speeder) using Bosch process [19]. Each single stage of the process consists of the following steps: (a) anisotropic etching using SF_6 chemistry, (b) sidewall passivation using C_4F_8 chemistry, and finally (c) passivation removal by O_2 plasma. The etching parameters employed are summarized in table I. The SEM images of all etched structures are observed in SEM XL-50 equipment. Figure A2 shows the SEM image of a fabricated array of silicon obstacles in a microchannel.

The appendix was extracted from the published proceeding as: H.T.M. Pham, T. Kulrattanarak, R.G.M. van der Sman, C.G.P.H. Schroën, R.M. Boom and P.M. Sarro. Deterministic ratchets for particle separation fabricated with Si MEMS Technology. *Proceedings of the Eurosensors XXIII conference.* Procedia Chemistry, 1 (2009) 345-348.

Table I: The main parameters used for the in-situ isotropic and anisotropic etching steps.

Parameters	Value	
	Isotropic etching	Anisotropic etching
SF_6 (sccm)	400	400
C_4F_8 (sccm)	-	280
Power(W)	1500	1500
Pressure(mbar)	2.3×10^{-2}	2.3×10^{-2}
Temperature (°C)	-10°C	-10°C

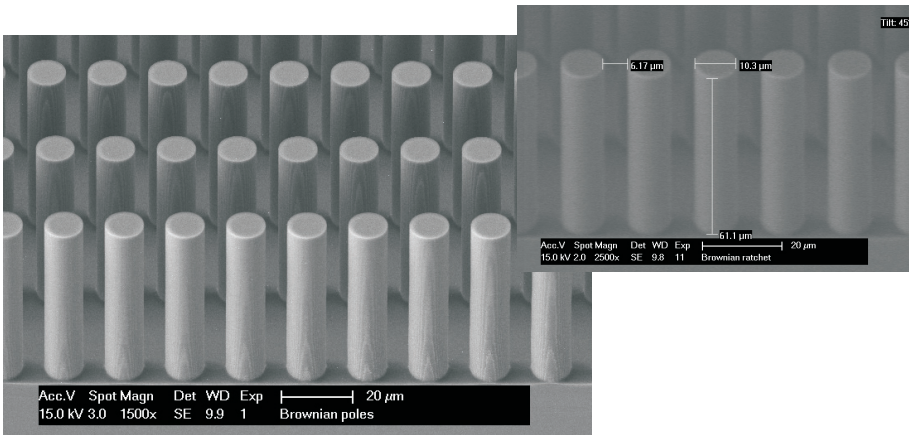

Figure A2: SEM images of the 60 μm height silicon obstacles etched by a highly anisotropic DRIE process.

References

[1] T. Kulrattanarak, R.G.M van der Sman C.G.P.H. Schroën, and R.M. Boom. Refinement of classification rules for deterministic ratchets through 2-D flow field simulation. *Chapter 3*.

[2] L.R. Huang, E.C. Cox, R.H. Austin and J.C. Sturm. Continuous particle separation through deterministic lateral displacement. *Science*, **304** (2004) 987-990.

[3] D.W. Inglis, J.A. Davis, R.H. Austin and J.C. Sturm. Critical particle size for fractionation by deterministic lateral displacement. *Lap on a Chip*, **6** (2006) 655-658.

[4] J.A. Davis, D.W. Inglis, K.J. Morton, D.A. Lawrence, L.R. Huang, S.Y. Chou, J.C. Sturm and R.H. Austin. Deterministic hydrodynamics: Taking blood apart. *PNAS*, **130** (2006) 14779-14784.

[5] K. Loutherback, J. Puchalla, R.H. Austin and J.C. Sturm. Deterministic microfluidic ratchet. *Phys. Rev. Lett.*, **102** (2009) 045301.

[6] J.V. Green, M. Radisic, and S.K. Murthy. Deterministic Lateral Displacement as a Means to Enrich Large Cells for Tissue Engineering. *Anal. Chem.*, **81** (2009) 91789182.

[7] T. Kulrattanarak, R.G.M van der Sman, C.G.P.H. Schroën and R.M. Boom. Classification and evaluation of microfluidic devices for continuous suspension fractionation. *Adv. Colloid Interface Sci.*, **142** (2008) 53-66.

[8] J. Kromkamp, F. Faber, C.G.P.H. Schroën and R.M. Boom. Effects of particle size segregation on crossflow microfiltration performance: Control mechanism for concentration polarisation and particle fractionation. *J. Membr. Sci.*, **268** (2006) 189-197.

[9] G. Brans, C.G.P.H. Schroën, R.G.M. van der sman and R.M. Boom. Membrane fractionation of milk: state of the art and challenges. *J. of Membr. Sci.*, **243** (2004) 263-272.

[10] J.C. Crocker and D.G. Grier. Methods of digital video microscopy for colloidal studies. *J. Colloid Interface Sci.*, **179** (1996) 298310.

[11] L. Dongning, Y. Zhang, Y. Sun and W. Yan. A multi-frame particle tracking algorithm robust against input noise. *Meas. Sci. Technol.*, **19** (2008) 105401.

[12] S.S. Rogers, T.A. Waigh, X. Zhao and J.R Lu. Precise particle tracking against a complicated background: polynomial fitting with Gaussian weight. *Phys. Biol.*, **4** (2007) 220227.

[13] M. Heller and H. Bruus. A theoretical analysis of the resolution due to diffusion and size dispersion of particles in deterministic lateral displacement devices. *J. Micromech. Microeng.*, **18**(2008) 075030.

[14] J.C.T. Eijkel and A. van den Berg. Nanotechnology for membranes, filters and sieves. *Lab Chip*, **6** (2006) 19-23.

[15] Mathworks. *http://www.mathworks.com/access/helpdesk/help/techdoc/index.html?/access/helpdesk/help/techdoc/creating_plots/f2 − 1667.html*

[16] J. Frechette and G. Drazer. Directional locking and deterministic separation. *J. Fluid Mech.*, **627** (2009) 379-401.

[17] D.W. Inglis. Efficient microfluidic particle separation arrays. *Appl. Phys. Lett.*, **94** (2009) 013510.

[18] H.T.M. Pham, T. Kulrattanarak, R.G.M. van der Sman, C.G.P.H. Schroën,

R.M. Boom and P.M. Sarro. Deterministic ratchets for particle separation fabricated with Si MEMS Technology. *Proceedings of the Eurosensors XXIII conference.*, Procedia Chemistry, 1 (2009) 345-348.

[19] A.A. Ayon, R.L. Bayt, K.S. Breuer. Deep reactive ion etching: a promissing technology for micro and nanosatellites. *Smart Mater. Struct.*, 10 (2001) 1135-1144.

Chapter 5

Analysis of particle motion in deterministic ratchet via experiment and simulation

Abstract

Deterministic lateral displacement (DLD) ratchets are microfluidic devices, which are used for size-based sorting of cells or DNA. Based on their size, particles are showing different kinds of motion, leading to their fractionation. In earlier studies, so-called zigzag, and displacement motions were observed, and in recent work from our group [9], we have shown that also *mixed motion* occurs, which is irregular in nature.

In this work, we have investigated *mixed motion* in depth by numerical and experimental analysis. Via 3D simulations, we computed explicit particle trajectories in DLD, and were able to show that there are two critical length scales determining the type of motion. The first length scale $d_{f,1}$ is the first flow lane width, which determines the transition between zigzag motion and mixed motion. The other length scale, $d_{f,c}$, determines the transition between mixed motion and displacement motion. Our experiments confirm the validity of the new particle classification rules, based on the length scales $d_{f,1}$ and $d_{f,c}$. Contrary to simulations, which show regular, periodic behavior for mixed motion, we have found irregular trajectories in our experiments, which can be due to non-hydrodynamic interactions like Brownian motion or colloidal forces. In conclusion, the 3D simulations have lead to the classification rules that are a considerable improvement to 2D simulations that allow identification of $d_{f,1}$ but not

of $d_{f,c}$.

5.1 Introduction

Deterministic ratchets, also known as deterministic lateral displacement (DLD) arrays, are microfluidic devices used for size-based fractionation of suspensions. Although these ratchets are mainly investigated in biological applications (e.g. cells, DNA and blood) [1–4], they also have potential for large-scale fractionation of food suspensions [5].

Nowadays, fractionation of food materials receives much interest since it is expected to lead to more sustainable and economical use of agrifood materials, leading to multiple functional ingredients. Membranes have been considered for fractionation of liquid foods [6, 7], but especially the larger components were found to influence the fractionation process negatively. As an alternative technique, we have considered microfluidic devices, and found that DLD (deterministic lateral displacement) ratchets are the most promising option [5]. The main benefit of DLD ratchets over membranes is that they have much lower chance of particle blockage, as their characteristic dimension is larger than the particles, where in membranes the pores are smaller than the particles.

The fractionation principle of deterministic (DLD) ratchets is based on the flow line sieving principle [10]. When particles are large enough, hydrodynamic and steric interaction with regularly arranged obstacles can make them deviate from their original streamline, via which they can end up in a different outlet than smaller sized particles. In deterministic ratchets, one uses the interaction of the particles with an array of obstacles. A periodic cell of such an array is shown in figure 5.1. The space between two obstacles in a single row is subdivided into a number of flow lanes, which are separated by dividing streamlines. These dividing streamlines originate from the back of the obstacle, and end at the stagnation point at the front of an obstacle directly upstream. Each flow lane can be characterized by its width, $d_{f,i}$, between obstacles.

Particles larger than the first lane width, $d_{f,1}$, will have hydrodynamic/steric interaction with the obstacles, which makes them cross the dividing streamline, and they will end up in the adjacent flow lane. An important characteristic of the deterministic ratchet is that subsequent obstacle rows are displaced a fraction, $\Delta\lambda$, of the obstacle interspacing λ. Hence, particles which have crossed the dividing streamline via inter-

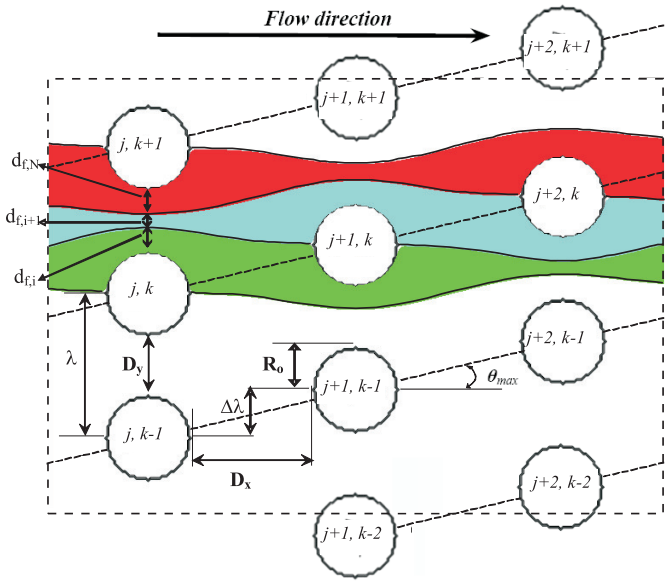

Figure 5.1: A periodic cell with $N = 3$ obstacle rows. Various geometrical parameters are indicated with their symbols and measures. The space between obstacles in an obstacle row is subdivided into N flow lanes, each indicated by a different color. Flow lanes are characterized by its width $d_{f,i}$. The bounding (solid) lines of the flow lanes are dividing streamlines, originating and ending at stagnation point at the surface of the obstacles. Dashed lines indicate the migration angle θ_{max} of particles showing displacement motion, and are the boundaries of the displacement lanes, within which the displacing particles move.

action with an obstacle will bump onto the obstacle of the following row (*displacement* motion). Inglis [2] noted that particles larger than $d_{f,1}$ will move along in the lattice direction under angle $\theta_{max} > 0$ relative to the flow direction, as shown in figure 5.1.

The flow lane distribution is determined by the various geometrical parameters of the obstacle array, as displayed in figure 5.1, in which comprise R_o is the radius of obstacle, D_x is the gap width between the obstacles in flow direction and D_y is the gap width perpendicular to the flow. The shift of the obstacle rows, $\Delta\lambda$, is a fraction of the distance between the centers of the obstacles denoted as $\lambda = D_y + 2R_o$. The ratio of $N = \lambda/\Delta\lambda$ is an integer, and indicates the number of obstacle rows in one periodic cell.

Initially Inglis et al. [2] assumed that between the obstacles a parabolic flow profile existed, with all flow lanes having equal volumetric flow rate. The lane width distribution was assumed non-uniform, with the first and the last lanes being equal and largest in size ($d_{f,1} = d_{f,N}$), and this was called the critical lane width ($d_{f,c}$).

Based on this, Inglis and coworkers concluded that particles with radius $r_p > d_{f,c}$ will show displacement motion, and zigzag motion otherwise.

From 2-D flow field simulations [8], we have found that for a large class of ratchet designs, with $D_x/D_y \leq 3$ and $R_o/D_y > 0.2$, the flow lane width distribution is *asymmetric*, with the first lane width, smaller than the last one, $d_{f,1} < d_{f,N}$. For these devices we found different particle behavior, which we have named *mixed* motion [9], and which shows migration angles θ between those for zigzag (0) and displacement motion (θ_{max}). We were able to summarize the behavior of particles in three simple rules based on the asymmetric distribution of flow lane widths computed by 2D simulation. 1) Zigzag motion ($\theta = 0$) occurs if $r_p < d_{f,1}$. 2) Displacement motion ($\theta = \theta_{max}$) occurs for particles with $r_p > d_{f,N}$. 3) Mixed motion with migration angle $0 < \theta < \theta_{max}$, occurs if $d_{f,1} < r_p < d_{f,N}$.

Although these preliminary classification rules are good to have, and can be used as a guideline for ratchet design, it is clear that more in depth simulations are needed to substantiate our findings. For this, we use 3D-simulations in which suspended particles are explicitly taken into account, which cannot be done through 2D simulations. Using the Lattice Boltzmann method [11, 13] we compute the motion of a single particle through a periodic cell of a DLD device, having the same dimensionless design parameters $(N, D_x/D_y, R_o/D_y)$ as the devices used in our experiments, which are especially designed for observation of mixed motion. The results of the 3D, and 2D simulations, are compared to the experimental results, and new classification rules will be presented at the end of the paper.

5.2 Material and Methods

5.2.1 Deterministic ratchet devices

We have designed deterministic ratchet devices that allow observation of mixed motion, based on the size distributions of the particle suspensions, and the classification rules presented in the introduction. The designs are made such that one part of the particles suspensions is expected to show zigzag motion, and other part of the particle suspensions is expected to show mixed motion. The resulting designs are listed in Table 5.1. They are described in terms of dimensionless design parameters N, D_x/D_y and R_o/D_y.

Table 5.1: Geometry of the devices and the first ($2d_{f,1}/D_y$) and the last flow lane widths ($2d_{f,N}/D_y$) determined from 2D-simulation [8].

Design	N	D_x/D_y	R_o/D_y	$2d_{f,1}/D_y$	$2d_{f,N}/D_y$
I	4	1.5	0.5	0.59	0.74
II		1.5	0.2	0.59	0.66
III	6	1.5	0.2	0.46	0.51
IV		2.0	0.2	0.47	0.48

The ratchet devices are produced by Delft Institute of Microelectronics and Submicrontechnology (DIMES), affiliated with Delft University of Technology, the Netherlands. Using lithography and highly anisotropic DRIE processes, the cylindrical obstacles are etched in silicon, as described by Hao and co-workers [27]. For all these designs holds, that the height of the obstacles is 40 μm, the radius is in the range of $1.6 \lesssim R_o \lesssim 4\mu$m, and the space between the obstacles is in the range , $8 \leq D_y \leq 9$ μm.

Each ratchet device has a chip size of 15 by 15 mm with 2 inlets, one for the particle suspensions and another one for the carrier fluid. All inlets and outlets have the same width, which is taken equal to the width of 3 periodic cells ($L_y/\lambda = 3N$). The length of the devices is taken such that if particles would show displacement motion they would end up in the outlet, and hence its length is $L_x/\lambda = 3N \times N$.

5.2.2 2D flow field simulations

The flow lane width of the new ratchet designs are computed with the 2D flow simulation model described in previous work [8]. We have numerically simulated the fluid flow through a periodic cell of various ratchet designs using the Lattice Boltzmann method, based on the generally applied Lattice BGK scheme, having 9 velocities on a two-dimensional lattice (D2Q9) [11, 12]. The no-slip boundary condition at the interface of fluid and obstacles is implemented using the bounce back method, as discussed in a review of Ladd and Verberg [13]. The pressure drop over the periodic cell is implemented using the 'pressure periodic' boundary conditions as proposed by Inamuro and co-workers [14]. The Lattice Boltzmann code is validated against a benchmark problem of Sangani and Acrivos [15].

From the LB simulations, we obtain the steady state velocity field $\mathbf{u(x)}$ throughout the periodic cell of the ratchet. From the flow field we determine the sizes of the

flow lanes; the differential equations between location $\mathbf{x}$ and velocity $\mathbf{u}$, $d\mathbf{x}/dt = \mathbf{u}(\mathbf{x})$ are solved with Euler integration, and we compute the trajectories of small tracer particles, with $r_p \ll \{d_{f,1}\}$, which will follow the fluid streamlines.

The width of flow lanes, $d_{f,i}$, is determined by releasing tracer particles in the space between obstacles j, k and $j, k+1$ (see figure 5.1) in which j identifies the obstacle row number and k identifies the bounding line of a displacement lane. The tracer particle will perform a zigzag motion. Via releasing particles equidistantly in the pore space, we obtain the flow lane distribution. The computed flow lane distributions, as used in the design of the ratchet devices (Table 5.1).

5.2.3 3D numerical simulations

The motion of spherical particles through a ratchet device is simulated with a 3-dimensional Lattice Boltzmann code, which performs Direct Numerical Simulation (DNS) of a sphere in a flowing fluid. In DNS the sphere is fully resolved, meaning that the particle diameter is larger than the grid spacing $d_p \gg \Delta x$ [17]. In DNS simulation, only few assumptions have to be made, and in this particular case, the assumptions are the form of the lubrication force between sphere and no-slip boundaries if the gap between particle and boundary is smaller than the grid spacing, $h < \Delta x$.

The particular Lattice Boltzmann code we have used is the Two-Relaxation-Time (TRT) scheme. The TRT scheme has been developed by Ginzburg [23], and is an efficient implementation of the Multi-Relaxation-Time (MRT) scheme [19, 20]. MRT schemes are known to eliminate the viscosity-dependent error in the effective radius of suspended particles and obstacles immersed in the flow. Via careful tuning of the degrees of freedom (DOF) of the TRT scheme, the error in the effective radius can be reduced significantly [18, 20, 23]. For implementing the no-slip boundary conditions on the moving sphere, obstacles and confining microchannel, we have used the traditional bounce-back method, as originally developed by Ladd [24]. Chun and Ladd recently have stated that the bounce-back method in combination with the TRT scheme is a very viable choice for implementing DNS simulations of suspensions with Lattice Boltzmann, in terms of accuracy, efficiency and ease of implementation [20], which we have shown in more detail in a recent paper [18]. There we have shown that for flowing suspended spheres, the optimal value of the DOF should adhere the following heuristic:

$$(\frac{1}{\omega^+} - \frac{1}{2})(\frac{1}{\omega^-} - \frac{1}{2}) = \frac{1}{4} \tag{5.1}$$

with $\lambda^+ = 1-\omega^+$ and $\lambda^- = 1-\omega^-$ the eigenvalues of the Lattice Boltzmann collision operator, for respectively the even and odd non-hydrodynamic modes [18, 23]. λ^- is related to the viscosity of the fluid, via $\nu_f = c_s^2(\frac{1}{\omega^-} - \frac{1}{2})\Delta t$, with $c_s^2 = \frac{1}{3}(\Delta x/\Delta t)^2$ the speed of sound squared. λ^+ is not related to any physical property of the fluid and renders a DOF to minimize the error in the effective radius of the suspended sphere. In earlier work [18], the accuracy of the TRT scheme was extensively benchmarked, therefore we will use the method as such.

For the lubrication force between the moving sphere and cylindrical obstacles at small distances, we use the hypothesis of Adamczyk et al. [16] - as was done in a recent paper on deterministic ratchet devices by Drazer and coworkers [25]. Adamczyk states that the hydrodynamic interaction (lubrication force) between an unconfined sphere of radius a approaching a cylinder of radius R, is equal to the hydrodynamic interaction between that particular sphere, with radius $r_{p,1} = a$, and a second, immobile sphere of a radius twice as large as that of the cylinder, i.e. $r_{p,2} = 2R$. We have tested the hypothesis of Adamczyk and found that it is valid at short distances $h/r_p \ll 1$. For distances further away the effect of the confining walls become noticeable - but this effect is sufficiently covered by the Lattice Boltzmann TRT scheme.

In summary, if the gap between sphere and cylindrical obstacle is less than one grid spacing, an explicit lubrication force acts on the particle - which is added to the force exerted on the particle by the fluid, as computed via the imposition of the no-slip boundary condition on the particle. As is stated in the original work of Ladd [24], the explicit lubrication force is truncated beyond a certain cut off length - which is here taken equal to the grid spacing Δx. Hence, if $h \geq \Delta x$ the lubrication force is zero.

The lubrication force scales with r_p/h, and diverges if the gap goes to zero, $h \to 0$, which is physically unrealistic [17]. A common practice is to let lubrication force saturate beyond a certain length scale, which can be interpreted as the particle roughness [17, 21, 22]. Here we take as the limiting length scale $h_{min} = 0.05 r_p$. Furthermore, following Melrose and Ball [21], we assume a Hookean spring force to act on the particle if $h < h_{min}$, which is linear with $h - h_{min}$. A sufficiently stiff spring will prevent the gap to become significantly smaller than h_{min}.

Simulations are performed for one single periodic cell of a deterministic ratchet. The fluid flow will be driven via a pressure gradient over the periodic cell. This

pressure gradient can be imposed via pressure periodic boundary conditions along the flow direction, as follows from the scheme of Inamuro [14].

Also, for the suspended sphere we assume periodic boundary conditions in the flow direction. If the particle is crossing the pressure periodic boundary, the computation of the force imposed by the fluid on the particle has to account for the fact that there is a jump in the pressure between inlet and outlet. The initial position of the particle is midway the first and second row of obstacles, in front of a gap between two obstacles, and it is positioned midway the confining walls of the microchannel. Initially the fluid is at rest, and starts flowing due to the applied pressure gradient. To eliminate start-up effects in the particle trajectory, we allow the particle to traverse the periodic cell more than once; a particle which leaves the computational domain will enter the domain again at the opposite side.

At the confining walls of the microchannel, of height H, we impose no-slip boundary conditions using the half-way bounce-back method, [18, 20]. As mentioned, at the remaining boundaries of the computation domain, we use regular periodic boundary conditions for both the fluid flow as for the suspended spheres.

5.2.4 Experimental setup

The latex suspensions are obtained from Interfacial Dynamics Corporation (USA), and have different nominal diameters, namely 3.4, 4.0, 5.0, or 6.0 μm. The actual size distribution has been measured using dynamic light scattering with Malvern Mastersizer 2000 [9]. The stock suspensions are diluted with MilliQ water to a volume concentration of 0.05%.

The ratchet devices are placed in a module (Fluidic connect 4515) from Micronit microfluidics B.V., the Netherlands. PEEK tubes with an internal diameter of 150 μm are used to connect the chip to syringes (1000 μL, Hamilton) placed in syringe-pumps (Harvard Apparatus model 11 plus) set at constant flow rates of 4 $\mu L/hr$. One inlet is fed with the particle suspension, and the other outlet is fed with MilliQ water; the carrier fluid.

During the start-up of the experiment, 0.25 wt % Synperonic PEF108 solution is first pumped into the device to drive out air bubbles and pre-treat the surface of the device to prevent particle adhesion [26]. After all bubbles are eliminated, we pump the solution through the chip for 30 minutes, after which we switch to particle suspensions.

The motion of particles through the ratchet devices is observed with a Zeiss Ax-

ioplan microscope, equipped with a Motion Pro high-speed camera (Redlake MASD Inc., San Diego). Video images are directly stored on the hard disk of a computer, which operates the camera using MIDAS software. Depending on the size and the speed of the particle and required quality of the video, we have used a magnification of 20-200, and a frame rate of 200-300 frames/sec. The resolution of a video image can vary from 128×48 up to 1280×1024 pixels.

From the video images, particle trajectories are extracted with a sophisticated image analysis algorithm, which we have described in detail in previous work [9]. The algorithm is implemented in MATLAB software using the Image Processing Toolbox. From the particle trajectories, we can obtain the migration angle, which describes the direction of the particle trajectory with respect to the flow direction [9].

5.3 Results and Discussion

5.3.1 Comparison 3D-simulation with 2D-simulation

Via the 3D simulations we compute the trajectories of particles traversing the periodic cell of the ratchet designs listed in Table 5.1, for particle with $2d_{f,1} \lesssim d_p < D_y$. In figures 5.2 and 5.3, we show the results for designs II and III, which are also illustrative for other devices. In these figures, we indicate the trajectories of particles (3D simulation) and superimposed them on the flow lanes computed with 2D flow simulations.

The particle trajectories converge to a periodic motion, after they traverse once or twice the periodic cell. Remarkably, this limiting periodic motion is independent of the initial position of the particle, as we concluded from several simulations where we only changed the initial position (results not shows). Similar periodic trajectories, independent of initial position, were also observed by Drazer and coworkers [25] for simulations with Stokesian Dynamics.

The 3D simulations confirm that particles show zigzag motion, if their radius is smaller than the first flow lane width, $d_p < 2d_{f,1}$. In both figures 5.2A and 5.3, one can observe that these particles remain within their flow lanes. For larger particles as shown in 5.2B, we observe that they exhibit displacement motion. They continuously bump into the obstacles, and move along the lattice direction having an angle of θ_{max} with the flow direction. However, the particles do not do this as expected, but at

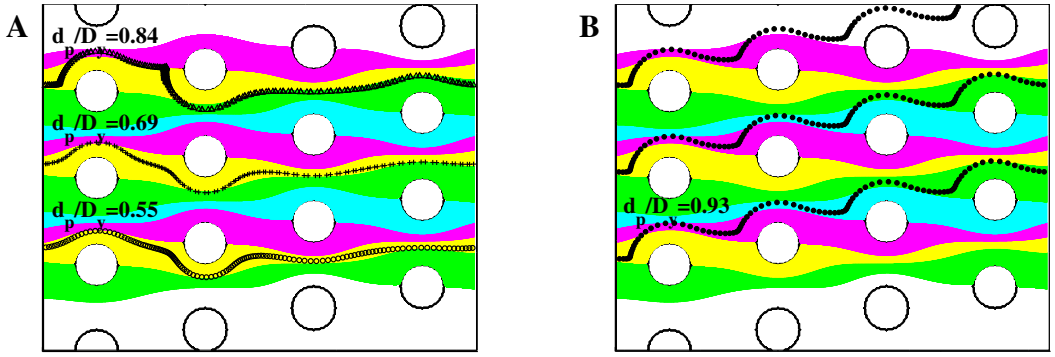

Figure 5.2: Particle motion after the first cycle obtained via 3D-simulation of explicite particles in fluid flow through a periodic cell of ratchets with $N = 4, R_o/D_y = 0.5$, and $D_x/D_y = 1.5$ with A) $d_p/D_y = 0.55, 0.69$ and 0.84, B) $d_p/D_y = 0.93$ superimposed on the flow lanes obtained from 2-D flow field simulation giving $2d_{f,1}/D_y = 0.59$ and $2d_{f,N}/D_y = 0.74$. Flow lanes are given in different colors.

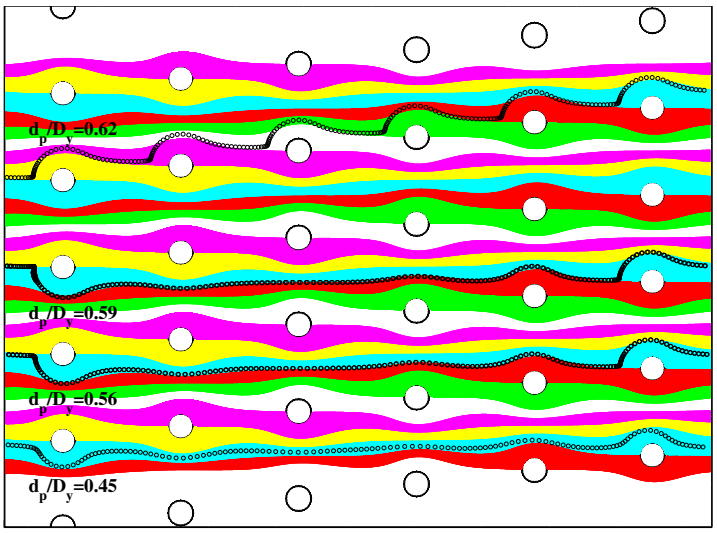

Figure 5.3: Particle motion after the first cycle obtained via 3D-simulation of explicite particles in fluid flow through a periodic cell of ratchets with $N = 6, R_o/D_y = 0.2$, and $D_x/D_y = 1.5$ with $d_p/D_y = 0.45, 0.56, 0.59$ and 0.62 superimposed on the flow lanes obtained from 2-D flow field simulation giving $2d_{f,1}/D_y = 0.46$ and $2d_{f,N}/D_y = 0.51$. Flow lanes are given in different colors.

larger length scale, which appears not to be correlated with $d_{f,N}$ nor with the critical lane width as computed from the theory of Inglis [2]. This length scale determining displacement motion will be denoted as the critical length scale $d_{f,c}$. In table 5.2 we have listed this critical length scale for all investigated ratchet designs. For all designs holds that $d_{f,c} > d_{f,N}$.

Table 5.2: The critical length scales for the investigated devices, 1) $d_{f,I}$ (Inglis, 2) $2d_{f,1}/D_y$ and $2d_{f,N}/D_y$, obtained from 2D-simulation, and 3) the critical length scale $2d_{f,c}/D_y$ obtained from the 3D particle simulations.

N	D_x/D_y	R_o/D_y	$d_{f,I}/D_y$ [2]	$2d_{f,1}/D_y$	$2d_{f,N}/D_y$	$2d_{f,c}/D_y$
4	1.5	0.5	0.65	0.59	0.74	0.93
	1.5	0.2	0.65	0.59	0.66	0.86
6	1.5	0.2	0.52	0.46	0.51	0.62
	2.0	0.2	0.52	0.47	0.48	0.78

For particles with an intermediate size, $2d_{f,1} < d_p < 2d_{f,c}$, the 3D simulations show a different type of motion, but it is different from the experimentally observed mixed motion. During the hydrodynamic interaction with the obstacles, the intermediate sized particles are crossing the dividing streamline. However, they do that twice, and return to their original flow lane. For a large part of their trajectory, they follow the dividing streamline, which bounds their original flow lane. Quite a number of trajectories of these intermediate sized particles approach the stagnation point near obstacles closely, and the particles are slowed down significantly during this approach - which is caused by the (dissipative) hydrodynamic interaction with the obstacle. Contrary to the experimentally observed mixed motions, these trajectories are *regular*, and have a migration angle of zero, as in the case of zigzag motion. We still think that the computed trajectories are related to the experimentally observed mixed motions. We suppose that in the experiments the intermediate sized particles, also approach the stagnation points closely, and slow down. In this position, they are prone to non-hydrodynamic interactions, like Brownian motion or colloidal forces, which could deviate them from the computed *ideal* trajectory, and make them move either above or below the obstacle. This can make the experimentally determined trajectories for mixed motion, highly irregular, and give them an intermediate migration angle in the range $0 < \theta < \theta_{max}$.

The occurrence of three types of particle motion in the 3D simulations, namely zigzag, displacement and the *ideal* mixed motion, indicate there are two length scales determining the particle motion. The first length scale is the width of the first flow lane $d_{f,1}$, as postulated in our earlier classification rules. The second length scale, $d_{f,c}$, determines the occurrence of displacement motion, and appears not to be correlated with the largest flow lane width $d_{f,N}$, and is to be determined via explicit 3D particle simulations. Particles within length scales $2d_{f,1} < d_p < 2d_{f,c}$ are expected to show

Table 5.3: Particle size distributions as measured in the Malvern Mastersizer 2000.

Suspension	$D(0.1)\mu m$	$D(0.5)\mu m$	$D(0.9)\mu m$
A	2.8	3.2	3.8
B	3.6	3.8	4.2
C	4.2	5.1	6.2
D	5.0	5.9	7.0

mixed behavior, and this is tested in practice in the next section.

5.3.2 Experimental results

The particle size (distributions) of the suspensions are illustrated in table 5.3, which lists the mean particle size, $D(0.5)$, together with the $D(0.1)$ and $D(0.9)$ values, which correspond to the lower and upper 10 % size limit of the particles. The experimental particle trajectories are analyzed in terms of average particle size, $D(0.5)$, and we take the $D(0.1)$ and $D(0.9)$ values as a measure for the breadth of the size distribution, which is reflected in the error bars.

Examples of particle trajectories as observed for design I from table 5.1 by video microscopy are shown in figure 5.4. In figure 5.4A we present a trajectory of a particle from suspension A (see table 5.3), which is showing zigzag motion. In figures 5.4B, C and D, we present trajectories of particles showing mixed motion, for particles from suspension D. One can clearly observe the irregularity of the mixed motion (as also observed in [9]), which starkly contrasts with the regular motion observed in the 3D simulations.

In most cases, particle adhesion has been limited or absent, as shown in figure 5.5B for suspension D flowing through design I. However, this is not always the case, and this can influence the particle trajectory considerably, as illustrated for suspension D and design II, where we observed severe particle adhesion to the obstacles (figure 5.5A). Particle adhesion is clearly a single particle event, and is probably due to colloidal forces between particles and obstacles. Despite the particle adsorption, it is still possible for particles to pass, via moving below or above the adhered particle. But adhered particles will definitely influence the local flow field and hydrodynamic interactions of particles and obstacles, and this may contribute to the irregularity of the observed mixed motion.

For each experiment, we have obtained numerous particle trajectories, which were

Table 5.4: Number of particle moving in different ranges of migration angles ($\tilde{\theta} = \theta/\theta_{max}$). The superscripts $^{A-D}$ indicate the suspensions used, as listed in table 5.3.

N	R_o/D_y	D_x/D_y	$\bar{d_p}/D_y$	Number of particle trajectories			
				$\tilde{\theta} < 0.1$	$0.1 \leq \tilde{\theta} < 0.5$	$0.5 \leq \tilde{\theta} \leq 0.9$	$\tilde{\theta} > 0.9$
4	0.5	1.5	0.64^{C}	146	19	1	1
			0.74^{D}	21	5	0	1
4	0.2	1.5	0.4^{A}	145	86	0	0
			0.64^{C}	21	8	3	0
			0.74^{D}	1	8	2	1
6	0.2	1.5	0.36^{A}	354	9	1	0
			0.42^{B}	9	7	0	0
			0.56^{C}	1	8	26	5
6	0.2	2.0	0.42^{B}	219	11	0	0
			0.56^{C}	41	25	12	13
			0.65^{D}	5	10	9	15

analyzed and characterized in terms of the migration angle, which will be presented in dimensionless form, $\tilde{\theta} = \theta/\theta_{max}$. As a measure for the distribution of the obtained migration angles, we have listed in table 5.4, the number of trajectories having migration angles within a certain range.

Within the range $\tilde{\theta} < 0.1$, particles show zigzag motion, and within the range $\tilde{\theta} > 0.9$, particles show displacement motion. Particle trajectories within the other ranges are showing mixed motion. From the table we can observe that for each device the majority of the small particles show zigzag motion. With increasing particle size, the migration angles increase, but only minority of particles show displacement motion, as aimed for in our design.

5.3.3 Comparison experiment with simulation

In this section, we use the migration angles of the particles as a function of the particle size, and compare them with the new classification rules, which are based on the numerically obtained length scales $d_{f,1}$ and $d_{f,c}$. The migration angles presented are the average over all migration angles obtained for a particular combination of suspension and ratchet device, as indicated in table 5.4. This comparison is shown in figure 5.6; the dashed lines indicate the length scale at which the transitions of

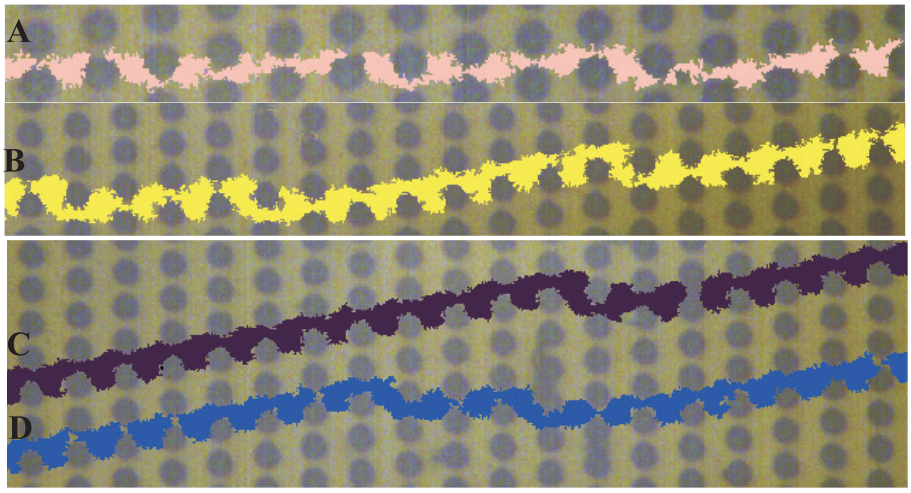

Figure 5.4: Particle trajectories obtained from image analysis [9] in devices with $N = 4, R_o/D_y = 0.2$ and $D_x/D_y = 1.5$ in which A) zigzag motion of suspension A occurs, and B-D) show mixed motion of suspension D.

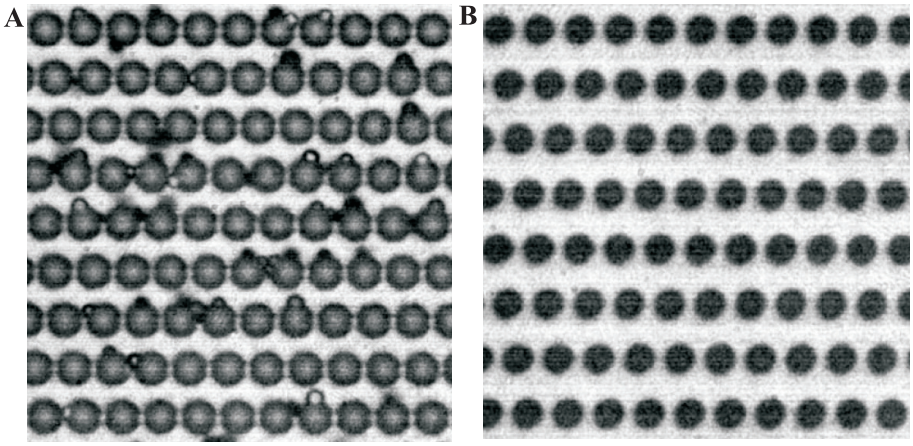

Figure 5.5: Particles of suspension D (see table 5.3) stuck in device design $N = 4, D_x/D_y = 1.5$ A) $R_o/D_y = 0.5$ and B) a device free of adhered particles $R_o/D_y = 0.2$.

particle motion occurs, namely $2d_{f,1}/D_y$ and $2d_{f,c}/D_y$. Their values are directly taken from table 5.2. The data points in the graphs represent the averaged, dimensionless migration angles θ/θ_{max}, as a function of the average, dimensionless particle diameter d_p/D_y. The error bars for the particle diameter are based on the $D(0.1)/D_y$ and $D(0.9)/D_y$ values from table 5.3. The error bars for the migration angle are based on the standard deviation of the migration angles, as indicated in table 5.4.

Overall, the experimental results agree with the newly formulated classification rules. For all particles smaller than the first lane width $r_p < d_{f,1}$, the average migration

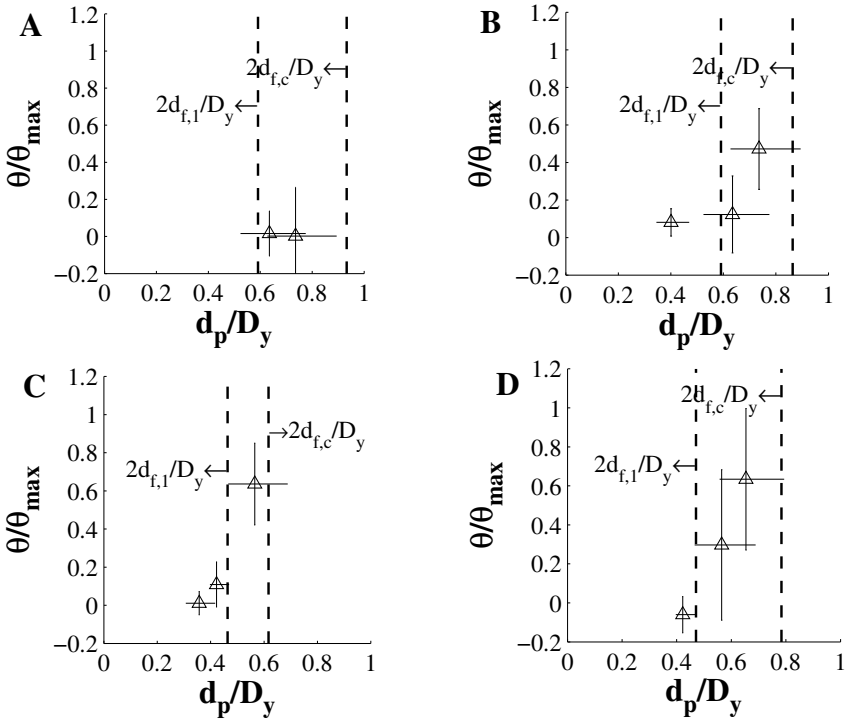

Figure 5.6: Comparison of experimental results with new classification rules for ratchet designs I to IV, which are shown in that order in graphs A to D. Dashed lines indicate the numerically obtained length scales $2d_{f,1}/D_y$, and $2d_{f,c}/D_y$, which describe the transition from zigzag to mixed motion, and the transition from mixed to displacement motion. Data points indicate average migration angle $\tilde{\theta} = \theta/\theta_{max}$ versus average particle diameter d_p/D_y.

is about zero as expected. For larger particles, we find migration angles larger than zero, but smaller than unity - indicating that they are showing mixed motion as expected from the classification rules. There is one data point, which does not adhere to the classification rule, and in this experiment severe particle adhesion occurred, as shown in figure 5.5. Therefore it seems legitimate to exclude this data point, and we may fairly conclude that our experiments confirm the new classification rules, which are based on the length scales, $d_{f,1}$ and $d_{f,c}$, obtained from the 2D flow simulations and the 3D particle flow simulations respectively.

To investigate whether there is a correlation between migration angle and particle size, we have re-plotted experimental data points of designs II to IV (shown in figure 5.6B-D) in a single graph 5.7, displaying the effective particle size $\tilde{d}_p = (d_p - 2d_{f,1})/(2d_{f,c} - 2d_{f,1})$ versus the dimensionless migration angle $\tilde{\theta} = \theta/\theta_{max}$. This

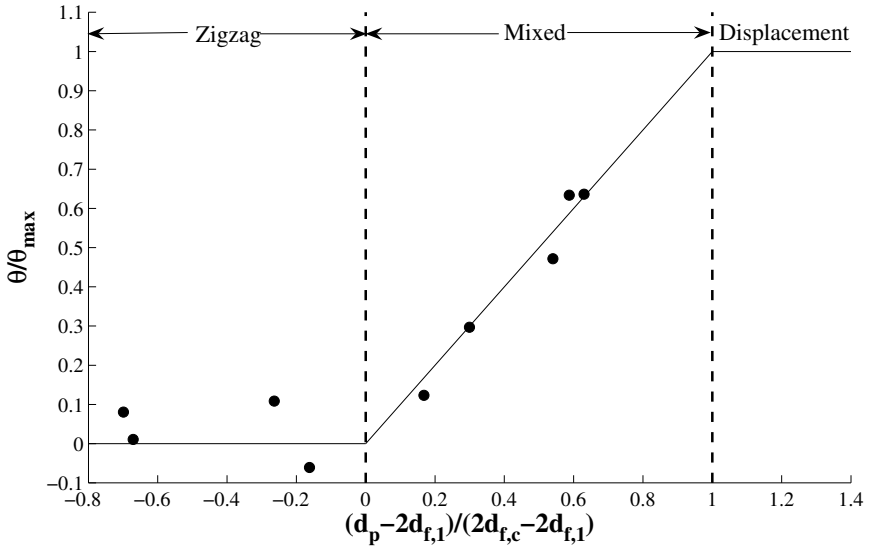

Figure 5.7: An overview of migration angles obtained from the experiments compared with the length scales $d_{f,1}$ and $d_{f,c}$ obtained from 2D and 3D simulations. The solid line is the expected migration angle; the dashed lines indicate the transition points to mixed, and displacement motion.

graph shows that $\tilde{d}_p$ versus $\tilde{\theta}$ follows a master curve. In the range of mixed motion, $0 \leq \tilde{d}_p \leq 1$, the master curve follows the straight line $\tilde{\theta} = \tilde{d}_p$. If $\tilde{d}_p < 0$ the particles are showing zigzag motion and $\tilde{\theta} = 0$, and if $\tilde{d}_p > 1$ the particles are showing displacement motion, and consequently $\tilde{\theta} = 1$.

5.4 Conclusions

In this paper, we derives new classification rules for fractionation of particles in deterministic DLD ratchets, based on numerical simulation, which are experimentally validated. The classification rules are based on 2 length scales: the first flow lane width $d_{f,1}$, and the critical length scale $d_{f,c}$, which denote the transition from zigzag to mixed motion, and from mixed to displacement motion.

The width of the first flow lane $d_{f,1}$ can be determined by simple 2D flow simulations, while the critical length scale $d_{f,c}$ needed to be determined via 3D particle flow simulations. In case of dominating hydrodynamic interactions, the experimental results indicate that the migration angle θ can be determined via a set of simple rules. If $d_p < 2d_{f,1}$ then the migration angle is zero, $\theta = 0$, and if $d_p \geq 2d_{f,c}$ the migration angle

is maximal, with the actual value depending on the ratchet design. For mixed motion, the migration angle follows the simple rule $\theta/\theta_{max} = (d_p - 2d_{f,1})/(2d_{f,c} - 2d_{f,1})$.

The trajectories of particles showing mixed motion are irregular in the experiments but the simulations show regular behavior. The numerical trajectories indicate that particles with mixed motion closely approach the stagnation points in front of the obstacles, which makes them prone to Brownian motion and colloidal forces, which in the experiments was shown to lead to adherence, and this may influence the trajectory that is followed. This point clearly deserves more attention in future investigations.

References

[1] L.R. Huang, E.C. Cox, R.H. Austin and J.C. Sturm. Continuous particle separation through deterministic lateral displacement. *Science*, **304**: 987-990 (2004).

[2] D.W. Inglis, J.A. Davis, R.H. Austin and J.C. Sturm. Critical particle size for fractionation by deterministic lateral displacement. *Lab Chip*, **6**: 655-658 (2006).

[3] J.A. Davis, D.W. Inglis, K.J. Morton, D.A. Lawrence, L.R. Huang, S.Y. Chou, J.C. Sturm and R.H. Austin. Deterministic hydrodynamics: Taking blood apart. *PNAS*, **130**:14779-14784 (2006).

[4] K. Loutherback, J. Puchalla, R.H. Austin and J.C. Sturm. Deterministic microfluidic ratchet. *Phys. Rev. Lett.*, **102**:045301 (2009).

[5] T. Kulrattanarak, R.G.M. van der Sman, C.G.P.H. Schroën and R.M. Boom. Classification and evaluation of microfluidic devices for continuous suspension fractionation. *Adv. Colloid Interface Sci.*, **142**:53-66 (2008).

[6] J. Kromkamp, F. Faber, C.G.P.H. Schroën and R.M. Boom. Effects of particle size segregation on crossflow microfiltration performance: control mechanism for concentration polarisation and particle fractionation. *J. Membr. Sci.*, **268**: 189-197 (2006).

[7] G. Brans, C.G.P.H. Schroën, R.G.M. van der Sman and R.M. Boom. Transmission and fractionation of micro-sized particle suspensions. *J. Membr. Sci.*, **290**: 230-240 (2007).

[8] T. Kulrattanarak, R.G.M van der Sman, C.G.P.H. Schroën, and R.M. Boom. Refinement of classification rules for deterministic ratchets through 2-D flow field simulation. *Chapter 3*

[9] T. Kulrattanarak, Y.S. Lubbersen, R.G.M van der Sman, C.G.P.H. Schroën,

H.T.M. Pham, P.M. Sarro and R.M. Boom. Image analysis of particle trajectories in deterministic ratchets including comparison with computed classification rules. *Chapter 4*

[10] J.C.T. Eijkel and A. van den Berg. Nanotechnology for membranes, filters and sieves. *Lab Chip*, **6**:19-23 (2006).

[11] S.Y. Chen and G.D. Doolen. Lattice Boltzmann method for fluid flows. *Ann Rev Fluid Mech.*, **3**:329-364 (1998).

[12] Y.H. Qian, D. d'Humieres, P. Lallemand. Lattice BGK model for Navier-Stokes equations. *Europhys Letters.*, **17**:479-484 (1992).

[13] Ladd AJC, Verberg R. Lattice-Boltzmann simulations of particle-fluid suspensions. *J Stat Phys.*, **104**: 1191-1251 (2001).

[14] Inamuro T, Yoshino M, Ogino F. A non-slip boundary condition for lattice Boltzmann simulations. *Phys. Fluids*, **7**(12):2928-2930 (1995).

[15] Sangani AS, Acrivos A. Slow flow past periodic arrays of cylinders with application to heat transfer. *Int J Multiphase Flow.*, **8**(3):193-206 (1982).

[16] Z. Adamczyk, M. Adamczyk and T.G.M. van de Ven. Resistance coefficient of a solid sphere approaching plane and curved boundaries. *J. Colloid Interface Sci.*, **96**, (1):204-213 (1983).

[17] R.G.M. van der Sman. Simulations of confined suspension flow at multiple length scales *Soft Matter*, **5**: 4376 (2009).

[18] R.G.M. van der Sman, Confined suspension flow with MRT Lattice Boltzmann schemes. *Comput. Phys. Commun.*, 2009 submitted.

[19] D. d'Humieres, I. Ginzburg, M. Krafczyk, P. Lallemand and L. Luo. Multiple-relaxation-time lattice Boltzmann models in three dimensions. *Phil. Trans. R. Soc. Lond. A*, **360**: 437451 (2002)

[20] B. Chun and A. J. C. Ladd, Interpolated boundary condition for lattice Boltzmann simulations of flows in narrow gaps. *Phys. Rev. E*, **75**(6): 066705 (2007).

[21] R.C. Ball and J.R. Melrose. Lubrication breakdown in hydrodynamic simulations of concentrated colloids. *Adv. Colloid Interface Sci.*, **59**: 19-30 (1995).

[22] J. Kromkamp, D. van den Ende, D. Kandhai, R.G.M. van der Sman and R.M. Boom. Lattice Boltzmann simulation of 2D and 3D non-Brownian suspensions in Couette flow. *Chem. Eng. Sci.*, **61**(2):858-873 (2006).

[23] I. Ginzburg. Equilibrium-type and link-type lattice Boltzmann models for generic advection and anisotropic-dispersion equation. *Adv Water Resour.*, **28**: 1171-1195

(2005).

[24] A.J.C. Ladd. Numerical simulations of particulate suspensions via a discretized Boltzmann equation Part I. Theoretical foundation. *J. Fluid Mech.*, **271**:285-309 (1994).

[25] J. Frechette and G. Drazer. Directional locking and deterministic separation. *J. Fluid Mech.*, **627**: 379-401 (2009).

[26] M.L.J. Steegmans, A Warmerdam, C.G.P.H. Schron and R.M. Boom. Dynamic Interfacial Tension Measurements with Microfluidic Y-Junctions *Langmuir*, **25** (17): 97519758 (2009)

[27] H.T.M. Pham, T. Kulrattanarak, R.G.M. van der Sman, C.G.P.H. Schroën, R.M. Boom and P.M. Sarro. Deterministic ratchets for particle separation fabricated with Si MEMS Technology. *Proceedings of the Eurosensors XXIII conference.*, Procedia Chemistry, **1**:345-348 (2009).

Chapter 6

General discussion

In the previous chapters, various classification rules for deterministic (DLD) ratchets have been derived via numerical investigation based on 2D, and 3D simulations and / in combination with experimental observations. Further, in chapter 3 relations are given for the evaluation of key performance indicators of ratchets, which are relevant to food applications such as compatibility with high volume throughput processing and compactness of the ratchets. However, in these rules the newly found mixed motion behavior is not taken into account. Because mixed motion occurs especially in compact devices relevant to food applications, the design rules need to be re-evaluated. This we will do in this concluding chapter. But first, we will give a brief summary of the development of our insights in the classification rules, and we will finalize with practical recommendations and an outlook on the future research of deterministic ratchets.

6.1 Development of classification rules

Like many other types of microfluidic devices, fractionation in deterministic ratchets is based on the flow line sieving principle [1, 2]. The flow field in the microchannel is divided into so-called flow lanes, which are bordered by dividing stream lines; small particles remain in their flow lanes, and larger particles have hydrodynamic interaction with obstacles and walls, which displaces them. Based on this difference in particle behavior, fractionation can be achieved, and for this, classification rules that state whether particle remain in their flow lane or whether they will be displaced are needed.

In deterministic (DLD) ratchets, flow line sieving is imposed by a regular array of

obstacles inside a microchannel, with each row of obstacles slightly laterally displaced with respect to the previous row. The inventors of DLD ratchets, Austin, Sturm and co-workers [3, 4], have assumed a Poiseuille flow profile in the pore space between obstacles, and equal volumetric flow rate for each flow lane. Based on that, they have formulated an analytical expression for the smallest particle that will show displacement motion (even smaller particles will thus show zigzag motion), and from this they concluded that if the particle is larger than the largest flow lane it will be displaced.

Since flow lane width has been indicated as an essential parameter, we have started our investigation via numerical investigation of the flow field inside the ratchet to determine the widths of the flow lanes. We have found that contrary to what is assumed by Austin and co-workers, mostly the flow field inside the pore space is asymmetric, and consequently, also the flow lane distribution. From the simulations, we have concluded in order to describe particle behavior, two critical length scales are needed, being the width of the first and the last flow lane, $d_{f,1}$ and $d_{f,N}$, and subsequent experiments seem to confirm that.

However, the observed particles have also showed unexpected behavior, so-called mixed motion, which occurs if the particle diameter is in between the two critical length scales, $2d_{f,1} < d_p < 2d_{f,N}$. In order to investigate this further, we have performed full 3D-simulations, which explicitly solve the motion of a single particle, flowing through a periodic cell of a ratchet, and having designs aimed at observing mixed motion. From this it can be concluded that the critical length scale determining the transition between zigzag and mixed motion is indeed $d_{f,1}$. The critical length scale determining the transition between mixed and displacement motion is however not equal to $d_{f,N}$, and might even be uncorrelated to it. This second critical length scale, $d_{f,c}$ is even larger than $d_{f,N}$. As mentioned, mixed motion occurs for particles having a radius in between these length scales, $d_{f,1}$ and $d_{f,c}$, and interestingly, their migration angle is linearly proportional with the ratio $(d_p - 2d_{f,1})/(2d_{f,c} - 2d_{f,1})$. We have not yet been able to find a simple analytical expression; for this, computationally intensive 3D-simulations are needed (which implies approximately one week computing time on parallel computers).

Table 6.1: Critical length scales $2d_{f,1}/D_y$ and $2d_{f,N}/D_y$, obtained from 2D simulations, and $2d_{f,c}/D_y$, obtained from 3D simulations for compact devices characterized by the dimensionless design parameters in the first column, together with the estimated yield based on the 3D critical length scales.

N	D_x/D_y	R_o/D_y	$2d_{f,1}/D_y$	$2d_{f,N}/D_y$	$2d_{f,c}/D_y$	Yield $[m^3/(m^3 \cdot day)]$
3	1.0	0.2	0.69	0.84	0.90	50.89
	1.5	0.2	0.72	0.78	0.88	39.40
4	1.0	0.2	0.55	0.77	0.82	23.14
	1.5	0.2	0.59	0.66	0.86	16.46

6.2 Design rules and implications of mixed motion

The key performance indicators of ratchets for food applications are their yield (productivity), compactness, and selectivity (as presented in chapter 3 based on 2D simulation results). In this section, we present full 3D analysis of ratchets with optimal design for food applications for which typically $D_x/D_y \approx 1$, the obstacles are slender with $R_o/D_y \leq 0.2$, and small number of obstacle rows inside one periodic cell of the obstacle array ($N = 3 - 4$). The critical length scale $d_{f,c}$ is determined, and subsequently we have re-evaluated the yield of these devices. Results are shown in table 6.1, which gives the dimensionless lane widths $2d_{f,1}/D_y$ and $2d_{f,N}/D_y$ obtained from 2D analysis, together with the critical length scale $2d_{f,c}/D_y$ obtained from 3D analysis. We find that for these compact devices the critical length scale $d_{f,c}$ is only fractionally larger than our previous estimation $d_{f,N}$, and consequently the yield as calculated using the relations from chapter 3 is not significantly different. The initial design rules that we have derived for food applications still hold, and computationally less intensive 2D simulations can be used for estimating both critical length scales.

The deterministic ratchet devices as originally investigated by the inventors of ratchets, have only a single critical length scale - due to a symmetric flow lane distribution. Consequently, these devices have a very strong selectivity, as particles will be displaced or not. In a ratchet device having two and equally sized outlets, as evaluated for their performance in chapter 3, which is fed with a binary suspension having particles either smaller or larger than the critical length scale, the feed will split up in two streams containing only one type of particles.

The existence of mixed motion breaks down this strong selectivity. In ratchet

devices having two outlets fed with a (slightly) polydisperse suspension, particles larger than $d_{f,1}$ but smaller than $d_{f,c}$ (thus showing mixed motion) can end up in both outlets. In case of mixed motion, selectivity can be improved via increase of the number of outlets. Such a ratchet device is shown in figure 6.1, where the device has three equally sized outlets - all with equal flow rates. In addition typical trajectories of particles are indicated. It is clear that zigzagging particles will always end up in the lower outlet, while only particles showing displacement motion will end up in the upper outlet. Particles exhibiting mixed motion will either end up in the first or second outlet.

Hence, the feed is fractionated into three different streams, based on the length scales $d_{f,1}$ and $d_{f,c}$. Compared to a device with two outlets, the devices of three outlets will occupy more space, and the permeate will be more diluted, because one needs twice the amount of carrier fluid as in a two outlet device.

The existence of mixed motion may even open up the possibility to fractionate particles in a single step, if the size distribution is more or less between the critical length scales $d_{f,1}$ and $d_{f,c}$. Via mixed motion one obtains a continuous spectrum of migration angles, $0 \leq \theta \leq \theta_{max}$, which can be split in multiple streams, if one applies multiple outlets and two inlets for the feed suspension and the carrier fluid.

In figure 6.1, we have also sketched an example of possible trajectories: a displacing particle, $d_p \geq 2d_{f,c}$, will traverse and end up in the most upper outlet, while a zigzagging particle, $d_p < 2d_{f,1}$ will move with net zero displacement towards the lowest outlet at anywhere of the initial positions. For mixed particles $2d_{f,1} < d_p < 2d_{f,c}$, as they have migration angles of $0 < \theta < \theta_{max}$, therefore depending on the initial positions and the migration angles, some part will end up at the middle outlet, but some part will end up at the lowest outlet.

We can also imagine a design that does not require any carrier fluid, and since dilution is prevented this is beneficial in a fractionation process (see figure 6.2). In the lower outlet, there will be a stream with only small particles $d_p < 2d_{f,c}$, as the large particles $d_p \geq 2d_{f,c}$ always displace to the upper part of the obstacle field. The upper outlet will have a stream that is highly concentrated in large particles, but will also contain small particles.

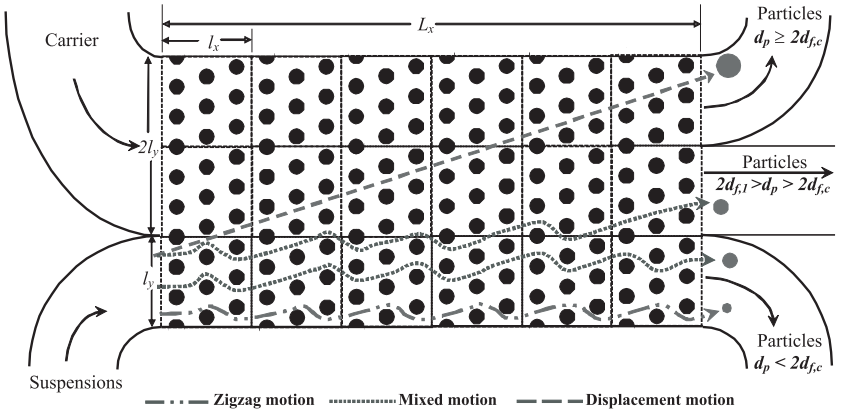

Figure 6.1: Sketch of a minimally sized ratchet device with $N = 3$, feed suspensions containing particles that exhibit mixed motion, including examples of particle trajectories.

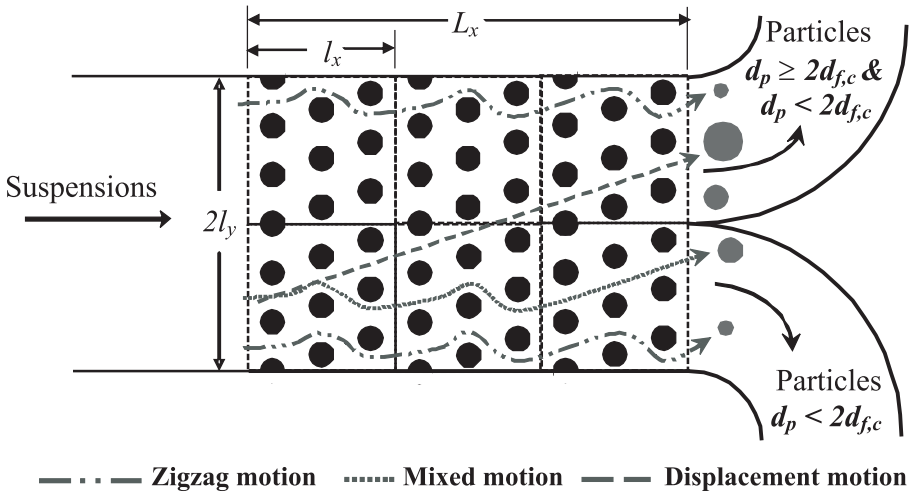

Figure 6.2: Sketch of a minimally sized ratchet device with $N = 3$, that does not require carrier fluid including examples of particle trajectories.

6.3 Applications and outlook

Although deterministic (DLD) ratchets are investigated mainly for use in biological applications, e.g. for fractionation cells and DNA [3, 5–7], they also receive interest from a fundamental point of view [8, 9]. The next step will be to use these devices in practice, and one hurdle that still needs to be taken is to make them suitable for large-scale applications and for this, economic aspects are of essence. A relevant quantitative survey on the economics of scale was reported in ref. [2, 10], which considered large scale application of DLD ratchets for dewatering of algae. This survey is quite positive

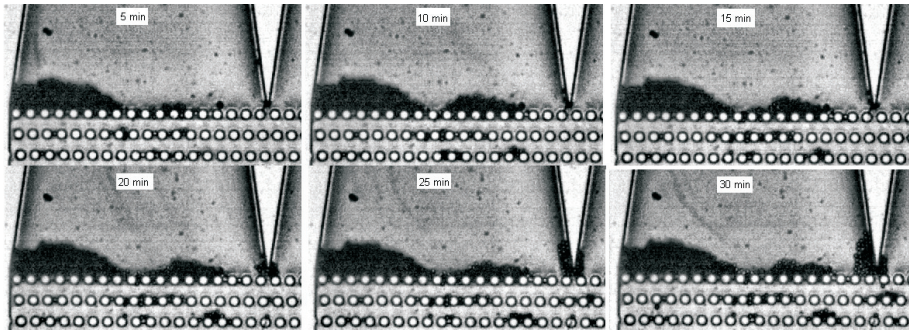

Figure 6.3: Particle accumulation above the first row of the ratchet for suspensions with a concentration of 1.00 $V/V\%$ after 5, 10,15, 20, 25 and 30 minutes.

about large scale application of ratchets, and we think this would also apply for food applications.

Our research has shown that there are practical, but manageable hurdles that still need to be taken. In most of the experiments reported in the thesis, the feed suspension had a particle volume fraction of 0.05%. We have also performed tests with higher volume fractions, namely 0.5 and 1.0%, and we have found that aggregated particles got stuck on the first obstacle row in the device (see figure 6.3), while initially still allowing some particles to pass. After 30 minutes, there are less and less particles entering to the ratchet. Most probably, aggregation was promoted by the confinement in the tubing; therefore, we suggest to use tubing that has an inner diameter larger than 30 times the particle diameter. Even though these problems are not intrinsic to the ratchets, they are a general bottleneck in microfluidic devices: the interfacing with the outside macroscopic world has not yet been solved satisfactorily.

Real food suspensions are even more concentrated than the 1% volume percent suspension; e.g. in milk, the solids have a (weight) fraction of around 13%. At these concentrations, we anticipate that there is a significant incidence of particle-particle interactions, and these hydrodynamic interactions may push the particles from their streamlines. Since the principle of the fractionation with ratchets is based on the hydrodynamic interaction between particle and obstacle, this may impart the process. Further, concentrated particles may accumulate in ratchets due to a difference in residence time between fluid and particles. To solve this, back pulsing might be applied, as used in membrane technology, which may even be beneficial for the separation [11–13], but the particle trajectories are also expected to be disturbed. Whether this is beneficial or not will have to follow from future research.

Furthermore, the (stability) of the surface properties of the obstacles and bounding walls is an important issue for any microfluidic device, and thus also for ratchet devices. In one experiment, we have observed significant particle adhesion to the obstacles, which indicates that colloidal forces between particles and obstacle may be important. One option to avoid this is surface treatment. In this work, we have adsorbed Synperonic PEF 108 to the surface, which reduces the interaction by colloidal forces, and facilitates the removal of air bubbles during start-up of the experiments. If modification that is more permanent is required, the covalent attachment methods described by Arafat and co-workers, and Rosso and co-workers [14–16] , would be interesting alternatives.

Most of the above mentioned hurdles are engineering problems, which can be solved - but will take time. We see deterministic ratchet as a promising technology, and in this, we are not alone given the increasing number of papers reporting on this technology. One interesting development for example, is the development of ratchets which use an extra external force (e.g. DEP), which opens up the possibility to fractionate particles based on size and dielectric properties [17], therewith allowing further fractionation of equally sized particles. This is also relevant for food; for example, milk has bacteria and fat globules of comparable size, but different dielectric properties therewith possibly opening a route to cold sterilization with ratchet technology.

References

[1] J.C.T. Eijkel and A. van den Berg. Nanotechnology for membranes, filters and sieves. *Lab Chip*, **6** (2006) 19-23.

[2] T. Kulrattanarak, R.G.M. van der Sman, C.G.P.H. Schroën and R.M. Boom. Classification and evaluation of microfluidic devices for continuous suspension fraction. *Adv. Colloid Interface Sci.*, **142** (2008) 53-66.

[3] L.R. Huang, E.C. Cox, R.H. Austin and J.C. Sturm. Continuous particle separation through deterministic lateral displacement. *Science*, **304** (2004) 987-990.

[4] D.W. Inglis, J.A. Davis, R.H. Austin and J.C. Sturm. Critical particle size for fractionation by deterministic lateral displacement. *Lab Chip* **6** (2006) 655-658.

[5] J.A. Davis, D.W. Inglis, K.J. Morton, D.A. Lawrence, L.R.Huang, S.Y. Chow, J.C. Sturm and R.H. Austin. Deterministic hydrodynamics: Taking blood apart. *PNAS*, **130** (2006) 14779-14784.

[6] D.W. Inglis, J.A. Davis, T.J. Zieziulewicz, D.A. Lawrence, R.H. Austin and J.C. Sturm. Determining blood cell size using microfluidic hydrodynamics. *J. Immunol. Methods*, **329** (2008) 151-156.

[7] J.V. Green, M. Radisic and S.K. Murthy. Deterministic Lateral Displacement as a means to Enrich Large Cells for Tissue Engineering. *Anal. Chem.*, **81** (2009) 9178-9182.

[8] J. Frechette and G. Drazer. Directional locking and deterministic separation. *J. Fluid Mech.*, **627** (2009) 379-401.

[9] K. Loutherback, J. Puchalla, R.H. Austin and J.C. Sturm. Deterministic microfluidic ratchet. *Phy. Rev. Lett.*, **102** (2009) 045301.

[10] J.T. Bargiel. Commercialization of lateral displacement array for dewatering of microalgae. *Master thesis*, Department of Physics, Case Western Reserve University.

[11] A. Guerra, G.Jonsson, A. Rasmussen, E. Waagner Nielsen and D. Edelsten. Low cross flow velocity microfiltration of skim milk for removal of bacterial spores. *Int. Dairy Journal*, **7** (1997) 849-861.

[12] W.D. Mores and R.H. Davis. Yeast-fouling effects in cross-flow microfiltration with periodic reverse filtration. *Industrial Eng. Chem. Research*, **42** (2003) 130-139.

[13] S. Redkar, V. Kuberkar and R.H.Davis. Modeling of concentration polarization and depolarization with high-frequency backpulsing. *J. Membrane Sci.*, **121** (1996) 229-242.

[14] A. Arafat, K. Schron, L. de Smet, E. Sudhlter, H. Zuilhof. Tailor-made Functionalization of Silicon Nitride Surfaces. *J. Am. Chem. Soc.*, **126** (2004) 8600-8601.

[15] A. Arafat, M. Giesbers, M. Rosso, E.J.R. Sudhlter, C.G.P.H. Schron, R.G. White, et al. Covalent Biofunctionalization of Silicon Nitride Surfaces. *Langmuir*, **23** (2007) 6233-6244.

[16] M. Rosso, M. Giesbers, A. Arafat, K. Schron, H. Zuilhof.. Covalently attached Organic Monolayers on SiC and SixN4 Surfaces: Formation using UV Light at Room Temperature. *Langmuir*, **25** (4) (2009) 2172-2180.

[17] J.P. Beech, P. Jonsson and J.O. Tegenfeldt. Tipping the balance of deterministic lateral displacement devices using dielectrophoresis. *Lab Chip*, **9** (2009) 2698-2706.

Summary

Driven by the current insights in sustainability and technological development in biorefining natural renewable resources, the food industry has taken an interest in fractionation of agrofood materials, like milk and cereal crops. The purpose of fractionation is to split the raw material in several functional ingredients. For example, milk can be split in fractions containing milk fat, casein micelles, and whey proteins.

Traditionally, separation processes in food industry are mainly aimed at separating fluid from a suspension stream. Frequently membrane technology is used this type of separation; membranes seem an obvious choice because they are able to sieve components during mild fractionation of many foods, which are suspensions by nature, like milk, or are suspended in liquid during processing (such as starch granule suspensions). However, membrane separation is hindered by fouling of the pores by the food ingredients and accumulation of these components in front of the pore, which makes fractionation with membranes more challenging than plain separation of fluid and solids. That is why we have investigated the possibilities of alternative technologies such as microfluidic devices, and evaluated them under conditions required for food applications.

Microfluidic devices are currently investigated for fractionation in biological applications, like sorting of DNA or cells. Due to the large degree of freedom in design, these devices are very suited for innovative fractionation technologies. First, we have evaluated various designs available in literature in chapter 2, which concludes that so-called deterministic ratchets are the most promising technology for fractionation of food suspensions. This conclusion is based on the high yield, compactness of equipment, and high selectivity that can be reached with such devices. In chapters 3 6, we report on detailed investigations on deterministic ratchets through 2D simulation (chapter 3), image analysis in comparison with simulation results (chapter 4), and full 3D simulations in combination with the previously mentioned methods (chapter 5).

In the last chapter, our findings are summarized in classification and design rules, and an outlook for future developments is given.

Deterministic ratchets are microchannels, containing a regularly spaced array of obstacles, through which the particle suspension flows. The essential property of these ratchets is that each obstacle row is displaced slightly laterally with respect to the previous row. Small particles follow the streamlines of the fluid, and zigzag around the obstacles, while particles larger than a certain critical size bump into the obstacles, and are consequently displaced from their streamline. The larger particles will continuously be displaced in a direction in which the obstacles are placed, and have a certain angle with the flow direction. The small particles are moving in the direction of the liquid flow, which implies under an angle of zero degrees. Via the difference in migration angle of the zigzag and displacement motion, particles can be fractionated, and collected from different outlets.

An important property of deterministic ratchets is the size of the particles relative to the width of the so-called flow lane, which determines whether it will show zigzag motion or not. This we have investigated intensively in chapter 3 by means of 2-D flow field simulation. The critical particle size is related to the width of the flow lanes, within which the zigzagging particles will move, and we have determined the flow lane widths for various designs. The distribution of the flow lane width is found to depend strongly on the design of the ratchets. For a limited number of designs the original hypothesis of the inventors of the deterministic ratchets holds, and the flow lanes are symmetrically distributed over the space in between obstacles in one single row. In general, ratchets have an asymmetric flow lane distribution, and typically, ratchet designs suitable for food applications show a strong asymmetric flow lane distribution.

An asymmetric flow lane distribution implies that there is not one critical flow lane width but two that determine the type of motion of particles inside the ratchets. As a first approach we have taken these as the first and last (and largest) flow lane width, $d_{f,1}$ and $d_{f,N}$. Consequently, particles are expected to show alternative motions that are in between zigzag and displacement motion. Its existence has become evident in the experiments described in chapter 4, and we have named it *mixed* motion. The mixed motion is irregular, in contrast to the zigzag and displacement motion, and has a migration angle which is intermediate between the angles corresponding to zigzag and displacement motion, $0 < \theta < \theta_{max}$. The particles moving in the ratchets we have tracked by high speed recording, and the migration angle were quantified through

tailor-made image analysis. As expected, the transitions between the different types of particle motion seem to occur on the basis of the critical length scales, $d_{f,1}$ and $d_{f,N}$. However, this conclusion can not be stated with high certainty because of the large experimental error due to the wide particle size distribution of the used suspensions.

Because the ratchets used in chapter 4 has not been specifically designed to investigate various particle behaviors, we have designed new ratchets based on the critical length scales, $d_{f,1}$ and $d_{f,N}$, via 2D flow simulations, in order to allow detailed investigation. Although these critical length scales do not take all aspects that play a role during particle movement in a ratchet into account, we have stated that they can be used as an initial guideline for ratchet designs. Next, we have performed detailed and computationally intensive, 3D simulations, that include the particles. These 3D simulations are performed to check the validity of the classification rules, derived from the 2D simulations, that only include fluid flow. The simulation results show that the transition between zigzag and mixed motion occurs indeed at the critical length scale, $d_{f,1}$, being the width of the first flow lane. However, the length scale determining the occurrence of displacement motion is larger than the last lane width, $d_{f,N}$, and might even be uncorrelated with it. We have concluded that this second critical length scale, $d_{f,c}$, can only be determined via 3D simulations. The thus obtained classification rules are investigated experimentally and we have been able to correlate the migration angle of many observed particles exhibiting mixed motion, to the critical length scales. This makes us confident, that we now have identified the relevant critical length scales in deterministic ratchets.

In the concluding chapter, we discuss the approach that we chose to ultimately derive the classification rules, and discuss the implications of the corrected length scales on the key performance indicators of ratchets, that are relevant to food applications. We find that obtaining the correct critical length scales requires computationally intensive 3D simulations. Specifically for compact ratchet designs, which are relevant for food application, the critical lane width $d_{f,c}$ is not much different from $d_{f,N}$, obtained via 2D flow simulations - and 2D simulation may thus offer a more time-efficient way of estimating $d_{f,c}$. Further, we have discussed the existence of mixed motion in terms of selectivity during fractionation for polydisperse suspensions, and have found that the yield, compactness, and selectivity, all decrease, but at the same time it also opens possibilities for fractionation in multiple streams in one step.

Samenvatting

Gedreven door de huidige inzichten op het gebied van duurzaamheid en technologische ontwikkelingen op het gebied van bioraffinage van natuurlijke grondstoffen, is er grote interesse ontstaan in de voedingsindustrie voor fractionering van agrofood grondstoffen, zoals melk en graan. Het doel van fractioneren is het scheiden van agrofood grondstoffen in meerdere functionele ingrediënten. Melk kan bijvoorbeeld gescheiden worden in fracties die melkvet, casene micellen, en wei-eiwitten bevatten.

Traditioneel zijn scheidingsprocessen in de voedingsindustrie vooral gericht op het scheiden van vloeistof van vaste deeltjes. Vaak wordt hiervoor membraantechnologie ingezet; membranen lijken een voor de hand liggende keuze omdat ze in staat zijn om componenten uit te zeven tijdens milde fractionering van veel levensmiddelen die van nature suspensies zijn, zoals melk, of die in suspensie gebracht worden tijdens de verwerking, zoals zetmeel suspensies. Echter, membraanscheiding wordt bemoeilijkt door vervuiling van de porin van het membraan door de voedselingrediënten en accumulatie van deze componenten voor de ingang van de porie, en dit maakt scheiding in verschillende fracties nog lastiger dan het traditionele filtreren van vaste stof uit vloeistof. Om deze reden hebben we de mogelijkheden van alternatieve technologien zoals microtechnologie onderzocht, en gevalueerd voor omstandigheden die relevant zijn voor toepassing in levensmiddelen.

Microtechnologie wordt intensief onderzocht voor fractionering in biologische systemen zoals het sorteren van DNA of cellen. Door de grote vrijheid in vormgeving van microtechnologische apparaten, zijn ze zeer geschikt voor innovatieve fractioneringstechnologieën. Eerst hebben we de verschillende ontwerpen die beschikbaar zijn in de literatuur gevalueerd in hoofdstuk 2, waaruit we konden concluderen dat de zogenaamde deterministische ratchets het meest veelbelovend zijn voor fractionering van levensmiddelencomponenten. In hoofdstukken 3 tot 6 rapporteren we in detail over het onderzoek aan deterministische ratchets via 2D simulatie (hoofdstuk 3), beeld-

analyse in relatie tot simulatieresultaten (hoofdstuk 4), en volledige 3D simulatie in combinatie met alle eerder genoemde methoden. In het laatste hoofdstuk worden onze bevindingen samengevat in classificatie- en ontwerpregels, en geven we een vooruitblik op toekomstige ontwikkelingen.

Deterministische ratchets zijn stromingskanalen, waarin een veld van pilaren is geplaatst, en waardoor de deeltjessuspensies stromen. De essentie van deze ratchets is dat de rijen pilaren een fractie verschoven zijn ten opzichte van de vorige rij. De kleinste deeltjes zullen de stroming volgen en als het ware om de pilaren heen zigzaggen, terwijl deeltjes die boven een bepaalde grootte zijn tegen de pilaren botsen en van hun stroomlijn afwijken. De grotere deeltjes worden continu uit hun stroomlijn geduwd, onder een bepaalde hoek met de stromingsrichting. De kleine deeltjes bewegen in de stromingsrichting en dat houdt in dat ze onder een hoek van nul graden bewegen. Door het verschil in migratiehoek tussen zigzag- en verplaatsingsbeweging kunnen deeltjes worden gefractioneerd, en opgevangen uit verschillende uitgangen.

Een belangrijke eigenschap van de determistische ratchets wordt bepaald door de deeltjesgrootte ten opzichte van de breedte van de stroomvelden (flow lanes), en dit bepaalt of een deeltje zigzagbeweging zal vertonen of niet. Dit hebben we uitvoerig onderzocht in hoofdstuk 3 met behulp van twee-dimensionale stromingsberekeningen. De kritische deeltjesgrootte is gerelateerd aan de zogenaamde breedte van de stromvingsvelden, waarbinnen de kleinste deeltjes zich bewegen, en we hebben deze breedtes berekend voor verschillende ontwerpen van ratchets. We hebben gevonden dat de verdeling van de breedtes van de stroomvelden sterk afhankelijk is van het ontwerp. Voor een gelimiteerd aantal ontwerpen gaat de veronderstelling van de uitvinders van de deterministische ratchet op, en dat houdt in dat de stroomvelden symmetrisch verdeeld zijn tussen de pilaren in een rij. Echter, de meeste ratchets hebben een asymmetrische verdeling van stroomvelden en ratchet-ontwerpen die interessant zijn voor fractionering van voedingssuspensies hebben een sterk asymmetrische verdeling.

Een asymmetrische verdeling van stroomvelden impliceert dat er niet één maar twee kritische lengteschalen zijn die de beweging van deeltjes in ratchets zullen bepalen. In eerste instantie hebben we hiervoor de breedte van het eerste en het grootste stroomveld genomen, $d_{f,1}$ and $d_{f,N}$. Daarom kan verwacht worden dat deeltjes nog een andere beweging zullen vertonen die tussen zigzag- en verplaatsingsbeweging in ligt; het bestaan hiervan is aangetoond in de experimenten die in hoofdstuk 4 beschreven zijn en we noemen dit gemengde beweging. In tegenstelling tot de zigzag- en de

verplaatsingsbewegingen is deze gemengde beweging onregelmatig, en wordt gekenmerkt door een verplaatsingshoek die het midden houdt tussen die van de zigzag- en de verplaatsingsbeweging $0 < \theta < \theta_{max}$. De deeltjes die door de ratchets bewegen worden opgenomen met een hogesnelheidscamera, en de migratiehoek van de deeltjes wordt bepaald met een specifiek voor dit doel ontwikkelde beeldverwerkingsprocedure. Zoals verwacht lijkt de overgang tussen de verschillende bewegingstypes plaats te vinden op basis van de kritische lengteschalen. De afhankelijkheid van de verschillende typen deeltjesbewegingen, komt redelijk overeen met de kritische lengteschalen, $d_{f,1}$ and $d_{f,N}$. Deze conclusie kunnen we echter niet met grote zekerheid stellen omdat er een grote experimentele onzekerheid is als gevolg van de deeltjesgrootteverdeling van de gebruikte suspensies.

Omdat de ratchets uit hoofdstuk 4 niet specifiek zijn ontworpen om de verschillende bewegingstypen te onderzoeken, hebben we nieuwe ratchets ontworpen gebaseerd op de kritische lengteschalen, $d_{f,1}$ and $d_{f,N}$, verkregen uit 2D simulaties. Omdat deze lengteschalen niet alle aspecten meenemen die een rol spelen bij deeltjesbeweging in een ratchet, gebruiken we ze als een eerste leidraad voor ratchetontwerp. Vervolgens hebben we gedetailleerde en computertijdintensieve 3D simulaties uitgevoerd, waarin de deeltjes expliciet zijn meegenomen. Deze 3D simulaties zijn uitgevoerd om de validiteit te controleren van de classificatieregels die afgeleid zijn uit de 2D simulaties en alleen vloeistofstroming bestuderen. De simulatieresultaten laten zien dat de overgang tussen zigzag en gemengde beweging plaatsvindt bij de kritische lengteschaal $d_{f,1}$; de breedte van het eerste stroomveld. Echter de lengteschaal die de overgang tussen gemengde en verplaatsingsbeweging bepaalt, is groter dan de breedte van het laatste stroomveld $d_{f,N}$, en zou daar helemaal niet mee gecorreleerd kunnen zijn. We hebben geconcludeerd dat deze tweede lengteschaal $d_{f,c}$, alleen bepaald kan worden uit 3D simulaties. De op deze manier afgeleide classificatieregels zijn onderzocht en we zijn in staat gebleken om de migratiehoek van deeltjes in ratchets te correleren met de kritische lengteschalen. Hieruit maken we op dat we de relevante lengteschalen voor deterministische ratchets gedentificeerd hebben.

In het afsluitende hoofdstuk bespreken we de aanpak die we gekozen hebben om uiteindelijk to classificatieregels te komen, en bediscussiëren het effect van de classificatieregels op de belangrijkste kwaliteitsparameters van ratchets gerelateerd aan toepassing in voedingsmiddelen. We hebben gevonden dat voor de kritische lengteschalen 3D simulaties nodig zijn. Echter, specifiek voor compacte ratcheton-

twerpen die relevant zijn voor toepassing in voedingsmiddelen, wijkt de kritische lengteschaal $d_{f,c}$ niet veel af van $d_{f,N}$, die verkregen wordt uit 2D stromingssimulaties en kunnen deze simulaties een snelle manier zijn om $d_{f,c}$ te schatten. Verder hebben we het bestaan van gemengde beweging besproken in termen van selectiviteit tijdens fractioneren van polydisperse suspensies, en hebben gevonden dat de opbrengst, compactheid van het ontwerp, en selectiviteit allen afnemen, maar dit opent ook mogelijkheden voor het fractioneren van een voeding in meerdere stromen in een processtap.

Acknowledgments

During the period that I stay in Wageningen, I have learned many things and met many people who contributed either direct or indirect to this thesis. I would like to thank them in these following lines.

First of all, this thesis would not be possible without helping from my supervisors: Dr. Ruud van der Sman, Dr. Karin Schroën and Prof. Remko Boom. Dear Ruud and Karin, I am deeply thank for all your help, support and encouragement which are real drives for success. You always give me valuable guidance and discussions, not only doing research and writing manuscript but also personal advice.

Dear Remko, although we don't have many discussions like Ruud and Karin, every meeting you give valuable comments to accomplish this research. Your kindness and politeness are also highly appreciated. Under your supervision during doing research, I am very happy. Thanks a lot.

For the help in laboratory and technical support, I wish to thanks Jos, Maurice, Pieter, Dr. Eduard, Dr. Koen and Dr. Maartje. Also Dr. Hoa Pham and Prof. Lina Sarro from Delft University of Technology who produced the device. Thanks is also expressed to my MSc student, Yvette, who helped me during my PhD for valuable contribution to my thesis.

To my colleagues at the process engineering group (6^{th} floor, Biotechnion, I thank all of you for the joyful and very pleasant atmosphere, although most of the time I busy in front of my computer. A lot of nice memories will be in mind, especially from *'PhD trips and labuitjes'*. I wish also to especially thank my roommates (room 623) Annette, Elsbeth and Dorinde for the friendly and pleasant environment in our office.

To be away far from home is not always easy, but my life in Wageningen is full of warmth with lovely Thai community. Many thanks go to Sayam who the first Thai people in Wageningen who introduce me a lot of thing, also let your room be a Thai kitchen for dinner everyday. My special thanks go to Busaba and Kees Schotten for all

your kind help and hospitality. Many thanks also go to Naiyana (for nice lunch), Phatsaraphorn, Wasaporn, Paweena, Krissana Nicolas (for delicious desserts), Arnon and Warangkana (for wonderful trips), Rattanaporn Marcel, Chantita Laurence, Supawoot, Budsara, Warit, U-sa, Kanang, Wirat, Theeraporn, Nipaporn, Panya, Kanjana, Puwanai, Baworn, Kunalai, Varongsiri, Apinna, Sarot, Mongkon, Supranee, Kittisak, Woranarin, Sarn, including younger brothers and sisters in the ODOS project (for cheerfulness and laugther).

Finally I would like to express my most sincere acknowledgments to my parents, brothers and sister for your support with no limitations.

Thanawit

Curriculum vitae

Thanawit Kulrattanarak was born on 26 January 1975 in Bangkok, Thailand. In 1993, he started his bachelor degree in Food Engineering at Kasetsart University, Kamphaeng Saen campus and graduated in 4 years. Afterward he started his master degree in Nuclear Technology at Chulalongkorn University, 1998-2001. His diploma thesis was entitled 'Detection of free radicals in some irradiated crops, spices and herbs'. In 2005, he started his PhD research at Food Process Engineering group at Wageningen University, focusing on fractionation in microfluidic devices, under financial support from the Commission on Higher Education, Ministry of Education, Thailand and the national consortium MicroNed, The Netherlands.

Publication List

T. Kulrattanarak, R.G.M. van der Sman, C.G.P.H. Schroën, R.M. Boom. **2008**. Classification and evaluation of microfluidic devices for continuous suspension fractionation. *Advances in Colloid and Interface Science.* 142:53-66.

Hoa T.M. Pham, T. Kulrattanarak, R.G.M. van der Sman, C.G.P.H. Schroën, R.M. Boom, P.M. Sarro. **2009**. Deterministic ratchets for particle separation fabricated with Si MEMS Technology. *Proceedings of the Eurosensors XXIII conference. Procedia Chemistry* 1:345-348.

T. Kulrattanarak, R.G.M. van der Sman, C.G.P.H. Schroën, R.M. Boom. Refinement of classification rules for deterministic ratchets through 2-D flow field simulation. *Preparation to submit.*

T. Kulrattanarak, Y.S. Lubbersen, R.G.M van der Sman, C.G.P.H. Schroën, H.T.M. Pham, P.M. Sarro, R.M. Boom. Image analysis of particle trajectories in deterministic ratchets including comparison with computed classification rules. *Preparation to submit.*

T. Kulrattanarak, R.G.M. van der Sman, C.G.P.H. Schroën, R.M. Boom. Analysis of particle motion in deterministic ratchet via experiment and simulation. *Preparation to submit.*

Overview of completed training activities

Discipline specific activities

Courses

Internal Lattice Boltzmann course (Wageningen, 2005)

Particle-based modelling of transport phenomena (OSPT, 2006)

CFD for Chemical Engineers (OSPT, 2007)

CFD of Dispersed Multiphase Flow (JMBC/OSPT, 2007)

A Unified Approach to Mass Transfer (OSPT, 2007)

Sustainable Process, Product and System Design (OSPT, 2008)

Meetings

National MicroNano conference (Wageningen, 2007)

The Fifth International conference for Mesoscopic Methods in Engineering and Science (Amsterdam, 2008)

Netherlands MicroNano conference (Ede, 2008)

Conference on Advanced in Microfluidics and Nanofluidics (Hong Kong, 2009)

General courses

PhD introduction week (VLAG, 2006)

Philosophy and Ethics of Food Science and Technology (VLAG, 2006)

Techniques for Writing and Presenting a Scientific Paper (WGS, 2006)

Teaching and Supervising Thesis students (OWU, 2007)

Scientific Publishing (WGS, 2007)

Advanced Course Guide to Scientific Artwork (2008)

Other activities

Preparation of PhD research proposal (2005)

Process Engineering Brainstrom Week (2005)

Process Engineering PhD trips, Denmark and Sweden (2006)

Brain and game food and bioprocess engineering group (2008)

Process Engineering PhD trips, Japan (2008)

Internal Symposium Food Process Engineering (2009)

Theme Meeting Food Process Engineering (2005-2010)